Using high resolution Sr isotope data from the Nama Group, South Africa, to constrain global stratigraphic relationships and continental weathering rates in the terminal Ediacaran

UNIVERSITY OF CAPE TOWN
IYUNIVESITHI YASEKAPA • UNIVERSITEIT VAN KAAPSTAD

McDonald Takondwa Mtonda

Dissertation presented for the degree of Master of Science in the Department of Geological Sciences, University of Cape

28th May, 2022

Supervisor: Dr Rosalie Tostevin

Author's Declaration

I know the meaning of plagiarism and declare that all of the work in the dissertation, save for that which is properly acknowledged, is my own.

Signed by candidate

McDonald T. Mtonda

Abstract

Although life on Earth evolved in the Archean, complex hard bodied animals only emerged in shallow marine environments during the late Ediacaran (~550 Ma). The trigger for the appearance of these hard-bodied animals is still debated but it was probably related to ecological and/or environmental change. Continental weathering fluxes into the oceans can influence redox conditions and seawater chemistry and can be tracked using the strontium isotope ratio of seawater, which can be faithfully captured by carbonate minerals. However, analysis of strontium isotopes in ancient carbonates can be complicated by diagenetic alteration. To ensure that the $^{87}Sr/^{86}Sr$ ratios generated in this study were reflective of primary seawater signals, a sequential leaching procedure, first proposed by Bailey et al., (2000), was tested on Ediacaran bulk rock carbonate samples. The successful implementation of the sequential digestion technique was verified through careful examination of samples for diagenetic alteration using petrography, trace element ratios and $\delta^{18}O$. The sequential digestion technique was then applied to a high-resolution stratigraphic transect through terminal Ediacaran carbonate rocks from the Nama Group, collected in South Africa and Namibia. The isotopic signature of these rocks is consistent with other terminal Ediacaran age rocks, with typically slightly positive $\delta^{13}C$ and relatively high $^{87}Sr/^{86}Sr$ ratios (~0.7085). Correlation with other Ediacaran basins reveals a drop in $^{87}Sr/^{86}Sr$ from ~0.7090 to ~0.7085 ca. 550 Ma. The drop was likely due to location of palaeocontinents compounded by palaeoclimatic cooling during the terminal Ediacaran. These changes provide important context for a critical period in metazoan evolution and may have influenced the cost-benefit ratio of producing hard body parts.

Acknowledgements

For years, I always dreamed of being involved in Palaeoenvironmental reconstruction research but my dreams were nowhere near the excitement and enjoyment experienced from carrying out the actual research. In the past two years, it has been such a privilege to witness events from 550 Ma come to life – it's been a wild and fun ride!

First and most importantly, I would like to thank my supervisor Dr Rosalie Tostevin. It has been an absolute pleasure to have been under your guidance. You gave me the freedom to explore ideas some of which were crazy and you never chastised me but gently and warmly explained to me where I went wrong with my thinking. I intend to remain involved in lifelong academic research and I hope to work with you during the entirety of my career (admittedly, this might be dependent on United becoming better than City again 😊). I will also eternally be grateful for the support you gave me during the unprecedented times of the Covid-19 pandemic. Your help was an integral part to my mental wellbeing during the lockdowns.

I would not have been able to do my MSc work without the technical assistance from the various labs I used to run my samples. I would like to thank John Harrison for helping me with getting to grips with rock prepping equipment and Rene Van Der Merwe for preparing thin sections. Thank you, Dr Julie Luyt for the C and O isotopes analyses and Dr Petrus Le Roux, for the immensely important Sr isotopes analyses. Christel Tinguely is also thanked for trace and rare earth elements analyses.

Field work was fun and surprisingly therapeutic – thanks Wendy Taylor for the crash-course palaeontology lessons offered in the field when my first instinct was otherwise to just smash rocks. Also, thanks WT for being a one-person field support system – your backpack had everything one could ever need while out in the beating sun of the Northern Cape. Aidan Wilton, thanks my guy for generally being my wingman of mayhem – never a dull moment when you're around.

To my other ALE Lab friends, Ansa Nke and Jess Von Der Meden I'm glad I got to work and know you. From cleaning the lab, sample prepping, to impromptu meet-ups, you guys made research stress bearable. Ansa, I had to put up with you going on about Arsenal on our walks home but I'll always cherish those moments.

To Sinelethu Hashibi, Riyaad Mukaddam, Njabulo Ndimande, Katleho Mathafeng and Batande Getyengana, thank you for welcoming and embracing me as one of your own since the Honours year. You made the experience of being a foreign student easy and enjoyable.

Thanks to my mom, dad, siblings and partner for the support and video calls during the time I was away from home. And mom, you can stop freaking out about my wellbeing now.

Lastly but certainly not least, I would like to thank the Government of Malawi and Genus (formerly DSI-NRF Centre of Excellence in Palaeosciences) for the financial assistance without which I would not have been able to complete my studies.

Dedicated to the memory of my grandfather who encouraged my interest in science.

Contents

1 Chapter 1: Introduction

1.1 Appearance of animals

Life first appeared on Earth during the Archean but remained microbial until the Late Neoproterozoic. The first unequivocal fossil evidence for eukaryotes – the locus of all complex life, occurs in the Mesoproterozoic Ruyang Group (~1600 Ma – 1000 Ma) of northern China (Knoll et al., 2006). However, molecular clocks suggest that eukaryotes emerged earlier, with some estimates placing the first appearance of eukaryotes in the Archean. Molecular clock analyses by Parfrey et al., (2011) place the last common ancestor of extant eukaryotes between 1866 Ma and 1679 Ma, while a Palaeoproterozoic age of ~2300, coincident with the Great Oxygenation Event, has also been postulated as the first appearance date for eukaryotes (e.g., Gold et al., 2017; Hedges et al., 2004). The earliest, reliable eukaryote biomarkers (i.e., free from contamination and not synthesized by prokaryotes) only appear at ~820 Ma and this can possibly be attributed to preservation biases. (Brocks et al., 2017). Regardless of the timing of their first appearance, there is consensus that eukaryotes only rose to dominance during the Neoproterozoic (Brocks et al., 2017; Butterfield, 2009; Parfrey et al., 2011).

Fossil steroids (animal-specific biomarkers) and body-fossil evidence constrain the emergence of multicellular animals to the Cryogenian, during the interglacial period of the Sturtian and Marinoan snowball earth glaciations, ca. 660 Ma to >635 Ma (Love & Summons, 2015; Lyons et al., 2021; Maloof et al., 2010). Occurrence of C_{30} steranes possessing a fraction of 24-isopropyl below the Hadash Formation cap carbonate of Oman have been interpreted to indicate the presence of demosponges (Love et al., 2009). Demosponges are the only known extant organisms which biosynthesize 24-isopropyl cholesterol (24-ipc) and other associated structures as major sterols and these steroids degrade to the geologically stable 24-isopropylcholestanes (Love et al., 2009). However, the use of 24-ipc as the principal indicator of sponges during the Cryogenian has been challenged since 24-ipc can also originate from precursor steroids biosynthesized in trace amounts by pelagophyte algae (Antcliffe, 2013 but see a response by Love & Summons, 2015). Recently a new C_{30} sterane, denoted as 26-methylstigmastane (26-mes), has been reported in Neoproterozoic strata from India, Oman and Siberia, and occurs alongside 24-ipc (Zumberge et al., 2018). Crucially, demosponges are the solely verified extant organisms which produce sterols whose carbon skeletons resemble

26-mes (Zumberge et al., 2018). As such, the co-occurrence of 26-mes and 24-ipc between 660 Ma and 635 Ma, in almost equal proportions provides the best biomarker evidence for a pre-Ediacaran emergence of animals (Lyons et al., 2021; Zumberge et al., 2018).

The first possible animal body fossils have been documented from the Ediacaran-aged Trezona Formation, Australia, based on similar characteristics with simple sponges (Maloof et al., 2010). However, multiple fossil evidence, obtained from over 30 localities, across five continents has shown that architecturally complex, macroscopic, metazoans emerged during the Ediacaran, ~575 Ma. However, biomineralizing metazoans – animals with hard body parts – only appeared ~25 Myr later during terminal stages of the Ediacaran (Canfield et al., 2007; Narbonne, 2005).

The Ediacaran biota, named after the Ediacara Hills of South Australia, are temporally restricted and found in specific marine environments and sedimentary facies (Droser et al., 2006; Grazhdankin, 2004; Waggoner, 2003). They have been divided into three assemblages; the Avalon, White Sea and Nama assemblages.

The Avalon assemblage biota are the oldest (579 – 560 Ma) of the three and were simple invertebrate organisms that colonized deep marine to continental shelf/slope environments (Droser et al., 2017; Laflamme et al., 2013). Fossils of this assemblage have been found in North America and Europe, and they thrived over the longest timespan in comparison to the younger assemblages (Droser & Gehling, 2015) Avalon type fossils do not exhibit complex activities such as mobility (Droser & Gehling, 2015; Grazhdankin, 2004). There are three clades associated with the Avalon assemblage and these are *Rangeomorpha*, *Arboreomorpha*, and *Triradialomorpha* (Laflamme et al., 2013)

White Sea assemblage biota are of intermediate age (558 – 550 Ma) and are found in shallower marine settings (Grazhdankin, 2004; Narbonne, 2005). They are more complex compared to Avalon but are restricted to a shorter time span and have a wider geographical distribution (Droser et al., 2006; Laflamme et al., 2013; Waggoner, 2003). The assemblage is also more faunally diverse compared to the Avalon, with the White Sea assemblage containing three times more genera than the Avalon assemblage (Droser et al., 2006; Grazhdankin, 2004; Laflamme et al., 2013) Clades of *Erniettomorpha*, *Dickinsoniomorpha*,

Kimberellomorpha, *Bilaterialomorphs*, *Tetraradialomorphs*, and *Pentaradialomorphs* have all been associated with the White Sea assemblage (Laflamme et al., 2013).

The Nama assemblage is the youngest (550 – 541 Ma) and contains the most complex and physically largest fossils of the three assemblages (Droser & Gehling, 2015; Germs, 1972; Narbonne, 2005). They represent the earliest skeletal metazoans and signify evolutionary innovation in organisms (Wood, 2018). There is also evidence of predation and mobility reflected in the fossils of the Nama assemblage (Droser et al., 2017; Tarhan et al., 2018). These organisms occupied shallow marine settings and fossil preservation is controlled by sedimentary facies whereby soft bodied organisms are preserved in siliciclastic rocks while skeletal fossils are preserved in carbonate rocks (Laflamme et al., 2013; Waggoner, 2003; Wood et al., 2017a) The Nama Assemblage is less diverse compared to the older assemblages but is distinguished by the occurrence of the hard-bodied fossils such as *Cloudina*, *Namacalathus, Namapoikia and Sinotubulites* (Amthor et al., 2003; Wood, 2011; Wood et al., 2002). The subsequent Cambrian radiation led to emergence of larger and more complex biota as animals entered into an ecological arms race but the detailed discussion of this is extremely broad and is beyond the focus of this research project.

1.2 Palaeoenvironment changes and influence on evolution of animals

Environmental changes have been suggested to have contributed to the emergence of complex animals and particularly hard-bodied metazoans. Three factors have been proposed as controls on the evolution of biomineralizing metazoans: 1) change in oxygen levels, 2) changes in carbonate saturation, and 3) the rise of predation. The debate about the relative importance of these three factors is ongoing, but they may all have played important roles at different times. Changes in marine redox and carbonate saturation are influenced by continental element fluxes, which in turn are influenced by rates of weathering. It is thus important to understand what the weathering and redox conditions were like across this time period. To achieve this, we need high-resolution records that are consistent across multiple continents. One barrier to doing this is uncertainty about how different sections correlate. Biostratigraphy is a useful correlation tool, but fossils may have long time ranges and might also be diachronous (e.g., Laflamme et al., 2013). Similarly, radiometric dates provide tie points for certain intervals but these dates are not always available due to dependence on presence of volcanic ash and these dates can also have large errors, although it is

acknowledged that U-Pb high precision ID-TIMS currently offers the best age resolution with precision of <0.1% (e.g., Baadsgaard et al., 2020; Zeh et al., 2015; von Quadt et al., 2016; Tapster and Bright, 2020). Therefore, correlating between different cratons, and understanding how the geochemical signals tie to the fossil record, is a necessary framework before investigation of other questions, such as weathering rates and oxygen levels, or even basic palaeontological frameworks (which fossils existed when and how geographically widespread they were). These points will be the focus of this research project. Nevertheless, the following two sub-sections will highlight the important discussion points concerning the aforementioned three factors and their possible influence on animal evolution during the Ediacaran.

1.2.1 Redox conditions and emergence of complex metazoans

It was once thought that there was a single step rise to stable, well oxygenated deep oceans during the Ediacaran, an episode dubbed the Neoproterozoic Oxygenation Event (NOE) (Canfield et al., 2007; Shields-Zhou & Och, 2011). Hence it was concluded that the appearance of complex biota was delayed during the mid-Proterozoic due to low atmospheric and oceanic oxygen levels, and only once stable oxic conditions developed in the deep oceans, could multicellular Ediacaran biota evolve (Canfield et al., 2007; Planavsky et al., 2014). However, mounting evidence supports more dynamic redox conditions during the Ediacaran with anoxic environments punctuated by episodes of oxygenation (Sahoo et al., 2016; Tostevin, Wood, et al., 2016; Tostevin & Mills, 2020; Wood et al., 2015; Zhang et al., 2018). Further, although it has proven difficult to reconstruct and reconcile the oxygenation events using different geochemical proxies, the best available evidence points to stable deep marine oxygenation conditions only being attained in the Palaeozoic (Tostevin & Mills, 2020). Thus, the emerging narrative is that the minimum oxygen requirements of simple metazoans such as sponges have probably been met since the Great Oxygenation Event (GOE, ~2400 Ma – 2300 Ma) while more complex animals emerged in restricted, well-oxygenated pockets on shallow marine shelves during the Ediacaran (Canfield et al., 2013; Mills et al., 2014; Wood et al., 2019; Wood & Erwin, 2018).

It is clear there is a need for at least low levels of oxygen to support of animal life, even though the oxygenation events are yet to be fully constrained. An equally important consideration is that anoxic conditions were prevalent for most of the Ediacaran. It is tempting to assume that

anoxic conditions brought about mass extinctions. However, recent work suggests that widespread anoxia could have provided favourable environmental conditions for novel and innovative evolutionary mechanisms (Wood & Erwin, 2018). It has been suggested that widespread anoxia facilitated morphological inventions in benthic soft-bodied biota and thus provided an ancestral framework on which skeletal lineages appeared as innovations upon the onset of stable oxic environments (Wood, 2018). This would imply that anoxic environments served as the trigger for major evolutionary diversification of metazoans and would support the view that metazoans evolved through successive, radiation events (Wood et al., 2019).

1.2.2 Biomineralization

Skeletal organisms presently dominate the animal kingdom and as such, their appearance in the fossil record marks a significant step change in the history of life. Biomineralization was preceded by the appearance of motility (~560 Ma) and possible carnivory (~550 Ma), and the development of hard parts would have been beneficial for the protection of soft tissue (Knoll, 2003). Therefore, it has been argued that ecological pressure was the first order cause in the development of skeletons (Knoll, 2003; Wood, 2011). Nevertheless, the process of constructing skeletons exerts a huge metabolic cost on the biomineralizing organism but this cost is subsidized in well oxygenated environments (Knoll, 2003; Towe, 1970). However, due to the dynamic redox architecture of Ediacaran oceans, it has been suggested that seawater chemistry played an important role in controlling the mineralogy of the skeletons to compensate for energy costs associated with production of the skeletal material (Porter, 2010; Wood et al., 2017a; Wood & Erwin, 2018). For example, animals that evolved skeletons in aragonitic seas would adopt aragonitic skeletons (Porter, 2007, 2010). Aragonite vs calcite vs dolomite seas would have been controlled by temperature, as well as Mg/Ca ratios, SO_4^{2-} and potentially Fe^{2+} and phosphate concentrations (Balthasar & Cusack, 2014; Bots et al., 2011).

Ediacaran skeletal fossils, with diverse skeletal lineages, are exclusively found in carbonate rocks but commonly have soft-bodied equivalents in coeval siliciclastic rocks (Germs, 1972; Wood et al., 2017a; Wood et al., 2002). Hence it has been suggested that passive biomineralization was environmentally triggered in $CaCO_3$ saturated waters. (Wood et al., 2017b). Changes in seawater chemistry could be linked to an increase in supply of Ca^{2+} ions

into Ediacaran oceans which would have increased $CaCO_3$ saturation (Tostevin et al., 2019a; Wood et al., 2017b). Increased weathering would have also increased alkalinity of seawater which would further increase $CaCO_3$ supersaturation, reducing the energy cost associated with biomineralization (Wood et al., 2017b; Wood & Erwin, 2018).

1.3 Nama Group

1.3.1 Geological setting

This study focusses on geochemical records from the Nama Group, a well-studied succession of Ediacaran rocks that contain the Nama Assemblage of the Ediacaran biota, including skeletal fossils. The Nama Group comprises siliciclastic and carbonate rocks that have an outcrop area of 125,000 km^2 and a cumulative thickness of >3000 m (Germs, 1995; Saylor et al., 1998). These rocks are located in southern Namibia and northwestern South Africa and are of Late Proterozoic to Early Cambrian age (Germs, 1995). Nama Group rocks largely rest on crystalline basement but in some areas unconformably overlie the Numees Formation sedimentary strata and are succeeded by Table Mountain Group sandstones on the South African side (Germs, 1983). Samples collected from ash layers yield ages that fall in the range of ~547 – 538 Ma (Bowring et al., 2007; Grotzinger et al., 1995; Linnemann et al., 2019; Nelson et al, 2022). There are three distinct lithologies, Kuibis, Schwarzand and Fish River subgroups and these were deposited in two connected basins separated by a palaeo-structural feature known as the Osis Ridge (Germs et al., 1986).

The Kuibis Subgroup represents the oldest sequence of rocks and the strata were deposited in two cycles of basal quartzitic sandstone, with conglomerate in some places, overlain by successions of shales and limestones(Germs, 1983). In the deeper parts of the two sub-basins, sandstones laterally grade into shales and limestones while shales dominate in the north-western regions of the Nama Basin (Germs et al., 1986). The thickness varies from tens of metres in the South and in the region near to the Osis Ridge, to ~800 m in the northwestern reaches of the basin (Germs et al., 1986).

Most of the Schwarzrand Subgroup sits conformably on top the Kuibis strata (Germs, 1983). Thick successions of limestone intercalated with sandstones and shales dominate in the South and these have an increasingly upward immaturity (Germs et al., 1986; Saylor et al., 1995). The limestones thin out towards the East and North and unconformities have been observed in this sequence (Saylor et al., 1995, 1998). Red shale beds appear in the Nomstas Formation,

near the top of Schwarzrand Subgroup and they laterally transition into stromatolitic limestone and blue-tinted shale to the south and southwest. The thickness of the strata increases towards the west and north west, reaching a maximum thickness of 1400 m (Germs, 1995)

Fish River Subgroup strata unconformably overlie Schwarzrand Subgroup rocks and comprise red, medium to coarse-grained feldspathic sandstones, intercalated with shales (Saylor et al., 1995, 1998). Five major fining-upward cycles have been identified in the northern section of the outcrop area (Gresse & Germs, 1993). Stratigraphic thicknesses for this subgroup have an inverse pattern to that of the older sequences with the thickest strata located in the south and east (Gresse & Germs, 1993; Saylor et al., 1995).

Provenance studies show that siliciclastic sediments of the Kuibis and Schwarzrand originate from easterly sources on the Kaapvaal Craton while the Fish River Subgroup is a distal molasse and the source material came from northerly and westerly sources during the late deformation stages of the Damara and Gariep orogens (Blanco et al., 2011). Further, the post-Gaskiers glaciation Vingerbreek Member was formed by sediments from eastern and western sources, possibly due to the closure of the Adamastor Ocean and the collision of the the Arachania terrane with the Kalahari Craton (Hofmann et al., 2014). The Kuibis and Schwarzrand subgroups were deposited in environments ranging from braided streams to quiet subtidal marine (Saylor et al., 1995). Intertidal to shallow subtidal deposits predominate in the two lower subgroups but fluival conditions become increasingly dominant in the Upper Schwarzrand and all of Fish River Subgroup (Blanco et al., 2011; Saylor et al., 1995).

1.3.2 Palaeontology

The Nama Group is the type locality for the Nama Assemblage and this unique fossil assemblage is an essential part of the global stratigraphic history. The Nama Assemblage were extant for ~10 Myr and appear and disappear relatively abruptly from the geologic record and have thus been used to correlate regional and global strata since their presence provides a first order indication that rocks are of the same age. In the ensuing discussion, the focus will be on hard bodied fauna because: 1) this is a major evolutionary innovation which first

appears in this assemblage, and 2) they have so far been found in carbonate rocks which are the focus of this study.

1.3.2.1 Cloudina

Cloudina is one of the oldest skeletal metazoans. It was first described by Germs, (1972) who discovered the shelly fossils of this enigmatic animal in the Kuibis Formation, Zaris subbasin, of the Nama Group, Namibia. They were described as sinuous calcareous tubes which have stacked cones, giving them the appearance of composite structure with two walls. The inner walls have a smooth texture while the outer walls have annular ridges and depressions. The inner tubes of the organism were found to be not ordinarily centrally located in transverse section (Hua et al., 2005). Both the apex and the distal end of *Cloudina* were found to be almost always open. Two species, principally distinguished by size were recognized, *Cloudina hartmann*ae and *Cloudina riemkeae*. *C. hartmannae* was the larger of the two species and grew to 2.5 to 6.5 mm wide and 8 to 150 mm long while the size of *C. riemkeae* was 0.3 to 1.3 mm wide and 1.5 to 12 mm long. *Cloudina* grew by eccentrically stacking its funnel-shaped tubes and secreted new calcareous units inside existing funnels, a technique which is similar to modern-day metazoan biomineralization (Germs, 1972). Further, the thickness of the tubes was environmentally controlled (Shore & Wood, 2021). *Cloudina* is difficult to systematically describe and the recent discovery of polytomous (multiple) dichotomous branching in *Cloudina* and similar skeletal taxa (collectively called cloudinomorphs) possibly suggests metazoans of diverse taxa (Shore et al., 2020).

Cloudina formed its shelly walls by depositing $CaCO_3$ on an organic template (Brain, 2001; Grant, 1990). The primary mineralogy of the skeleton of *Cloudina* has been debated to have either been high-Mg calcite or aragonite but recent Ca isotope data suggests that *Cloudina* precipitated aragonite shells which were later altered to calcite during diagenesis (Pruss et al., 2018). *Cloudina* were benthic dwelling, immobile and also reef builders, possibly as an evolutionary innovation in response to predation and competition (Penny et al., 2014).

Cloudina is of great importance because it is almost always found in Ediacaran limestones which are interbedded with siliciclastic rocks that host soft-bodied fossils (Brain, 2001). This is interesting because prior to *Cloudina*'s discovery, it was thought that soft-bodied Ediacaran fauna predated skeletal organisms by millions of years (Conway Morris et al., 1990). The

concurrent occurrence of Ediacaran soft-bodied and skeletal fauna therefore provides evidence that organisms had already evolved mechanisms for producing skeletal parts.

1.3.2.2 Namacalathus hermanaste

Namacalathus hermanaste, first described by Grotzinger et al., (2000) is another species of Ediacaran skeletal metazoan which coexisted with *Cloudina*. They are goblet or chalice shaped, cm-scale fossils that predominantly colonized thrombolite-stromatolite reefs. *Namacalathus* individuals have walls around 1 mm thick, and a basal stem which is open at both ends and is connected to an ellipsoidal cup. The cup has 6 or 7 perforations which have slightly incurved margins and are regularly distributed around the cup periphery, with lateral walls separating the perforations. The cup also possesses an upper circular opening which is lined by an incurved lip. *Namacalathus* biomineralization was similar to *Cloudina* in that individuals also deposited high-Mg calcite onto an organic template (Wood, 2011). This is important because the preferred cement during the Ediacaran Period was aragonite. As such, formation of calcite skeletons by these metazoans provides evidence that they had already evolved physiological pathways which were incorporated into skeletal biomineralization (Wood et al., 2017a).

Namacalathus fossils are preserved in calcitic void fills in a calcite matrix and are thus impossible to isolate using conventional techniques such as acid dissolution (Watters & Grotzinger, 2001). This makes defining of their morphology difficult, although digital reconstruction suggests that *Namacalathus* was of cnidarian affinity (Grotzinger et al., 2000; Wood, 2011).

1.3.2.3 Namapoikia rietoogensis

Namapoikia rietoogensis is a controversial Ediacaran metazoan first described by Wood et al., (2002) from the Driedoornvlagte reef complex (Wood & Penny, 2018) of the Omkyk Member, Nama Group. Presently, this is the only known location of this metazoan. *Namapoikia* has been classified as poriferan in affinity (Wood et al., 2002). It encrusted synsedimentary fissures that formed perpendicular to the bedding plane within thrombolitic reefs and in very rare occurrences, *Namapoikia* colonized open reef surfaces (Wood, 2011). *Namapoikia* grows as individual nodules or domes and extends laterally in a sheetlike manner or coalesces into mounds (Wood et al., 2002). *Namapoikia* could grow up to 1 m width and 0.25 m height and had a modular skeleton made of incomplete, continuously linked tubules with diameters

ranging from 1.5 to 5 mm (Wood et al., 2002). Tubules of *Namapoikia* do not increase in size with growth of organism but grow by longitudinal fusion and they appear labyrinthine when viewed in transverse section (Wood & Penny, 2018). Skeletal biomineralization was achieved through sustained calcification of an organic scaffolding, during a relatively long lifespan of *Namapoikia* individuals (Wood & Penny, 2018).

Namapoikia had a considerably longer lifespan in comparison with *Cloudina* and *Namacalathus*, leading to the suggestion that its cryptic habitat was persistently oxic for extended timescales compared to the ephemeral nature of environments which were sometimes colonized by *Cloudina* and *Namacalathus* (Wood & Penny, 2018). The same authors also report the first evidence of competition between metazoans and microbial mats during the Ediacaran. *Namapoikia* principally encrusted two substrate types: lithified thrombolite and unlithified, living thrombolite and microbialite. In turn, microbial mats have been found growing on top of *Namapoikia* individuals thus providing evidence that advanced adaptations for robust substrate competition had evolved in these Ediacaran benthic communities (Wood & Penny, 2018).

Recently, Mehra et al., (2020) have argued against the classification of *Namapoikia* as a metazoan. Mehra et al. (2020) argue that the lack of diagnostic features synonymous with sponges such as aquiferous system, ostia, an osculum, and/or any spongin, tissues, or fibers make it unlikely that *Namapoikia* was a sponge. Furthermore, the scale of partitions and voids suggest an anomalously large structure which does not compare to any known sponges, extant or extinct. The same authors propose that *Namapoikia* was probably a microbially mediated structure and not a metazoan, owing to its morphological expression. The widely spaced meandering partitions that split and merge transversely and longitudinally made it structurally unstable and needed to be propped up externally. The distinct morphology of *Namapoikia*, according to Mehra et al. (2020), is down to the unique growth environment of *Namapoikia* and structure would be different in different ecological settings.

Commenting on the objections raised by Mehra et al., (2020), (Xiao, 2020) adopts a middle ground approach by appealing to the enigmatic nature of Ediacaran-Cambrian boundary metazoans. The author suggests acknowledgement that the last common ancestor of sponges was of Ediacaran origin, possibly closer to the Ediacaran-Cambrian boundary. Thus, diagnostic features of Cambrian sponges e.g., spicules, probably evolved after the crown-group split and

need not be used in identifying Precambrian sponges. Xiao (2020) concludes that even though it is unclear whether *Namapoikia* was a sponge, there is still evidence that it was an important member of Ediacaran-reef metazoan community.

1.3.3 Geochemical setting

There is a substantial amount of existing geochemical data for the Nama Group, including carbon isotopes (Bowyer et al., 2022; Wood et al., 2015), calcium isotopes (Pruss et al., 2018; Tostevin et al., 2019a), sulfur isotopes (Ries et al., 2009; Tostevin et al., 2017), Uranium isotopes (Tostevin et al., 2019b), I/Ca (Uahengo et al., 2020), Fe speciation (R. A. Wood et al., 2015), rare earth elements (REE) (Tostevinet al., 2016b) and $^{87}Sr/^{86}Sr$ (Kaufman et al., 1993a). This thesis will focus on $\delta^{13}C$, REE and $^{87}Sr/^{86}Sr$. Chemostratigraphic correlation of Nama Group carbonates yield carbon isotope profiles ($\delta^{13}C$) that are similar to global late Neoproterozoic trends (Bowyer et al., 2022; Kaufman et al., 1991). Isotopically light limestones above glacial tillites progressively become $\delta^{13}C$ enriched with the heaviest value of +6‰ observed in limestones from the Zaris Formation. Above these limestones, values drop to a mean of +2‰ for the succeeding strata (Bowyer et al., 2022; Kaufman et al., 1991; Saylor et al., 1998; Wood et al., 2015). Rare earth elements (REE) patterns are consistent with authigenic carbonates deposited in an open marine environment and show that these carbonates precipitated from seawater which was connected to the global ocean (Tostevin et al., 2016a). $^{87}Sr/^{86}Sr$ values of ~0.7085 have been reported for Nama lithologies (Kaufman et al., 1993) but these are sparse and the exact locations where sampling was done are not clearly known.

1.4 Aims

This thesis aims to generate primary $^{87}Sr/^{86}Sr$ data through the terminal stage of the Ediacaran to enable high resolution chemostratigraphy and constrain continental weathering rates, and ultimately, provide context for the evolution of skeletal biota.

1.4.1 Objectives

- Conduct field work in the Northern Cape, South Africa, to produce stratigraphic logs and collect carbonate and shale samples from the Upper Nama Group.
- Generate thin sections of key samples for petrographic assessment of lithology and degree of diagenesis.

- Analyse $\delta^{13}C$ on Upper Nama Group carbonates for regional correlation of the study area with the wider Nama Group
- Analyse $\delta^{18}O$ on Upper Nama Group carbonates to assess diagenesis.
- Analyse trace elements and rare earth elements of Upper Nama Group carbonates via ICP-MS to determine impacts of diagenesis and primary redox conditions.
- Use Ce anomalies to expand the 4D map of redox conditions across the Nama Group to the Upper Nama Group, where there is currently a dearth of data
- Confirm sequential leaching method (Bailey et al., 2000) for extraction of primary Sr from carbonates in older, bulk rock limestones.
- Analyse $^{87}Sr/^{86}Sr$ on carbonates through a stratigraphic transect of the Lower and Upper Nama Group and fit into global chemostratigraphic framework.
- Interpret geochemical proxies data to determine how global weathering rates were changing across the Ediacaran–Cambrian Boundary, and assess their impact on the first skeletal biota.

2 Chapter 2: Background on geochemical proxies

2.1 Carbon isotopes

There are two stable isotopes of carbon, C-12 and C-13, with respective natural abundances of 98.89% and 1.11% (Hoefs & Hoefs, 1997). Isotope ratios are stated as permil (‰) deviations from a standard, formerly a Cretaceous belemnite (PDB), *Belemnitella americana,* from the PeeDee Formation of South Carolina, USA (Craig, 1953). The Vienna-PDB is now in use following the depletion of the original PDB. The permil deviation is expressed as $\delta^{13}C$ and is calculated using the formula:

$$\delta^{13}C = \left(\frac{R_{sample} - R_{standard}}{R_{standard}}\right) \times 1000; where\ R = \frac{^{13}C}{^{12}C} \qquad \text{Equation 1}$$

Due to mass differences between these two isotopes, fractionation occurs between the major reservoirs of carbon. Craig, (1953) first reported variations in carbon isotope composition between terrestrial carbon reservoirs and laid the foundation for their usage in geological studies. Further work by (Scholle & Arthur, 1980) showed that $\delta^{13}C$ variations across carbon-rich stratigraphic units can be correlated with other, distant carbon-rich sedimentary rocks of the same age.

In the ensuing years, more research provided strong evidence for the reliability of carbon isotopes as proxies for palaeoenvironment reconstruction (Berger & Vincent, 1986; Jenkyns, 1995; Jenkyns et al., 1994; Shackleton, 1986; Weissert, 1989). Organic productivity is the main control on the $\delta^{13}C$ of marine waters. The process of photosynthesis favours C-12 over C-13, resulting in organic carbon with a low $\delta^{13}C$ (Sharp, 2017; Farquhar et al., 1989; Jenkyns et al., 1994; Weissert, 1989). Consequently, dissolved inorganic carbon (DIC) becomes enriched in C–13. Since carbon is removed from the ocean through two major pathways, burial of organic carbon in sediments and precipitation of carbonate rocks (Scholle and Arthur, 1980), the balance between these two sinks affects the $\delta^{13}C$ of seawater DIC. Increased removal of carbon through burial of organic carbon will lead to enrichment in $\delta^{13}C$ in DIC and vice versa. Since carbonate minerals usually precipitate in isotopic equilibrium with DIC (Marshall, 1992), they inherit the $\delta^{13}C$ of the seawater DIC pool.

The main control on the $\delta^{13}C$ of seawater over long timescales, and therefore carbonate rocks, is the amount of organic carbon burial as a proportion of the total carbon sink, which is controlled by primary productivity and carbon burial rates. Factors which influence the rate of photosynthesis include the availability of sunlight and nutrients. Excessive nutrient influx can lead to an extreme increase in bio-productivity, which may in turn cause deoxygenation of the water column and anoxia (Boudinot et al., 2021). Most organic carbon will be respired and remineralised in the water column or shallow sediments. Anoxia, high sedimentation rates and decreased sediment mixing can all increase the fraction of carbon that escapes re-oxidation and ends up buried and removed from the system. Although potentially complicated, changes in the $\delta^{13}C$ of seawater are pivotal in our understanding of palaeoenvironments (e.g., palaeo-ocean salinity, mass extinctions, changes in redox conditions across geologic time, tectonic upheavals). Carbon isotope chemostratigraphy has also become a common tool for correlating global stratigraphic units, since major excursions in seawater $\delta^{13}C$ should be recorded globally (e.g., Halverson et al., 2007; Sawaki et al., 2010; Bowyer et al., 2022).

Even though carbon isotope chemostratigraphy is now widely used, several factors need to be considered before $\delta^{13}C$ analysis, such as the type of material being analysed, local depositional conditions and diagenetic alteration. $\delta^{13}C$ data can be obtained from organic and/or inorganic carbon, which represent the marine organic carbon and DIC pools, respectively. It is important to understand the inherent differences between the two sources. Organic matter is more reactive than inorganic carbonate and this results in poorly understood, complex processes which affect $\delta^{13}C_{org}$, complicating data interpretation (Werne & Hollander, 2004). Similarly, although carbonates form in near-isotopic equilibrium, significant shifts can occur. Vital effects, i.e., biologically influenced isotopic offsets between secreted skeletal material (shells) and ambient seawater, can cause significant shifts in $\delta^{13}C_{carb}$ (see Wendler, (2013) for a detailed review). Abiotic or microbial carbonates can also be slightly enriched in $\delta^{13}C$ compared to seawater by 1–2‰, but these offsets are small compared to long term variation in seawater $\delta^{13}C$ (Scholle & Arthur, 1980). Moreover, carbon-rich fluids can alter the $\delta^{13}C$ of carbonates during diagenesis, although this is rare.

2.2 Oxygen isotopes

Oxygen stable isotopes exhibit strong temperature and composition of seawater dependent fractionations and are thus useful as Palaeotemperature proxies (Urey et al., 1951) Although there can be large $\delta^{18}O$ fractionation effects between carbonates and the solution from which they precipitated, the process is assumed to have occurred in isotopic equilibrium such that the carbonate mineral is related to its source fluid through a temperature dependent fraction factor (α) (Marshall, 1992). This enables the determination of past ocean temperatures with a high confidence, if the $\delta^{18}O$ of seawater is known. However, $\delta^{18}O$ values of older carbonate rocks are susceptible to diagenetic alteration through interaction with fluids with a different $\delta^{18}O$ (Halverson et al., 2007; Kuznetsov et al., 2018). Isotopic resetting is severe in Precambrian rocks due to alteration caused by diagenesis, deformation and/or hydrothermal alteration. So, rather than reflecting palaeotemperature, $\delta^{18}O$ data are useful for tracking diagenetic screening. Although cut-off values for $\delta^{18}O$ are arbitrary, samples with $\delta^{18}O$ of less than -10‰ are considered severely altered and are commonly disregarded as viable options for further geochemical analyses (Kuznetsov et al., 2018; Li et al., 2011). The $\delta^{18}O$ data obtained in this project were thus used to screen for diagenetic alteration.

2.3 Trace elements

Trace elements refer to chemical elements whose concentrations are less than 0.1 wt% of a rock. In carbonates and other sedimentary rocks, trace elements have been used to acquire information about the type of fluids from which the rocks originated (Ge et al., 2010). Redox sensitive trace elements such as vanadium and molybdenum have been used as palaeoredox proxies due to their enrichment in sediments being controlled by their oxygenation state which is related to the redox conditions at the time of precipitation of the sediments (Bennett & Canfield, 2020). Radioactive trace elements such as uranium and thorium are also used in dating carbonates (e.g. Pickering, 2015). However, in this study, trace elements are of importance due to their behaviour during diagenesis which enables the use of trace element ratios such as Mn/Sr and Fe/Sr to evaluate the extent of diagenetic alteration (Banner, 1995).

2.4 Rare earth elements

The rare earth elements (REEs), also known as lanthanides, are a group of 15 elements (La, Ce, Pr, Nd, Pm, Sm, Eu, Gd, Tb, Dy, Ho, Er, Tm, Yb, Lu) which have very similar chemical properties. There are some small but predictable differences among them, making them

extremely useful in tracer studies (Elderfield et al., 1988). The REEs are affected by riverine, aeolian and hydrothermal input, redox reactions, adsorption and scavenging onto particles (Bender, 1982)

The similarity in the chemical properties of REEs is due to their electron structure which permits the electron filling of lower energy 4f orbitals. These are shielded by outer electrons and this prevents major differences in chemical reactivity (Elderfield et al., 1988). Due to nucleosynthesis, REEs with even numbers are more abundant than odd numbered REEs and as such, data are normalized to post Archean Australian Shale (PAAS) to smooth out these natural variations (Elderfield et al., 1988; Pourmand et al., 2012). Normalized modern seawater REE trends are smooth with progressive enrichment in heavy-REEs (HREEs; Figure 1) (James et al., 1995) which is caused by increased tendency for complexation with carbonate ions across the lanthanide series due to the progressive reduction in ionic radii (Byrne & Kim, 1990; Elderfield et al., 1988, 1990). Since REE are incorporated into the crystal lattice of carbonate minerals with minor fractionation, they are used as proxies for ancient seawater chemistry (Banner et al., 1988; Banner & Hanson, 1990).

Modern oxygenated seawater REE patterns also show depletions in Ce relative to neighbouring REE, and this is particularly important for understanding marine redox conditions. Although all REEs exist as trivalent (+3) ions, Ce can also exist in the +4 oxidation state. In oxic environments, Ce(III) is oxidized to Ce(IV) which is very insoluble and is drawn down onto particulates, leaving residual water depleted in Ce (Alibo & Nozaki, 1999; Elderfield & Greaves, 1983; German & Elderfield, 1990). Ce anomalies in high-purity carbonate rocks can thus be used as localized redox proxies for ancient oceans (Tostevin et al., 2016a). Importantly, carbonate-bound REEs are resilient to dolomitization and diagenetic alteration (Banner et al., 1988; Liu et al., 2019; Webb & Kamber, 2000) and are therefore useful proxies in the study of ancient environments. Ce anomalies are not always easily identified from REE trends. Therefore, calculations are done using formulae that compare the relationship of the element to neighboring REEs. One such equation was derived by Lawrence et al., (2006) and is expressed as:

$$Ce^*/Ce_{SN} = \frac{[Ce]_{SN}}{[Pr]^2_{SN}/Nd_{SN}};$$ where SN = normalized to PAAS Equation 2

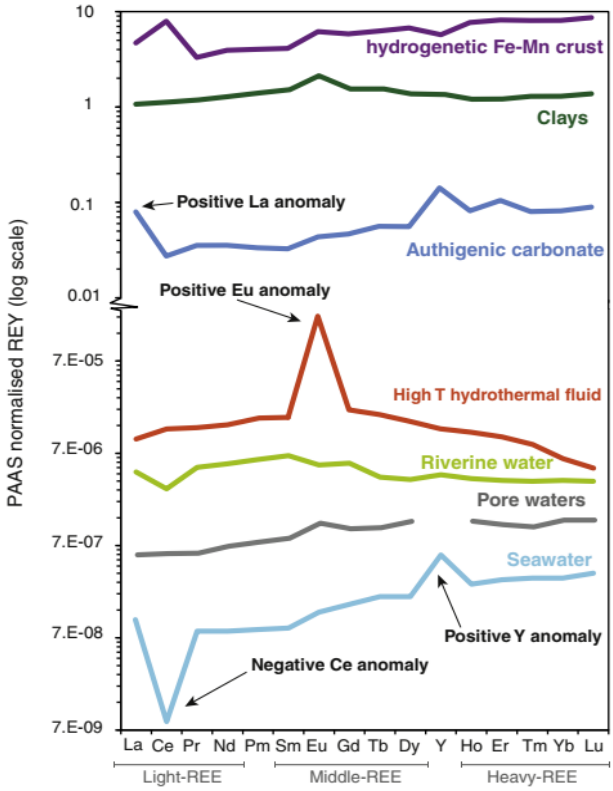

Figure 1: Rare earth elements patterns for important natural environments and minerals showing the distinct element anomalies. From Tostevin et al., (2016).

2.5 Strontium isotopes

2.5.1 Geochemistry of strontium

Strontium (Sr) is a Group IIA element, with an atomic number of 38, and has four naturally occurring, stable isotopes: 84, 86, 87 and 88, whose proportions approximately 0.56% : 9.87% : 7.04% : 82.53% (Faure & Powell, 1972; Veizer, 1989). The isotopic abundances are slightly variable due to generation of ^{87}Sr through radioactive (β^-) decay of Rubidium (^{87}Rb):

$$^{87}_{37}Rb \rightarrow {}^{87}_{38}Sr + \beta^- + \bar{\nu} + Q$$; where $\bar{\nu}$ = antineutrino, Q = decay energy

Strontium, like all alkaline elements, has two valence electrons in the s orbital outside the electron configuration of krypton ([Kr]$5s^2$) and as such, forms ions with a +2 oxidation state (Faure & Mensing, 2005).

In modern marine environments, the mean concentration of Sr is 7.85 ± 0.03 ppm although slight variations occur with depth and salinity (Veizer, 1989). Input of Sr to the ocean comes from:

1. Continental runoff, primarily from riverine discharge

2. Continental runout, through groundwater discharge
3. Oceanic crust – seawater interaction at (i) mid-oceanic ridges (high temperature conditions), (ii) ridge flanks and intracrustal (low temperature conditions)
4. Reflux from diagenetic pore waters and sediment stabilization (mineral recrystallisation)

Under steady state conditions, Sr input is counterbalanced by precipitation of sediments, principally carbonates (Veizer, 1989). Today, continental runoff has been estimated to be 4.55 ± 0.15 x 10^{16} Lyr^{-1} and this results in an Sr flux into oceans of ~2.73 ± 0.09 x 10^{9} $kgyr^{-1}$. Groundwater discharge has been estimated to be only 5% of riverine discharge. However, due to the high concentrations of Sr in aquifers, it has been estimated that the annual groundwater flux of Sr is ~1.95 ± 0.5 x 10^{9} kg, although it has proved difficult to constrain this variable. The cumulative input of water from global hydrothermal systems is ~1.85 x 10^{14} $kgyr^{-1}$ resulting in a Sr influx of ~0.42 ± 0.19 x 10^{9} $kgyr^{-1}$. Oxygen isotope data and calcium concentrations in pore waters suggest that alteration of oceanic crust during interaction with seawater which results in low temperature (<70°C) chemical weathering contributes an estimated annual Sr influx of ~0.035 x 10^{9} kg. Recrystallization of carbonate minerals during deep-sea diagenesis releases Sr into the water column and the estimated reflux is ~0.26 x 10^{12} g/yr. For a detailed review of Sr fluxes in seawater, see Veizer (1989) and the references therein.

2.5.1.1 Behaviour of Sr during carbonate precipitation

The principal mode of Sr removal from seawater is through chemical precipitation of carbonate minerals such as aragonite, high-Mg calcite (HMC) and low-Mg calcite (LMC), and to a lesser extent, Sr minerals such as celestite and strontianite. Strontium is incorporated into minerals through:

1. Substitution for Ca^{2+} in $CaCO_3$ crystal lattice,
2. Occlusion of vacant lattice positions caused by structural defects,
3. Inclusions occupying spaces between interstitial planes (i.e., impurities),
4. And adsorption onto growing crystals due to residual ionic charges (Banner, 1995; Veizer, 1983).

Substitution for Ca^{2+} by Sr^{2+} has been shown experimentally to be the main pathway for Sr incorporation into carbonate minerals with the other three factors proven to be random occurrences and overall, insignificant in terms of their contribution to the net Sr concentration in carbonates (Banner, 1995). The ionic radius of Sr^{2+} is 1.13 Å, which is only 15% larger than the ionic radius of Ca^{2+} (0.99 Å) in six-fold coordination and this enables Sr^{2+} to substitute for Ca^{2+} in calcium-bearing minerals (Faure & Mensing, 2005). However, the ionic radii differences cause Sr^{2+} to preferentially occupy eightfold coordination sites while Ca^{2+} can occupy six- and eight-fold lattice positions (Faure & Powell, 1972). For this reason, incorporation of Sr^{2+} into the crystal lattice of calcium-bearing minerals is partially controlled by the crystal structure (Faure & Mensing, 2005). Aragonite contains higher Sr content than calcite even when they precipitate from the same fluid. This is caused by differences in the crystal structures of the two polymorphs (Carpenter & Lohmann, 1992). Aragonite has an orthorhombic structure with ninefold coordination, which results in the site occupied by Ca^{2+} being larger than that of sixfold coordinated, rhombohedral calcite structure (Veizer, 1989; Banner 1995). Since Sr^{2+} has a larger ionic radius than Ca^{2+}, the substitution rate is faster in the orthorhombic structure. Moreover, calcite can precipitate as high-Mg or low-Mg calcite and higher Mg contents are also associated with higher Sr contents (Mucci, 1986; Mucci & Morse, 1983). This is due to distortion of the calcite crystal lattice induced by Mg^{2+} (0.65Å) substituting for Ca^{2+} (1.13Å) in eight-fold coordination, which leads to an increase in neighbouring cation site sizes (Carpenter et al., 1991, Carpenter & Lohmann, 1992). This facilitates increased assimilation of Sr^{2+} (Mucci & Morse, 1983).

2.5.1.2 Distribution coefficient

Distribution coefficients are used to quantitatively describe Sr partitioning between carbonate minerals and fluid phases (Veizer, 1983; Banner, 1995). The distribution coefficient (or partition coefficient, K_D^{Sr-Ca}) denotes the difference in ratio of Sr to Ca between a mineral and the fluid from which it is precipitating i.e. (Banner, 1995; Carpenter & Lohmann, 1992):

$$K_D^{Sr-Ca} = \frac{(Sr/Ca)_{Mineral}}{(Sr/Ca)_{Solution}}$$

Carbonate minerals with K_D^{Sr-Ca} < 1 will have lower Sr concentrations than minerals with K_D^{Sr-Ca} > 1 (Veizer, 1983).

Experimental and empirical K_D^{Sr-Ca} values for Sr in aragonite cements and skeletal fossils are in agreement and approximate unity ($K_D^{Sr-Ca} \cong 1$) (Veizer, 1983; Banner, 1995 and references therein). This suggests that precipitation of aragonite occurs under near-equilibrium conditions and Sr is mostly evenly distributed between the solid and liquid phase. It should be noted that vital effects, e.g. mechanisms of skeletal secretion and compositions of metabolic fluids, have the potential to affect partitioning behaviour of Sr in biogenic aragonite (Banner, 1995).

In contrast, experimental K_D^{Sr-Ca} values for Sr partitioning in calcite are dependent on Mg. High-Mg calcite has a K_D^{Sr-Ca} value of 0.146 (Mucci & Morse, 1983) while low-Mg calcite has a lower K_D^{Sr-Ca} of 0.14 (Holland et al., 1964 in Banner, 1995). Recrystallisation of aragonite to calcite also affects Sr partitioning and a K_D^{Sr-Ca} value of 0.045 has been reported (Banner, 1995). Moreover, the rate of precipitation affects partition coefficient values.

2.5.1.3 Effect of calcite precipitation rate on strontium concentration

There is a 1250 ppm offset in Sr content between biotic and abiotic calcite for a given Mg content (Carpenter & Lohmann, 1992). The higher Sr content in biotic calcite is likely due to the higher precipitation rate. The dependence of K_D^{Sr} (i.e. $[Sr]_{Mineral}/[Sr]_{Solution}$), and by definition, concentration of Sr in calcite, on the precipitation rate has been collaborated by several authors (see Ullmann, 2016 and references therein). When precipitation rates are high there is reduced selectivity for cations being incorporated into the calcite crystal structure and as such, substitution rates of Sr^{2+} for Ca^{2+} are high (Banner, 1995; Carpenter et al., 1991). Thus, it has been shown that low K_D^{Sr} values of abiotic calcite approximate equilibrium precipitation conditions while the high K_D^{Sr} values of biotic calcite are caused by kinetic effects in the same way that vital effects cause fractionation of carbon and oxygen isotopes in biotic carbonates (Carpenter & Lohmann, 1992).

2.5.2 Strontium isotope systematics

The Sr isotopic composition of seawater is primarily controlled by two sources: continental input and upper mantle influx (Elderfield, 1986). Continental input is through dissolved Sr sourced from chemical weathering of terrestrial rocks and is delivered to oceans predominantly through riverine runoff, although groundwater input is also influential (Palmer & Edmond, 1989; Veizer, 1989). Sr from the upper mantle is supplied to marine waters through mid-ocean ridge hydrothermal activity and weathering of oceanic crust basalts

(Elderfield, 1986; J. M. McArthur et al., 2012; Veizer et al., 1999). The composition of Sr isotopes of these two sources differs due to differences in the initial ratio of non-radiogenic ^{86}Sr to ^{87}Rb, the radioactive parent isotope to ^{87}Sr, and also their ages (Elderfield, 1986). At the onset of the delineation of the crust from the mantle during Earths early history, Rb, which behaves like an incompatible element during fractional crystallization, was excluded from the early forming basaltic rocks and thus became enriched in the residual silicic melts which formed the continental crust (Veizer, 1989; Elderfield, 1986). Since ^{87}Rb decays to ^{87}Sr, continental crust has a higher $^{87}Sr/^{86}Sr$ ratio (presently at ~0.712) than mid-oceanic ridge basalts (presently at ~0.7035) (McArthur, 1994; Richter et al., 1992) and this has resulted in a mean modern seawater ratio of 0.7092 (Elderfield, 1986). The $^{87}Sr/^{86}Sr$ composition of the ocean is considered to be homogenous due to the long residence time of Sr (~3 – 5 Myr) compared to the mixing time of the ocean (~10^3 yr) although this cannot be verified for ancient oceans where circulation may have been more sluggish or stratified (e.g., oceanic anoxic events – OAEs) (Halverson, 2007; McArthur, 1994).

2.5.3 Processes that control continental weathering

The oscillations in $^{87}Sr/^{86}Sr$ composition are primarily due to changes in continental flux into global oceans because changes in the hydrothermal fluxes are too small to account for the observed changes, especially post-Archean when old continental crust increasingly became the dominant source of weathering material (Allègre et al., 2010; McArthur, 1994; Richter et al., 1992; Shields, 2007). Therefore, processes affecting the weathering of continental crust control the strontium isotope composition of seawater and operate on geological timescales ranging from a few million years to tens of million years. Ultimately, three processes influence the rate of weathering and erosion as well as the type of material being eroded and these processes are: plate tectonics, atmospheric pCO_2 and palaeogeography (i.e., geographic location of continents at different times during the course of Earth's geological history) (Cawood et al., 2018; Shields, 2007; Walker et al., 1981). These broad categorisations encompass other sub-processes and create feedback loops such that the three processes influence each other.

2.5.3.1 Plate tectonics

Although the timing of the onset of plate tectonics is still debated, the mechanisms associated with plate tectonics were likely in place by the end of the Archaean (Brown, 2006; Brown et

al., 2020; Greber et al., 2017; Hawkesworth et al., 2017, 2020; Taylor & McLennan, 1985), although see (Stern, 2005, 2018) for an alternative view. Tectonic collision and rifting influence both the rate of weathering and the rock types being weathered. Collision of continental plates is accompanied by metamorphism and deformation and leads to uplift. Metamorphism and deformation lead to CO_2 degassing as well as alteration of Sr bearing minerals to more mobile minerals, both of which increase weathering rates (Chen et al., 2022; Cox et al., 2016; Richter et al., 1992; Schaller et al., 2012). Uplift exposes older rocks, which tend to have higher $^{87}Sr/^{86}Sr$ ratios, and also increases rates of runoff (Richter et al., 1992). Continental plate collisions therefore increase the flux of continental strontium, as well as increasing the average $^{87}Sr/^{86}Sr$ of that flux.

Continental rifting also influences seawater strontium isotope composition but in a different way to plate collisions. Initially, rifting exposes older rocks with high $^{87}Sr/^{86}Sr$ values, which upon weathering and transportation, can elevate seawater $^{87}Sr/^{86}Sr$ (Goddéris et al., 2017; Zhou et al., 2020). Rifting may progress into emplacement of continental flood basalts (CFBs) or large igneous provinces (LIPs), which have low $^{87}Sr/^{86}Sr$ due to their mantle origin. These basalts are highly susceptible to weathering (Cox et al., 2016). Consequently, emplacement of CFBs may decrease supply of radiogenic Sr to oceans, lowering seawater $^{87}Sr/^{86}Sr$, depending on the size and lifespan of the CFBs (Halverson et al., 2007). CFBs are also associated with CO_2 degassing, which increases pCO_2, in turn increasing rates of continental weathering (Cox et al., 2016). Earth alternates between periods of global rifting and global collisions over long timescales, depending on the Wilson Cycle (supercontinent cycle) and CFB are usually emplaced during periods of continental rifting.

2.5.3.2 Palaeogeography

Since the inception of plate tectonics, the continuous drift of landmasses has carried them to different latitudes with variable climatic conditions (Goddéris et al., 2017). Therefore, at certain times in Earth's history, older rocks with high $^{87}Sr/^{86}Sr$ values wandered into hot, wet, low latitude climates, where they were exposed to higher rates of erosion. Conversely, exposure of juvenile rocks to low latitude climates would have increased the supply of low $^{87}Sr/^{86}Sr$ to global oceans. Drift into cool, dry, high latitude areas would have drastically reduced rates of continental weathering and erosion, regardless of the exposed lithologies. Further, during periods of supercontinent assembly, shifting of weather systems drives

rainfall from continent interiors (Goddéris et al., 2017; Rooney et al., 2015). This results in reduced precipitation over the large swathes of continental landmasses leading to reduced run-off and weathering.

2.5.3.3 Atmospheric carbon dioxide partial pressure (pCO_2)

The partial pressure of atmospheric carbon dioxide is controlled by a negative feedback mechanism – the rate of silicate weathering increases with surface temperature, which in turn increases with the partial pressure of carbon dioxide (Colbourn et al., 2015; Walker et al., 1981). Silicate weathering draws down atmospheric CO_2, and the resultant ions are then transported to the ocean (Schaller et al., 2011). The process of carbonate precipitation, although a net carbon sink process, releases CO_2 back to the atmosphere. These processes keep pCO_2 within certain limits, preventing runaway greenhouse or icehouse conditions (Schaller et al., 2012; Walker et al., 1981). This feedback mechanism is stable over long geological timescales but is prone to short-term disruption by other natural phenomena like CFB emplacement and arc volcanism (Halverson et al., 2007; Allégre et al., 2010). The influx of mantle CO_2 into the atmosphere increases surface temperatures, which in turn results in increased weathering. The high susceptibility of basalts to weathering leads to rapid draw down of CO_2 and this is exacerbated in tropical regions where humidity and temperatures are high (Cox et al., 2016). If the rate of weathering outpaces the rate of carbonate formation, atmospheric pCO_2 will decrease, eventually leading to a drop in surface temperatures and weathering (Cox et al., 2016; Rooney et al., 2015). A return to steady state would then depend on the duration of the CFB, its size and geographic location. These changes would be recorded by seawater $^{87}Sr/^{86}Sr$, but would also have an impact on the climate and biosphere. Therefore, secular changes in seawater $^{87}Sr/^{86}Sr$ have the potential to track changes in past climate and environment, and their impact on biological evolution and mass extinction events.

2.5.4 Strontium isotope stratigraphy (SIS)

Wickman, (1948) first postulated that the ratio of marine $^{87}Sr/^{86}Sr$ varies across geologic time. Decades later, Peterman et al., (1970) generated the seminal record of Sr isotope composition variations for the Phanerozoic which along with subsequent studies (Faure et al., 1978; Spooner, 1976; Veizer & Compston, 1974), highlighted the nature of isotope shifts through geologic time and their likely causes. This culminated in the first comprehensive curve of $^{87}Sr/^{86}Sr$ for Phanerozoic seawater by Burke et al., (1982). DePaolo & Ingram, (1985) further

demonstrated that variations in marine strontium isotope composition through time could be used as a tool for stratigraphic correlation and dating. The increase in number of well-preserved samples from different geographic locations as well as improvement in Sr isotopes analytical techniques and instrumentation has led to improved reconstruction of $^{87}Sr/^{86}Sr$ curves for the Phanerozoic (e.g. McArthur & Howarth, 2005; McArthur, 1994; McArthur et al., 2012; Veizer et al., 1997, 1999) and the Precambrian (e.g. Chen et al., 2022; Halverson et al., 2007; Shields & Veizer, 2002). Reconstruction of Precambrian seawater $^{87}Sr/^{86}Sr$ has historically been beset by the paucity of well-preserved marine carbonates, large age uncertainities and the absence of skeletal fossils with modern day correlatives (Veizer, 1997, Shields & Veizer, 2002). Furthermore, depositional settings present unique challenges – e.g., continental margins are prone to folding and deformation during tectonic convergence, while intra-cratonic environments are likely to yield non-open marine carbonates which are especially susceptible to meteoric diagenesis (Chen et al., 2022). For these reasons, Precambrian SIS studies are limited to diagenetically well-preserved bulk rock samples of carbonates and other chemical precipitates (Shields & Veizer, 2002). Careful sampling and analysis yield $^{87}Sr/^{86}Sr$ ratios which can be used for (1) tracking long term changes in climatic, biological and tectonic activities; (2) determining numerical ages of unknown samples by comparing with known global seawater $^{87}Sr/^{86}Sr$ curve; and (3) diagenetic screening and distinguishing marine from non-marine carbonates, provided the ages of the samples are known (Chen et al., 2022; Halverson et al., 2007, Veizer, 1999).

2.6 Preservation and diagenesis

Marine carbonates are thought to faithfully capture seawater Sr signal but diagenesis could potentially alter the signal away from primary seawater values (Brand & Veizer, 1980; Wendler, 2013). Therefore, it is important to understand diagenetic processes, especially how they affect the Sr system. Diagenesis refers to all the processes that affect sediment after it has been deposited (Marshall, 1992). Understanding these diagenetic processes is important for differentiating primary geochemical characteristics from diagenetic artefacts (Marshall, 1992). Achieving this is not always straightforward but when carried out correctly, it helps to reconstruct palaeoenvironments, which in the case of this research project are ancient marine environments.

2.6.1 Diagenetic potential

Diagenetic potential denotes the possibility of a sedimentary rock (carbonates from this point onwards), experiencing significant pervasive alteration in relation to the solubility and reactivity of the minerals which constitute the primary sediment (Marshall, 1992). Mineralogy plays an important role because low-Mg calcite is considerably less soluble than aragonite or high-Mg calcite, and consequently, is less reactive (Wendler, 2013; Banner, 1995; Marshall, 1992). Particle sizes are also significant: small grains of low-Mg calcite have a higher solubility potential than large grained particles (Marshall, 1992). Regardless of particle size, low-Mg calcites are commonly well-preserved whereas high-Mg calcite and aragonite usually recrystallize to low-Mg calcite, a process known as neomorphism.

2.6.2 Diagenetic processes

There are several diagenetic processes, some which are well constrained and others that are not well understood. However, the processes of cementation and recrystallization are the most common causes of elemental and isotopic changes (Marshall, 1992).

2.6.2.1 Cementation

Cementation is the process of passive precipitation of minerals in sediment pore spaces. The precipitating minerals will inherit the elemental and isotopic composition of the pore fluids (Marshall, 1992; Banner 1995). Therefore, a shift in the average chemical composition will occur if the pore fluid is compositionally different from seawater (Carpenter et al., 1991). This will depend on whether the cements are early stage, when pore fluids are still an open system with respect to seawater, or late stage, when pore fluids are part of a closed system that has evolved away from seawater (Banner, 1995). Identifying diagenetic cements is thus important when seeking to obtain primary chemical composition data from carbonates.

2.6.2.2 Recrystallization

Rocks in disequilibrium with their environment will undergo physical and chemical changes in order to attain equilibrium (Marshall, 1992). One way of reaching equilibrium is by precipitation of new crystalline fabrics in place of pre-existing, unstable minerals (Carpenter & Lohmann, 1992; Carpenter et al., 1991). Due to slow reaction kinetics of solid-state processes, sedimentary systems preferentially equilibrate via dissolution of unstable phases and subsequent precipitation of more stable ones (Banner, 1995). Recrystallization is not always accompanied by change in mineralogy; it sometimes occurs as a change in grain size where fine grained metastable particles are replaced by stable crystalline fabrics (Marshall,

1992; Carpenter et al., 1991; Banner, 1995). In the same manner as cementation, pore fluids play an important role in the chemical composition of minerals formed through recrystallization (Marshall, 1992; Banner 1995). The shift in chemical composition is dependent on:

1. Variations between recrystallization environment and original carbonate formation environment,
2. Water-rock ratio of diagenetic system i.e., open or closed system dynamics,
3. Isotopic fractionation and trace element K_D's during precipitation of new carbonate minerals (Banner, 1995).

As a general observation, open systems with associated high water-rock ratios result in loss of primary chemical compositions signals. Exceptions exist and require adequate attention; for example, organic carbon-rich sediments trapped in a closed system may cause shifts in $\delta^{13}C$ composition of the newly formed carbonate if diagenetic recrystallization occurs at the same time as the breakdown of the organic carbon (Banner 1995).

2.6.3 Diagenesis environments and isotopic shifts

2.6.3.1 Shallow burial diagenesis

Stabilization of aragonite and high-Mg calcite through neomorphism to low-Mg calcite begins within the first few metres of burial and can result in loss of strontium and magnesium to the overlying water column (Tucker & Wright, 1990). Sediments which attain mineralogical stability under these conditions preserve a marine isotopic composition since recrystallisation occurs in contact with overlying seawater (Marshall, 1992). Low to non-existent recrystallization and cementation during shallow diagenesis makes carbonates susceptible to further diagenetic alteration (Marshall, 1992).

2.6.3.2 Shallow meteoric diagenesis

Interaction with meteoric water in shallow marine environments may alter the geochemical composition of carbonates. Meteoric water has different chemistry compared to seawater and pervasive dissolution, recrystallisation and cementation of limestone in the presence of such fluids may result in loss of primary trace elements and isotopic signals (Brand & Veizer, 1980; Marshall, 1992). Carbonates are more susceptible to meteoric diagenesis during periods of sea level fall because exposure occurs before stabilization of the carbonate phases

is complete (Marshall, 1992). Meteoric processes lead to depletion in elements such as strontium and sodium in carbonate sediments, but enrichment in others such as iron and manganese (Brand & Veizer, 1980). Isotopically, meteoric water has low $\delta^{18}O$ while its $\delta^{13}C$ varies depending on the carbon source (Marshall, 1992). Meteoric processes taking place in environments which are close to terrestrial vegetation will lead to depletion in ^{13}C while processes occurring in environments which are removed from vegetation horizons are enriched in ^{13}C and approach marine values (Tucker and Wright, 1990; Marshall, 1992). Therefore, carbonate cements and matrices altered by meteoric diagenesis will have low $\delta^{18}O$ and variable $\delta^{13}C$ (Marshall, 1992).

2.6.3.3 Deep Burial Diagenesis

As carbonate sediments are buried, they become isolated from surface water and diagenesis is controlled by fluid chemical potential and movement, as well as localized pressure induced dissolution and reprecipitation (Tucker and Wright, 1990; Marshall, 1992). Burial diagenesis extinguishes remnant unstable mineral phases and produces $CaCO_3$ saturated fluids (Marshall, 1992). Since deep burial diagenesis is effectively a closed system, cements precipitated from pore fluids will inherit $\delta^{13}C$ of the bulk rock due to low water-rock ratios (Banner, 1995; Banner & Hanson, 1990; Marshall, 1992). However, due to higher temperatures and the depleted $\delta^{18}O$ of pore waters, $\delta^{18}O$ decreases as equilibration occurs between the carbonate solid and pore fluids (Tucker and Wright, 1990; Marshall, 1992). Introduction of organic sources of carbon as well as deep, ^{18}O enriched waters released during compaction may induce reversals in the isotopic composition of carbonates during deep burial diagenesis (Marshall, 1992). There is mounting evidence that $\delta^{13}C$ can be affected during early-stage diagenesis, particularly in shallow marine environments (Higgins et al., 2018; Ahm et al., 2019). A detailed discussion of this is however beyond the scope of this research project.

2.6.4 Trace element behaviour during diagenesis

Elemental shifts during diagenesis are controlled by (1) the source of diagenetic fluid, (2) partition coefficients (3) the water/rock ratio (Banner & Hanson, 1990; Veizer, 2018). For Ediacaran carbonates, understanding meteoric diagenetic alteration is of great importance because, as is usually the case for the Precambrian, these carbonates were deposited in shallow marine environments where alteration by meteoric fluids is prevalent (Marshall,

1992). Meteoric waters are saturated in low-Mg calcite but undersaturated in aragonite and high-Mg calcite and thus dissolve the latter two and precipitate diagenetic low-Mg calcite (Veizer, 1983). Further, interaction of marine carbonate with meteoric water creates shifts in trace element composition (Veizer, 2018). Sr and Na have $K_D < 1$ in calcite crystals and will favourably partition into fluid phases leading to lowering of their concentration in the resultant diagenetic low-Mg calcite (Brand & Veizer, 1980). Mn and Fe have $K_D > 1$ for calcite and will preferentially partition into the calcite crystal lattice during precipitation and will thus be enriched in calcite than in the fluid from which the calcite is precipitating (Banner & Hanson, 1990; Brand & Veizer, 1980; Veizer, 1983). The extent to which these shifts occur will be limited by the water/rock ratio – when the ratio is high (open system) the shifts are pronounced while low ratios (closed system) produce minimal shifts (Banner & Hanson, 1990; Veizer, 1983). Closed systems largely preserve seawater concentrations of trace elements while open systems have trace element compositions which are significantly different from the primary carbonate (Brand & Veizer, 1980). Detrital or other non-carbonate marine particles can also affect trace element composition of diagenetic low-Mg calcite if they are present during diagenesis, and as such, may produce shifts that mimic those of diagenetic fluids, but these usually occur on a small scale (Banner & Hanson, 1990). Furthermore, redox conditions can affect Mn and Fe compositions. For instance, high Mn/Sr and Fe/Sr ratios may result from precipitation of carbonate from anoxic waters which reduce Mn and Fe to more soluble forms and thus increases their concentrations in such waters (Canfield & Thamdrup, 2009; McArthur, 1994).

3 Chapter 3: Study area and sample preparation

3.1 Geology of Neint Nababeep Plateau

The Neint Nababeep Plateau lies between 28°39’ S and 28°54’ S, and 17°36’E and 17°39’ E. It is located in the Northern Cape Province of the Republic of South Africa, close to the border town of Vioolsdrif, and partially straddles the Namibian – South African border, which is defined by the Orange River (Figure 2). The plateau represents the most extensive outcrop of the Nama Group in South Africa, encompassing the Kuibis and Schwarzrand Subgroups, and is underlain by the Kalahari crystalline basement. The Kliphoek and Mooifontein members of the Kuibis Subgroup outcrop around the margins of the plateau, but they are less prominent than members of the Schwarzrand Subgroup. The Schwarzrand Subgroup consist of the Neiderhagen and Vingerbreek members of the Nudaus Formation; the Nasep, Huns, Feldschuhorn and Spitskopf members of the Urusis Formation, and the Nomstas Formation. Carbonate units of the Huns Member dominate across the length and width of Neint Nababeep but they are especially pronounced in the eastern, southern and western margins of the plateau. Spitskopf Member siliciclastics and carbonates are located in the south-eastern, central and northern regions of Neint Nababeep, with the Nomstas Formation outcropping in the central and northern areas of the plateau. The area is cross-cut by major NW-SE trending thrust faults and is more deformed and folded towards the North and North-West. There are no apparent unconformities or erosional surfaces in Neint Nababeep and thus the rock sequences represent continuous and uninterrupted deposition unlike the Zaris and Witputs sub-basins in southern Namibia (Saylor et al., 1995).

3.1.1 Zaris Formation

3.1.1.1 Kliphoek Member

Similar to southern Namibian basins, the Kliphoek Member is defined by pebbly to coarse grained cross-stratified sandstone. The rock sequence is consistent with a tidal current influenced, shallow marine deposition environment as evidenced by occurrence ripple mark structures (Saylor et al., 1995,1998).

3.1.1.2 Mooifontein Member

The Mooifontein is dominated by siliciclastic rocks with subordinate fine-grained grey to black limestone. This is different to the Mooifontein Member of the Zaris sub-basin in southern Namibia which is dominated by carbonates (Saylor et al., 1995). The limestone strata range

from ~1 to 3 m thick, with the thickest unit occurring at the top of the member. Medium to coarse grained sandstones are the dominant siliciclastic rocks with shale occurring as a 1 m thick subordinate unit. The sandstones occur as laterally continuous, thick beds of tabular geometry, with blocky parting units. Saylor et al. (1995) interpreted the Mooifontein Member as mainly subtidal due to thin bedding and paucity of evidence for strong flows and exposure. However, the presence of laterally continuous, thick siliciclastic units in the study area suggests a marginal-marine environment which was heavily influenced by deltaic or tidal currents (Saylor et al., 1995). *Cloudina* and *Namacalathus* fossils are present in the thinly bedded limestone layers of the Mooifontein Member. An ash layer is present just below the 3 m thick limestone unit at the top of the member which is very useful as it provides opportunity for acquiring absolute dates for the deposition of the Nama Supergroup carbonates.

3.1.2 Nudaus Formation

The Nudaus Member represents a succession of medium- to coarse-grained sandstone interbedded with lesser fine-grained sandstone and siltstone/shale. Nudaus Formation is subdivided into two members: Neiderhagen and Vingerbreek (Figure 3A).

3.1.2.1 Neiderhagen Member

The Neiderhagen Member is characterized by dominant medium- to coarse- grained sandstone interbedded with lesser siltstone and fine-grained sandstone. It has previously been interpreted as a highstand deposit (Saylor et al., 1995) based on work on southern Namibian Nama basins and the upward coarsening sequence observed at Neint Nababeep is consistent with that interpretation.

3.1.2.2 Vingerbreek Member

The Vingerbreek Member is characterized by dominant fine-grained sandstone interbedded with red and green shale and lesser medium- to coarse-grained sandstone, along with subordinate siltstone. A very thin layer of limestone and two ash layers have been reported (Nelson et al., 2022) but were not observed during the field excursion for this research project. The observed deposition sequences are consistent with mainly near-shore shoaling-upward cycles, deposited during lowstand to transgressive systems tracts (Saylor et al., 1995).

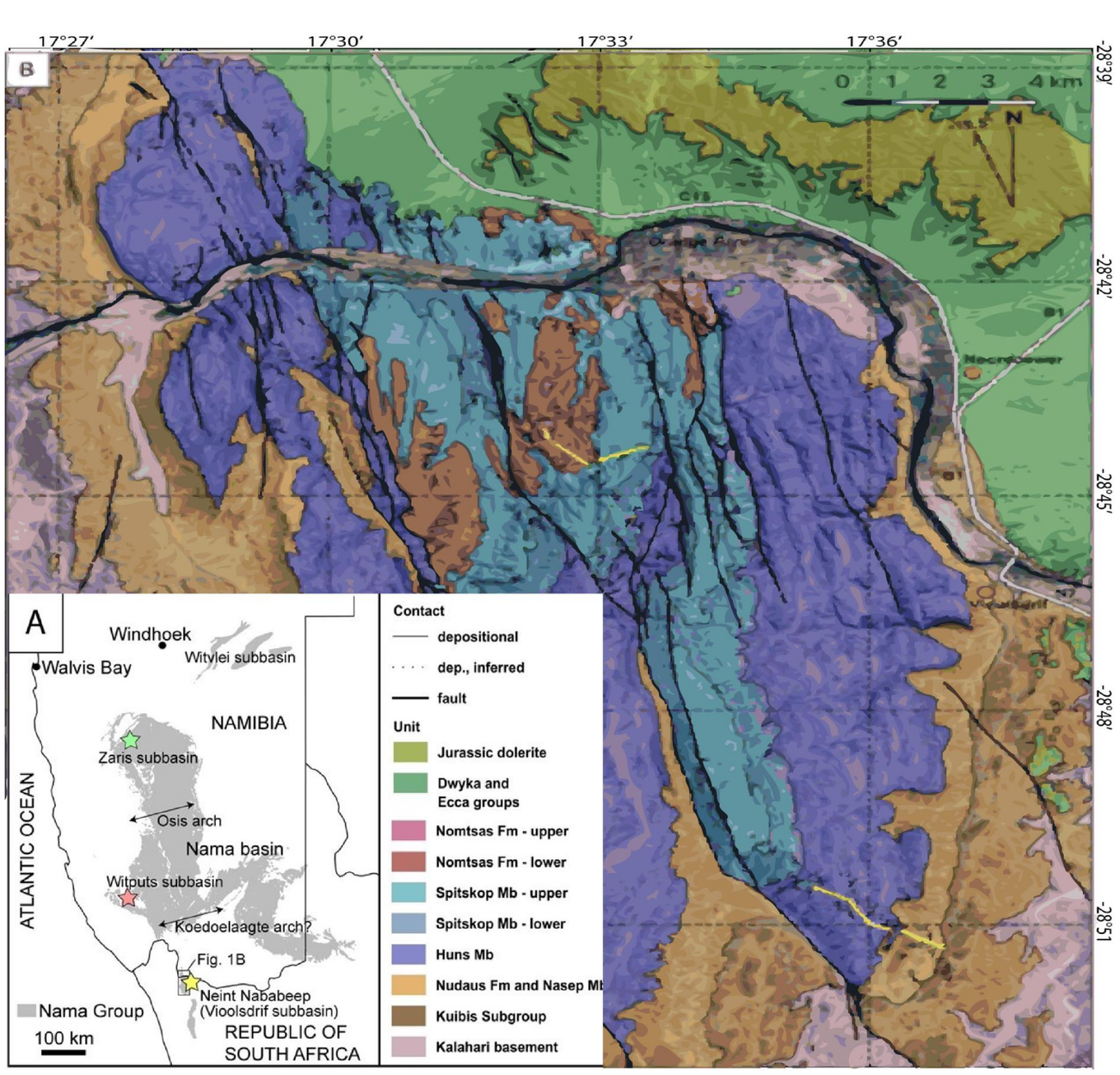

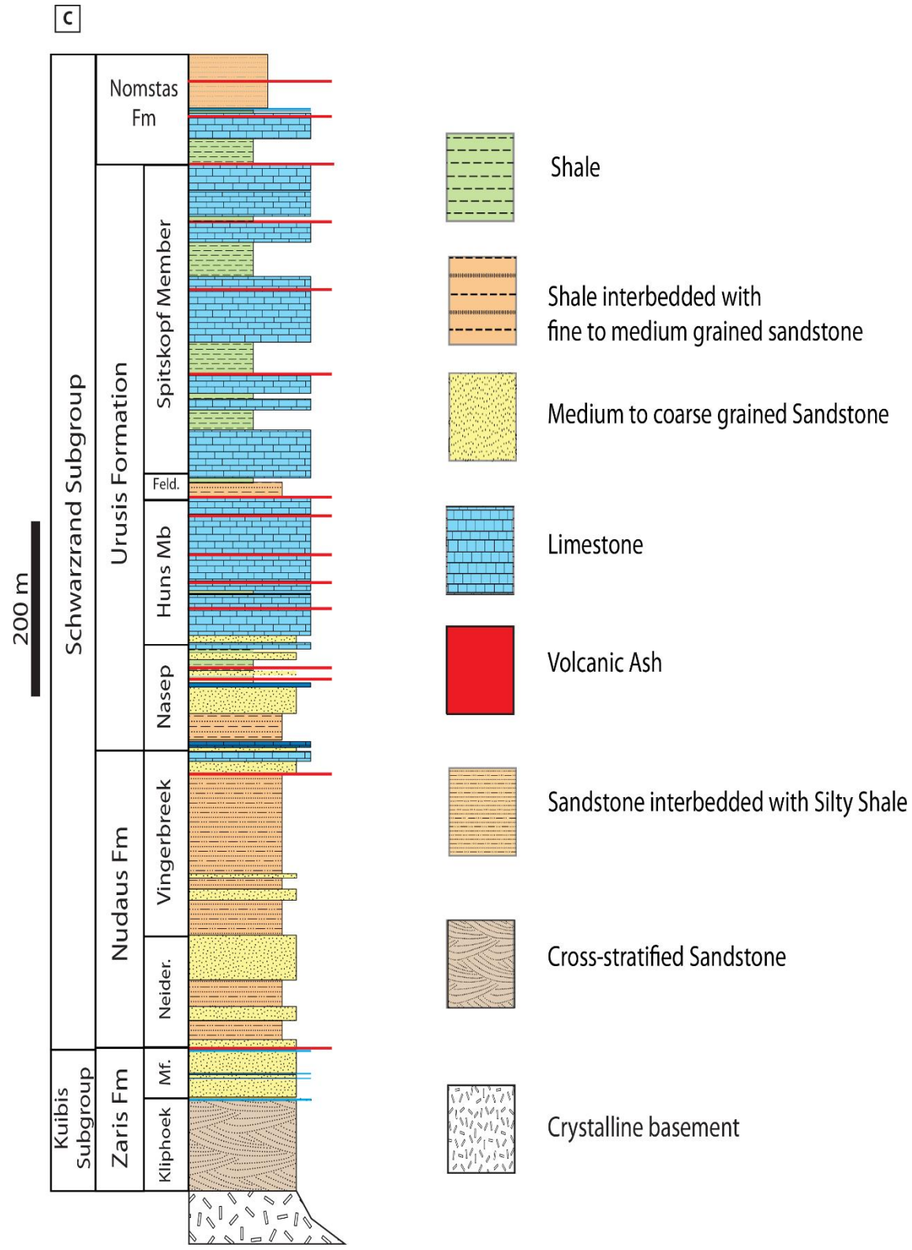

Figure 2: (A) Outcrop of Nama Group (grey) and location of key sites within South Africa and Namibia (orange yellow and green stars). (B) Detailed geological map of Neint Nababapeep Plateau from Nelson et al., (2022). Yellow paths are transects along which samples were collected. (C) Accompanying stratigraphic log constructed from field observations.

3.1.3 Urisis Formation

3.1.3.1 Nasep Member

The Nasep Member at Neint Nababeep plateau is characterized by siliciclastics with subordinate carbonate layers at the top of the member. Prominent sandstone ridges at the bottom of the member give way to green and sometimes purple and white shale. Near the top, shale is abruptly overlain by ~10 m thick sandstone which is in-turn succeeded by 5 m green shale. Successive layers of thin bedded limestone and shale follow, with a 2 m thick sandstone unit representing the boundary with the Huns Member. Overall, the Nasep Member represents an upward fining sequence and is interpreted as upper shoreface, deltaic environment which experienced persistent currents as evidenced by occurrence of hummocky cross-stratification structures in some of the sandstones (Saylor et al., 1995).

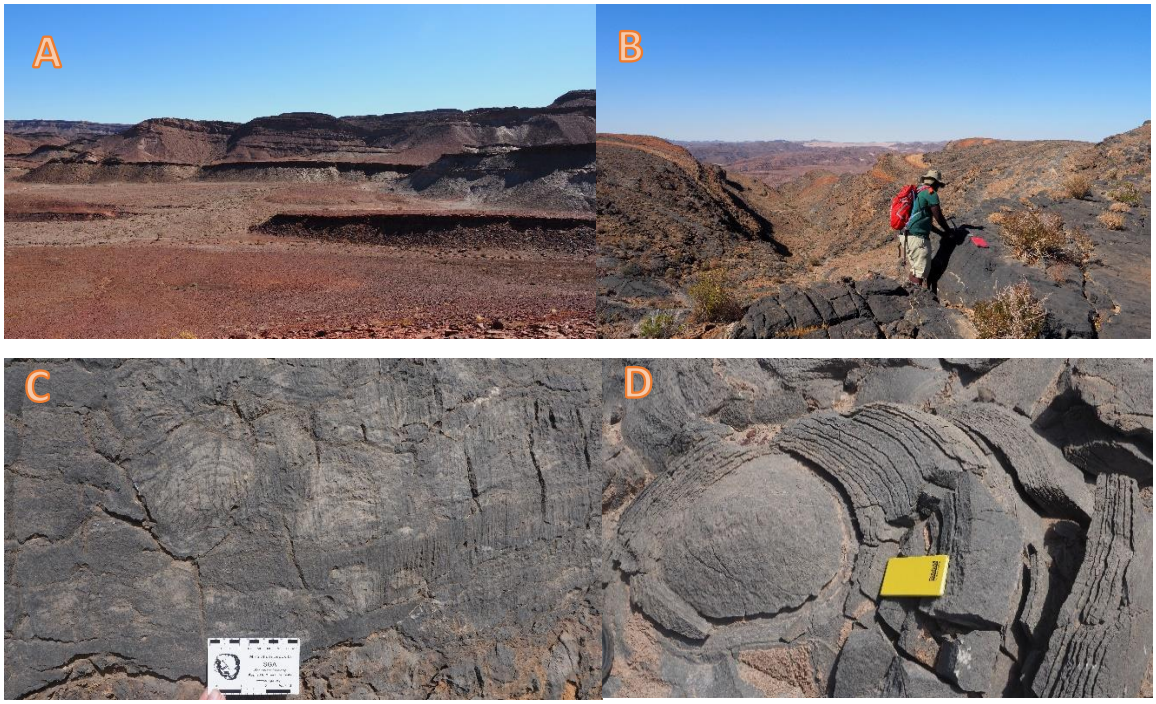

Figure 3: (A) Sandstone and Shale of Nudaus Formation. (B) Black limestone of Huns Member in the foreground and red/orange weathered ash horizons in the background. (C) Columnar stromatolites from the Spitskopf Member. (D) Stromatolite domes (onions) from the Spitskopf – Nomstas boundary.

3.1.3.2 Huns Member

The Huns Member is a succession of mostly massively bedded, laminated black limestone. Shales are sparse and occur as thin bedded layers ranging from a few centimetres up to 3 m and are mostly green although purple shale is also present. There are several ash layers (at least 4 but could be up to 7) and these are identified as red/orange weathered horizons or compact grey/green very fine-grained, blocky layers (Figure 3B). Thin bedded limestone

horizons are also present and usually yield fossils of *Cloudina*, unidentified calcified tubes and ooids. The carbonate platform of the Huns Member is consistent with a shallow marine environment with the platform developing during a prolonged period of sea level rise (Germs, 1983; Saylor et al., 1998).

3.1.3.3 Feldschuhorn Member

This member represents a small sequence (~20 m) of siliciclastic rocks, with green shale succeeded by sandstone and siltstone. This rock sequence is underlain by an ash layer. Presence of volcanic ash might signify sea level fall caused by tectonic activity which triggered heavy sediment input into shallow marine environments. The event was short lived as evidenced by the succeeding carbonate units of the Spitskopf Member.

3.1.3.4 Spitskopf Member

The Spitskopf Member is dominated by black limestone with individual layers ranging from 10 cm to >10 m. Shales are also present in sections and the stratigraphic thicknesses of these sections range from 1.5 to 48 m. The shales in the lower Spitskopf are grey and/or green but they transition to red and brown shales in the upper Spitskopf. The limestone facies include laminated, massive bedded, thin bedded and columnar stromatolic limestones. Massively bedded limestones are prominent in the lower Spitskopf and are generally fossil poor. Thin bedded limestones become ubiquitous in the upper Spitskopf and they are interbedded with the stromatolitic limestones. Huge domes typify stromatolitic limestone facies and these domes measure up to 3 m in length (Figure 3C). The domes usually have thrombolitic cores and stromatolitic outer layers and have as such been colloquially called “Onions”. *Cloudina* and other shelly and tubular skeletal fossils have been found in these stromatolite domes. The massively bedded limestones are similar to those of the Huns and suggest similar depositional conditions. Thin bedded limestone facies have been reported in Spitskopf limestones of the Namibian Nama basins and slope facies (Germs 1972,1986; Saylor et al., 1995) and were interpreted as resumption of limestone production, representing progradation of platform deposits across detrital deposits during sea-level highstand (Grammer & Ginsburg, 1992).

3.1.4 Nomstas Formation

The formation is markedly different from equivalent strata from Namibia. At Neint Nababeep, the Nomstas Formation has thin bedded and stromatolitic limestone facies, which are entirely

missing in its Namibian counterparts (Figure 3D). Interbedded with the limestones are green and red shales which are typically thin bedded and friable. Stromatolite domes are present just like in the underlying Spitskopf but skeletal fossils were not observed. Significantly, no erosional surface was discovered and this represents uninterrupted sediment deposition unlike in Namibian sequences.

3.2 Sampled sections

Sampling and logging were carried out over two field excursions in March 2020 (with Rosalie Tostevin and Wendy Taylor) and May 2021 (with RT and WT, plus Aidan Wilton). Samples were mostly collected from the carbonate rock dominated members of Mooifontein, Huns, Lower and Upper Spitskopf; as well as a few from the Nasep Member and Nomstas Formation. Shales were also collected from the Spitskopf Member and Nomstas Formation. In total, 111 samples were collected: carbonates, n = 98; shales, n =13. Samples were clearly labelled with their way up and placed into labelled bags. Stratigraphic logs were completed through transects and photographs taken of all key lithologies.

3.2.1 Mooifontein Member section (sample set ORMF-00)

The Mooifointein section (-28.86761; 017.61331 to -28.86685; 017.61233) was transected on 12/05/2021. The measured stratigraphic thickness of the sampled area is ~72 m from which 9 carbonate samples were collected. Frequency of sampling varied depending on the thickness of beds, with one sample collected from the thin beds and multiple samples collected from thicker beds. Large samples containing densley packed skeletal fossils were also collected for palaeontological work.

3.2.2 Huns section (Sample set ORH-00)

The transect through the Huns Member (-28.84818; 017.60605 to -28.84258; 017.58965) was completed on 13/05/2021. Although it mostly covered the Huns Member, the initial 63 m (-28.84818; 017.60605 to -28.84877; 017.60547) of the transect was from the Nasep member from which 3 carbonate samples were collected; one from a 1 m thick bed and 2 from a 6 m thick bed. To reach the base of the Huns involved climbing an extensive, steep scree slope, followed by some basic bouldering. In total, the transect took 12 hours to complete. Due to the preponderance of carbonate rocks in the Huns, samples were collected at intervals of 10 – 15 m or, in some cases, when a facies change was observed. A further 23 samples were thus collected, covering a stratigraphic thickness of 202 m.

3.2.3 Lower – Upper Spitskopf section (sample set ORLS-00)

The transect through the entire Lower Spitskopf and part of the Upper Spitskopf (-28.70490; 017.52569 to -28.70720; 017.52125) was the longest transect, covering a cumulative stratigraphic thickness of 384 m. It was completed over two days (11/03/2020 to 12/03/2020). Due to the generally gentle slopes of the rock outcrops, it was easy to traverse this section and this was coupled with higher rate of facies change, in comparison with the Huns Member, leading to increased frequency of sample collection. A total of 59 samples (carbonate n = 48, shale n = 11) were collected from this section.

3.2.4 Upper Spitskopf – Nomstas section (sample set ORSN-00)

Covering a stratigraphic thickness of 129 m (-28.72209; 017.54690 to -28.72305; 017.54474), this section represents the rocks at the top of the Nama Group stratigraphy of the study area. In total, 17 samples were collected on 13/03/2020 and comprised of carbonates (n = 15) and shales (n =2). The transect was markedly shorter than the previous Lower - Upper Spitskopf but had similar facies and topographic relief. As such, the two sections had comparable sampling resolutions.

3.3 Rock powdering

Preparation for rocks to be turned into powder started during sample collection. Only fresh samples were collected. Weathered or altered rocks were not sampled but were noted in the field notebook. The samples were further cleaned by sawing off edges which contained traces of weathered or altered materials which were missed during sampling. The samples were then crushed using a cast iron crusher in the University of Cape Town's Department of Geological Sciences crushing room. The cm – sized rock chippings were further assessed to remove any lingering non-pristine fragments. The painstakingly selected rock chippings were then ground into fine powder using a steel mill.

3.4 Thin section preparation

A total of 35 samples, from across the entire stratigraphy, were chosen to be made into thin sections. They were chosen based on field observations i.e., samples which were representative of the sampled sections and samples from rocks with important sedimentary and physical structures. The selected samples were sawed into two parts, one for thin sectioning and the other for geochemical analyses. The parts to be turned into thin sections were cut out into blocks and then mounted on glass using epoxy resin by Rene Van Der Merwe in the thin section lab at the University of Cape Town. The sizes of the blocks were further

reduced by cutting it down using a motorized blade. The trimmed samples were then ground down to a thickness of ~35 mm using a spinning wheel. The samples were further manually ground down to the desired thickness using super-fine, 600 grit silicon carbide powder. Samples were finally cleaned with ethanol.

3.5 Petrographic analysis

The rocks were described using Folk's Carbonate Classification (FCC) (Folk, 1980). According to this classification, carbonate rocks are classified as: microcrystalline calcite (micrite), sparry calcite or allochems. Micrite is limestone derived from carbonate mud, has grain size diameters ranging from 1 to 4 mm and has a dull appearance in thin section. Sparry calcite forms from recrystallization of micrite or as pore filling cement. Sparry calcite crystals are larger than micritic crystals and have a grain diameter >10 mm and appear clear in thin section. Allochems refer to allochemical constituents i.e., constituents which formed in the basin of deposition but were transported or if they were not transported, they contain aggregates of fossils or fecal pellets. Allochems names are prefixed by the dominant allochemical constituent and suffixed by the type of carbonate cement. For example, a limestone composed of fossils in a micrite matrix is called Biomicrite.

The carbonates are micritic to microsparry limestones across the entire stratigraphic sequence. In thin section, Micrite occurs as the primary matrix and is sometimes replaced by microspar and in some instances grades into sparry calcite (Figure 4A). Styolites, which represent pressure induced dissolution of calcite during diagenesis, are present especially in thin sections of samples from the Mooifontein Member (Figure 4B). There is also evidence of calcite recrystallization in previously formed styolites, indicating complex diagenetic processes (Figure 4C). Deformation fractures are also present and are filled by mostly sparry calcite but manganese nodules also occur, especially in Spitskopf Member thin sections. The manganese nodules do not occupy the spaces between calcite crystals but rather form on top of the calcite crystals and appear as dark brown, irregularly shaped crystals (Figure 4D).

The allochemical constituents identified in thin sections were ooids and intraclasts (Figure 4E). Ooids are 0.25 to 2 mm, laminated, concentric carbonate grains whose crystals grow in a spherical or radial orientation, around a nucleus, usually a detrital terrigenous grain or fossil fragment (Scholle & Ulmer-Scholle, 2003, p228). Occurrence of ooids in thin sections indicates that the prevalent conditions at the time of formation of the sediments were warm shallow

tropical marine waters which had high levels of carbonate saturation and pH, and had normal to moderate salinity (Diaz & Eberli, 2019). The ooid cortices have tangential crystal orientation indicating that they formed in a high energy intertidal or subtidal environment (Simone, 1980). The intraclasts have been almost entirely recrystallized to sparry calcite such that it is impossible to decipher the primary sedimentary structures.

In some of the thin sections, there are dark, thick patches which form veneers over the carbonate matrices (Figure 4D). The patches are difficult to deduce because they lack key diagnostic features used to classify carbonate sedimentary structures. Although the nature of these patches is unknown, they are likely responsible for the dark colour of the carbonates of Neint Nababeep Plateau.

3.6 Zebra River samples

The Zebra River section lies in the Zaris sub-basin of the Nama Group and consists of shallow marine carbonates interbedded with siliciclastic rocks of the Zaris Formation (Germs, 1995; Saylor et al., 1998). The Zebra River section has a thickness of ~500 m and two members of the Zaris Formation (Omkyk and Hoogland) are present (Saylor et al., 1998). The Omkyk and Hoogland members composed of dark micritic limestone which is comprised of stromatolitic, oolitic, pisolitic and oncolytic facies which are representative of barrier reef, barrier bar and forereef depositional environments (Gresse and Germs, 1993). The Urikos Member comprises siliciclastic rocks which were deposited in relatively deep basin to the north of the barriers (Gresse & Germs, 1993). These samples are important as they fill in the lower Nama section, which is carbonate dominated at Zebra River, but siliciclastic dominated at Neint Nababeep Plateau. These samples were inherited from Dr. Rosalie Tostevin and were already crushed, thin sectioned and analysed for trace elements and isotope data (Tostevin, 2015).

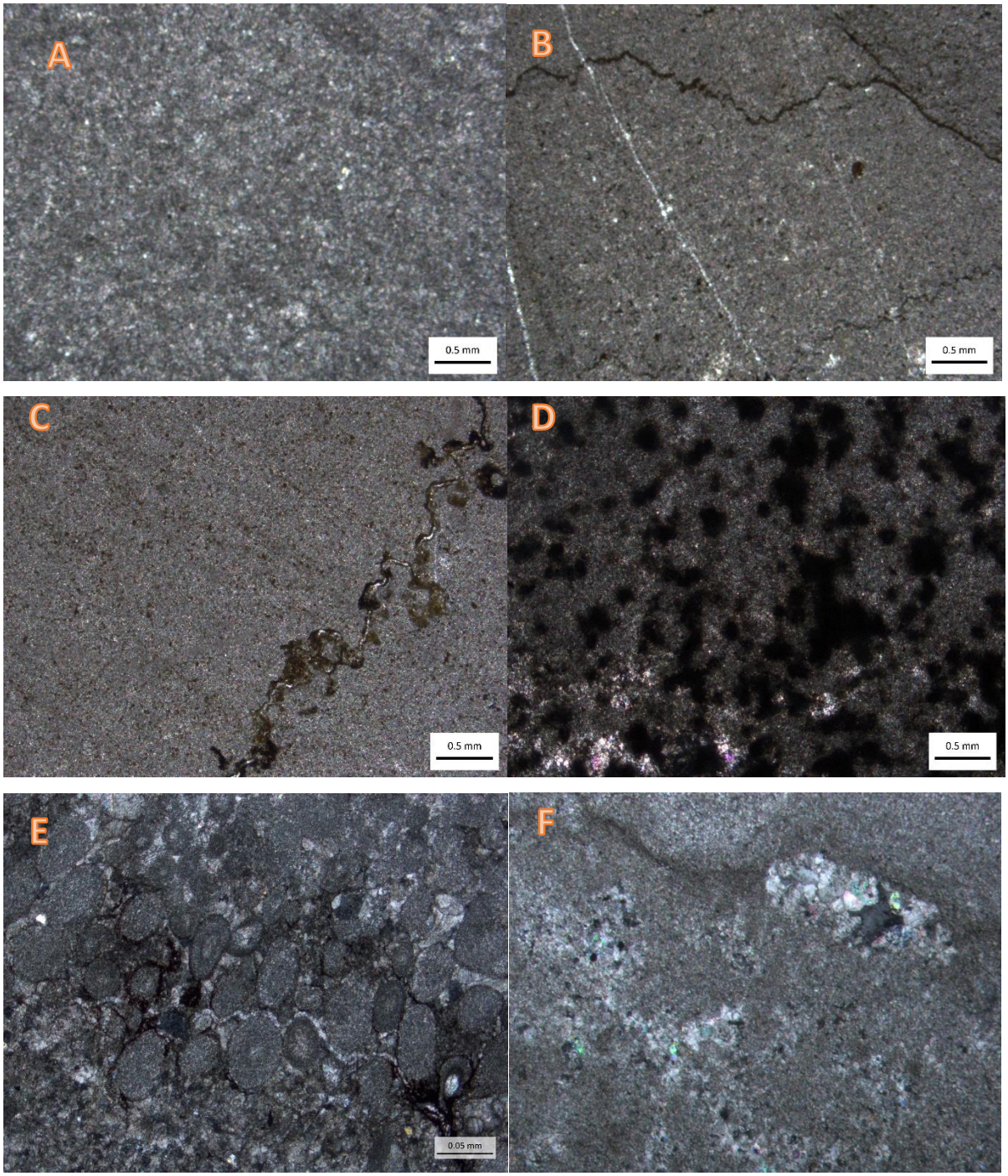

Figure 4: (A) Microspar crystals in dominant micritic matrix from Nomstas Formation (B) Styolite structure in micritic limestone showing evidence of calcite dissolution, micro-veins filled with sparry calcite run almost perpendicular to styolite feature from Mooifontein Member. (C) Styolite with recrystallized sparry calcite in micritic matrix from Mooifontein Member. (D) Dark unidentified veneer covering a micritic limestone from Huns Member. (E) Ooids in micrite matrix i.e., oomicrite limestone from Spitskopf Member. (F) A vein and void both filled with sparry calcite and have manganese nodules (dark-coloured crystals) growing on top of calcite crystals from Spitskopf. Photos A – D were taken under XPL and scale is 0.5 mm while E and F were taken under PPL and scale is 0.05 mm.

4 Chapter 4: Carbon and oxygen isotopes, trace and rare earth elements

4.1 Introduction

Chapter 2 provided an overview of the geochemical proxies used in this study. In this chapter, the focus will be on the analyses, results and interpretation of C, O isotopes, trace elements and REEs. C isotopes analysis was carried out for chemostratigraphy i.e., for correlation with regional Nama Group sections and global Ediacaran strata. Although C isotopes are largely resistant to diagenetic alteration in carbonates, care was still taken in sample selection. O isotopes were analysed along with C isotopes and the data were principally used for diagenetic screening as explained in Chapter 2. Similarly, trace elements data, particularly Mn, Fe and Rb, were used to ascertain the diagenetic alteration state of the samples and the possible effect on $^{87}Sr/^{86}Sr$ ratios. REEs data were also obtained and used to: (1) reconstruct local palaeoredox conditions and, (2) check whether the carbonates were deposited in an open marine environment. All these analyses were done within the context of attempting to obtain the best possible Sr isotopes data.

4.2 Analytical protocols

4.2.1 Carbon and oxygen isotopes

Approximately 0.2 mg of powdered sample was reacted with 100% H_3PO_4 at 72 °C in a Thermo Finnigan Model II gas bench to liberate CO_2. The reaction mixture was left to stand for a minimum of 2.5 hours and the evolved CO_2 was analysed using a Delta Plus XP isotope mass spectrometer at University of Cape Town. Internationally recommended standard materials (IAEA-CO-8 and Carrara Z) along with an in-house standard, Cavendish Marble ($\delta^{13}C$ = 0.34‰, $\delta^{18}O$ = -8.95‰), were routinely analysed to monitor accuracy and precision. Isotope ratios were reported in the delta notation relative to the Vienna PeeDee Belemnite (VPDB) standard in permil (‰). Raw data were calibrated using known $\delta^{13}C$ and $\delta^{18}O$ values for IAEA-CO-8, Carrara Z and Cavendish Marble standards. All data are in Appendix, Table 1.

4.2.2 Trace and rare earth elements

Trace and rare earth elements data from the Spitskopf (Upper and Lower) and Nomstas were inherited from Mashego, (2020) who analysed them as part of her Honours thesis (Appendix, Table 1). However, the method used was different to the sequential leaching used in this study project. The method used by Mashego was a single step dissolution technique and thus likely incorporated trace elements and REEs from non-carbonate phases. The data obtained were sufficient for the testing of Sr isotopes analytical protocol (see Chapter 5).

For the Mooifontein and Huns members, 34 samples were analysed using a sequential leaching method described in Tostevin et al., (2016). Approximately 25 mg of sample was weighed and washed with Milli-Q water and an appropriate amount of 1% HNO_3 was added to dissolve 20% (5 mg) of the sample (a theoretical purity of 100% was assumed). The sample was then shaken and left to stand for more than 30 minutes before it was centrifuged at 3000 rpm for 10 minutes. The supernatant was then decanted and the remaining solid sample was dried down. The sample was then treated again with enough 1% HNO_3 to dissolve a further 40% of the sample, and the mixture was shaken and left to stand for more than 30 minutes. The solution was then centrifuged at 3000 rpm for 10 minutes and ~640 ml was removed and passed through a 20 mm syringe filter(Cao et al., 2020) . The samples were dried down and then taken back up into solution using a stock solution of 5% HNO_3 containing 10 ppb of the following internal standards: In, Re, Rh and Bi. Samples were further diluted using the same HNO_3 solution and were analysed on a Thermo Fisher iCAP RQ ICP-MS and calibration curves were obtained from standard solutions made from synthetic standards.

4.3 Results and interpretation

4.3.1 Carbon isotopes for Neint Nababeep Plateau

$\delta^{13}C_{VPDB}$ in the Mooifontein Member ranges from -0.29‰ to +1.68‰ (n = 7). In the Huns Member, carbon isotopes values range from -10.90‰ to +3.04‰ (n = 26) although the outlying -10.90‰ value is likely due to analytical error. Excluding that anomalously low value, the mean and standard deviations all change significantly to 1.34‰ and 1.25‰ respectively, although the median value is relatively unchanged at 1.46‰. In the Lower Spitskopf Member, $\delta^{13}C$ ranges from -4.51‰ to +1.40‰ (n = 40). $\delta^{13}C$ in the Upper Spitskopf Member ranges from -0.35‰ to +1.56‰ (n = 14) and in the Nomstas Formation $\delta^{13}C$ ranges from -1.72‰ to +0.98‰ (n = 9) (Figure 5).

The highest $\delta^{13}C$ on the Neint Nababeep Plateau occur in the Huns Member carbonates (Figure 5). The occurrence of thick successions of siliciclastic deposits between the Mooifointein and Huns members, combined with the limited number of carbonate rock samples from the Mooifontein make it difficult to constrain any trend in $\delta^{13}C$ between the two sections. $\delta^{13}C$ in the Lower Spitskopf Member shows an initial decrease in comparison with the Huns Section but then gradually increases, with the upward trend continuing into

the Upper Spitskopf Member were the values peak. A steady decrease in $\delta^{13}C$ is then observed between the Upper Spitskopf and Nomstas Members.

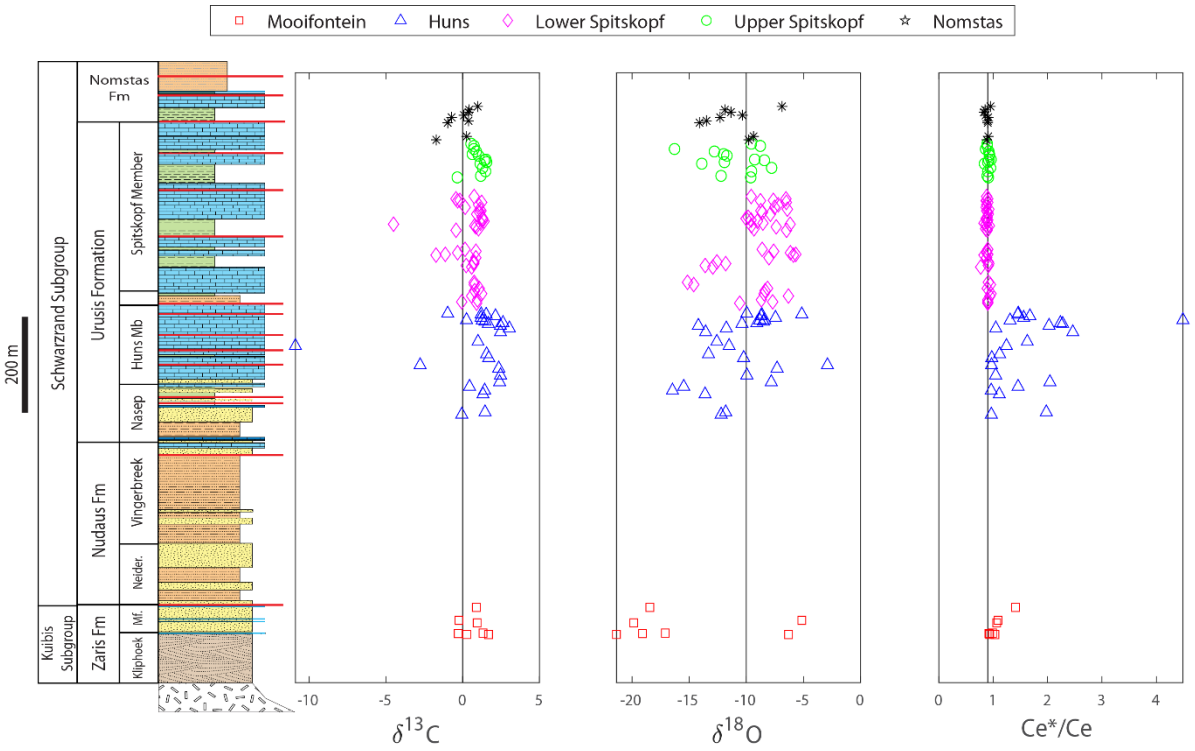

Figure 5: $\delta^{13}C$, $\delta^{18}O$ and Ce anomalies trends across the entire stratigraphy of Neint Nababeep Plateau. Klip = Kliphoek Member, Mooi. = Mooifontein Member, Feld. = Feldschuhorn Member

Overall, the carbon isotope trend through the entire stratigraphy of Neint Nababeep is similar to other Ediacaran carbonates from South Africa (Nelson et al., 2022), Namibia (Grotzinger et al., 1995; Wood et al., 2015), Oman (Fike et al., 2006), China (Jiang et al., 2007), Canada (Rooney et al., 2020) and Australia (Calver, 2000). The persistent positive $\delta^{13}C$ values are consistent with those of Witputs Basin, southern Namiba, where ash layers have yielded ages ranging from 540 Ma ± 0.99 Ma to 538.58 ± 0.19 Ma (Grotzinger et al., 1995; Linnemann et al., 2019). Crucially the $\delta^{13}C$ of the Spitskopf Member in Neint Nababeep is identical to the Swartpunt and Swartkloofberg sections of the Witputs Sub-basin, with a plateau known as late Ediacaran Positive Carbon Isotope Plateau (EPIP) (Bowyer et al., 2022; Linnemann et al., 2019). The correlation with other, well established, Ediacaran carbonates provides compelling evidence that the sampled sections represent a near-primary archive of ancient seawater $\delta^{13}C$ and that the Neint Nababeep Basin was connected to the global ocean (Bowyer et al. 2022). The close relationship with southern Namibian $\delta^{13}C$ trends strongly supports coeval deposition between the basins during the terminal Ediacaran.

4.3.2 Oxygen isotopes for Neint Nababeep Plateau

$\delta^{18}O$ in Mooifontein Member ranges from -21.37‰ to -5.14‰ (n = 7). Huns Member oxygen isotopes values range from -16.46‰ to -2.90‰ (n = 26). Lower and Upper Spitskopf sections have oxygen isotopes values ranging from -15.15‰ to -5.67‰ (n = 40) and -16.68‰ to -7.78‰ (n = 14) respectively, while values from Nomstas Formation range from -14.10‰ and -6.87‰ (n = 9) (Figure 5).

Samples from the Mooifontein Member are the most isotopically depleted and also show the most scatter (Figure 5). They also have values that are largely below -10‰, indicating that they have been heavily affected by diagenetic alteration (Kuznetsov et al., 2018). The isotope data are consistent with petrographic analysis which showed stylolites and sparry calcite filled micro-veins, indicating chemical leaching and mineral recrystallization which may have occurred during diagenesis or post-diagenesis (Figure 4C). Samples at the base of the Huns Member have low $\delta^{18}O$ (<-10‰) but gradually become enriched before stabilizing towards the top of the section. Small enrichments in $\delta^{18}O$ are observed throughout the Lower Spitskopf but generally the values remain constant across both the Lower and Upper Spitskopf before the values become depleted near the boundary between Upper Spitskopf and Nomstas. The downward trend in $\delta^{18}O$ persists across the Nomstas Formation.

$\delta^{18}O$ does not co-vary with $\delta^{13}C$ across the entire stratigraphy of Neint Nababeep (Figure 5). Further, as is the case with Ediacaran carbonates, there is paucity of fossils with known carbon and oxygen isotope fractionation behaviour. Therefore, it is difficult to reconstruct Palaeotemperatures of Ediacaran seawater as well as to ascertain the impact of climate fluctuations on the Ediacaran carbon cycle using $\delta^{18}O$ isotopes. In this thesis, they are only used to assess the extent of diagenetic alteration.

4.3.3 Trace elements

4.3.3.1 Kuibis Subgroup (Zaris Basin, Namibia)

Extensive trace elements data for Kuibis Subgroup in the Zaris sub-basin have been published (e.g. Tostevin et al., 2019a; Tostevin et al., 2016a). For the samples analysed for $^{87}Sr/^{86}Sr$ ratios, Sr concentrations range from 24 ppm to 1138 ppm (n = 18) Mn concentrations range from 36 ppm to 744 ppm (n = 18) (Figure 6). Fe concentrations range from 394 ppm to 2141 ppm (n = 18). Rb concentrations range from 0.23 ppm to 0.37 ppm (n = 2). Mn/Sr ratios range up to 1.80 (n = 18), Fe/Sr ratios range up to 37.44 (n = 18) and Rb/Sr ratios range up to 0.0013

(n = 2). Mn/Sr, Fe/Sr and Rb/Sr are mostly less than 2, 5 and 0.02 respectively. The discussion of trace elements from this stratigraphic section will be restricted to strontium isotopes data evaluation (see Chapter 6).

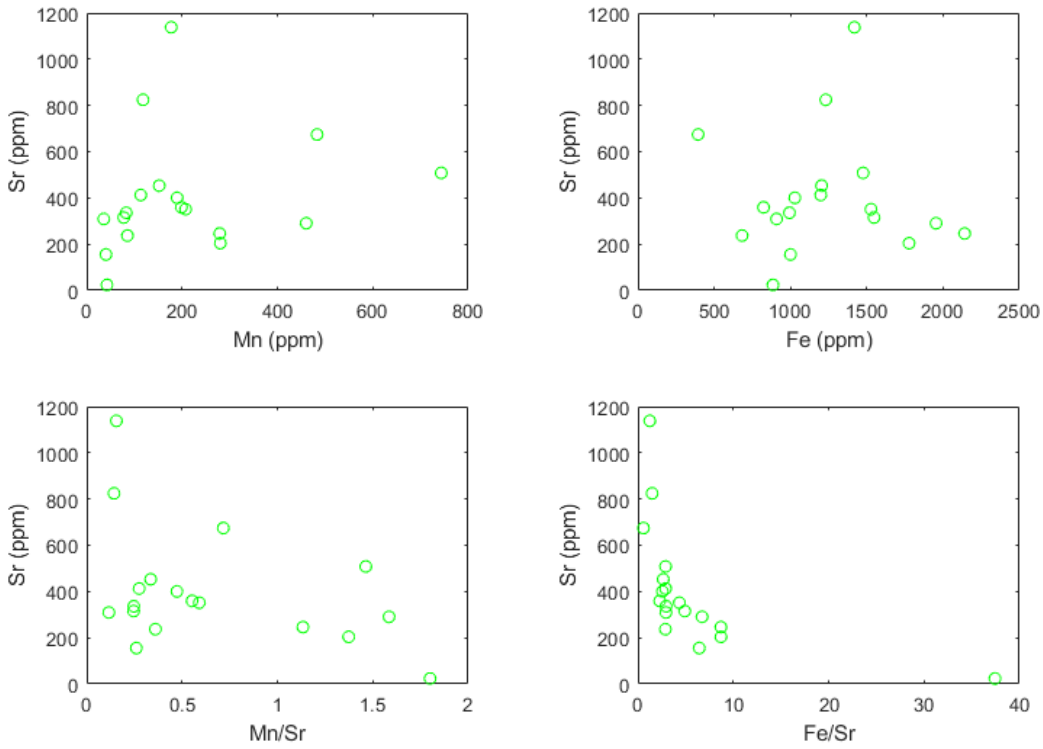

Figure 6: Cross plots for Kuibis Subgroup, Zebra River, Namibia

4.3.3.2 Schwarzrand Subgroup (Neint Nababeep Plateau, South Africa)

4.3.3.2.1 Mooifontein Member

Sr concentrations range from 24 ppm to 1606 ppm (n = 8). Mn concentrations range from 1072 ppm to 7183 ppm (n = 8). Fe concentrations range from 0.72 wt% ppm to 7.85 wt% (n = 8). Rb concentrations range from 0.10 ppm to 1.30 ppm (n =8). Mn/Sr ratios range up to 21 (n =8), Fe/Sr ratios range up to 179.30 (n = 8) and Rb/Sr ratios range up to 0.0033 (n = 8). Mn/Sr, Fe/Sr and Rb/Sr are very high with most values being greater than 2, 5 and 0.02 respectively (Figures 7 and 8).

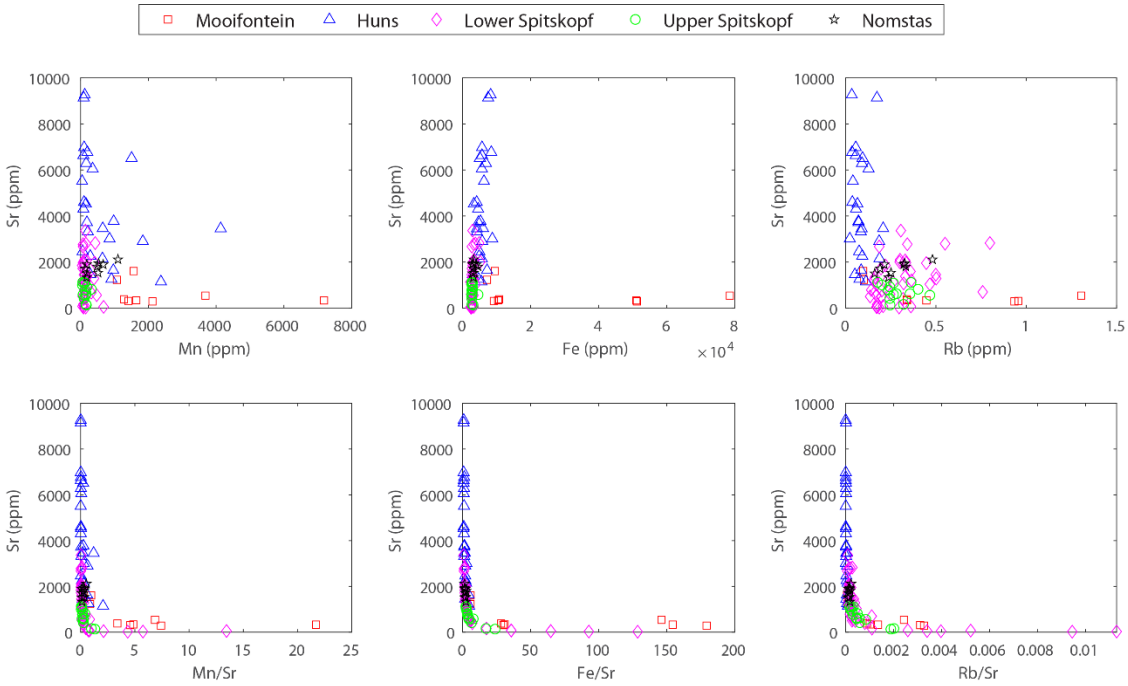

Figure 7: Trace elements cross plots for Neint Nababeep Plateau.

4.3.3.2.2 Huns Member

Sr concentrations range from 1147 ppm to 9261 ppm (n = 26). Mn concentrations range from 45 ppm to 4134 ppm (n = 26). Fe concentrations range from 2990 ppm to 8759 ppm (n = 26). Rb concentrations range from 0.0234 ppm to 0.2078 ppm (n = 26). Mn/Sr ratios range up to 2.0678 (n = 26), Fe/Sr ratios range up to 4.8492 (n = 26) and Rb/Sr ratios range up to 9.8×10^{-5} (n = 26). Mn/Sr, Fe/Sr and Rb/Sr ratios are predominantly less than 0.5, 5 and 0.005 respectively (Figure 7 and 8).

4.3.3.2.3 Lower Spitskopf Member

Sr concentrations range from 18 ppm to 3363 ppm (n = 40). Mn concentrations range from 44 ppm to 678 ppm (n = 40) (Figures 7 and 8). Fe concentrations range from 2309 ppm to 5205 ppm (n = 40). Rb concentrations range from 0.1358 ppm to 0.7987 ppm (n = 40). Mn/Sr ratios range up to 13.4556 (n = 40), Fe/Sr ratios range up to 128. 6687 (n = 40) and Rb/Sr ratios range up to 0.0113 (n = 40). Mn/Sr, Fe/Sr and Rb/Sr ratios are predominantly less than 0.5, 5 and 0.005 respectively.

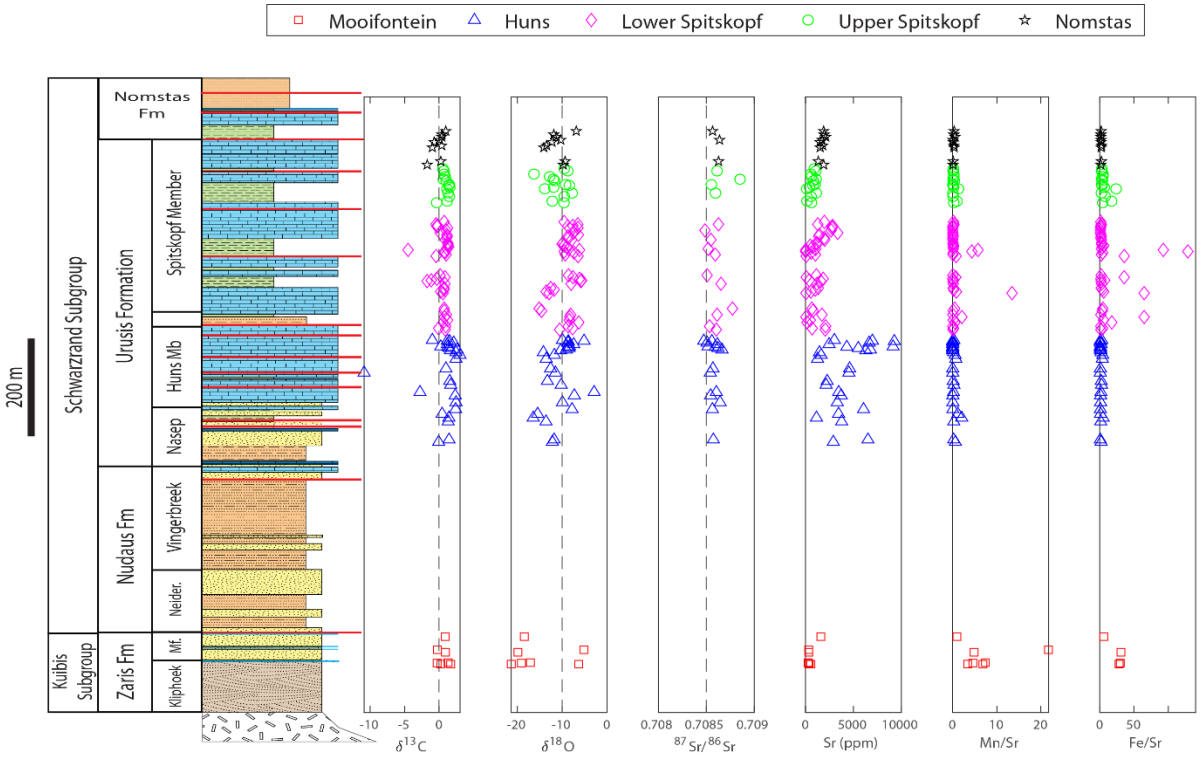

Figure 8: Composite trace elements plots for Huns and Spitskopf members and Nomstas Formation.

4.3.3.2.4 Upper Spitskopf Member

Sr concentrations range from 131 ppm to 1120 ppm (n = 14). Mn concentrations range from 52 ppm to 315 ppm (n = 14). Fe concentrations range from 2630 ppm to 4587 ppm (n = 14). Rb concentrations range from 0.1782 ppm to 0.4665 ppm (n = 14). Mn/Sr ratios range up to 1.3156 (n = 14), Fe/Sr ratios range up to 23.9152 (n = 14) and Rb/Sr ratios range up to 0.0020 (n = 14). Mn/Sr, Fe/Sr and Rb/Sr ratios are predominantly less than 0.5, 5 and 0.005 respectively.

4.3.3.2.5 Nomstas Formation

Sr concentrations range from 1332 ppm to 2111 ppm (n = 9). Mn concentrations range from 130 ppm to 1102 ppm (n = 9). Fe concentrations range from 2914 ppm to 4566 ppm (n = 9). Rb concentrations range from 0.1613 ppm to 0.4809 ppm (n = 9). Mn/Sr ratios range up to 0.5220 (n = 9), Fe/Sr ratios range up to 2.5340 (n = 9) and Rb/Sr ratios range up to 0.0002 (n = 9). Mn/Sr, Fe/Sr and Rb/Sr ratios are predominantly less than 0.5, 5 and 0.005 respectively (Figures 7 and 8).

4.4 Interpretation for trace and rare earth elements data for Neint Nababeep Plateau

4.4.1 Trace element data

The mean Sr content in the Mooifontein Member is the lowest for Neint Nababeep Plateau. Conversely, the Mooifontein Member has the highest mean Mn, Fe and Rb content. Due to the sparse nature of carbonates in this member, the data points are dispersed and stratigraphic trends cannot be deciphered. However, point-by-point comparison shows that Sr content negatively covaries with Mn, Fe and Rb content (Figure 7). Higher Mn and Fe content can be indicative of diagenetic alteration or reducing conditions. Moreover, high Rb contents suggest elevated levels of silicate phases, since Rb preferentially accumulates in clay minerals over carbonate minerals due to its large ionic radii. The Mooifontein carbonates are subordinate to siliciclastic rocks and these could have been the source of clay mineral contamination. The evidence therefore suggests that the high concentrations of Mn and Fe are a consequence of diagenetic alteration by fluids which had previously interacted with silicate rocks. Due to the high Mn/Sr and Fe/Sr of the Neint Nababeep Plateau Mooifontein Member, the samples were not analysed for $^{87}Sr/^{86}Sr$ ratios.

The Schwarzrand Subgroup rocks (Huns and Spitskopf members, Nomstas Formation) are diagenetically well-preserved as evidenced by the low Mn/Sr and Fe/Sr ratios for most of the samples (Figure 8). Sr concentrations are very high, higher than those from Namibian Nama, with the highest values being recorded in the Huns Member. The reason for the high Sr concentrations at Neint Nababeep Plateau could be due to localized high precipitation rate of carbonates or possibly are a result of reduced diagenetic alteration compared to Namibian Nama Group.

4.4.2 REE patterns

All carbonates show enrichment in HREE, consistent with seawater trends (Figure 9). The REE trends therefore provide evidence that these carbonate rocks were deposited in an open marine setting. There are strong positive Eu anomalies in some of the samples from the Mooifontein and Nomstas and these could be due to circulation of hydrothermal fluids in the rocks. These fluids might be associated with the ash layers which are present in these sections. Perhaps surprisingly, ash layers are ubiquitous in the Huns but the samples do not show Eu enrichment. An alternative explanation would be that the Eu anomalies were inherited from the source of the weathered detrital material. Eu anomalies are associated with plagioclase rich rocks due to Eu^{2+} substituting for Ca^{2+} in the crystal lattice of the feldspar minerals. This

process occurs under mantle or deep crust conditions and not near the Earth's surface where sedimentary rocks form. This would suggest that deeply buried rocks were exhumed due to erosion and were the predominant source of weathering during deposition of these rocks. The occurrence of Eu anomalies in rocks that were deposited at different times may signify episodic exposure of the source rocks.

Mooifontein carbonates in the Kuibis Subgroup are depleted in Lanthanum (La). The lack of La enrichment in Mooifontein carbonates makes it difficult to verify whether the REE patterns record seawater. Further to this, the REE content of the Mooifontein samples is significantly higher than the rest. This is highly likely caused by interaction with REE enriched fluids during or post-diagenesis, consistent with altered $\delta^{18}O$ values as well as field and thin section observations.

Ce anomalies change on a metre scale across the water column (Tostevin, Wood, et al., 2016a) and thus provide evidence of localized oxic environments in the depositional environments of these carbonate rocks. Across the Neint Nababeep Plateau section, there are no large Ce anomalies which is consistent with the general REE pattern for the rest of the Nama Group (Tostevin, Shields, et al., 2016b).

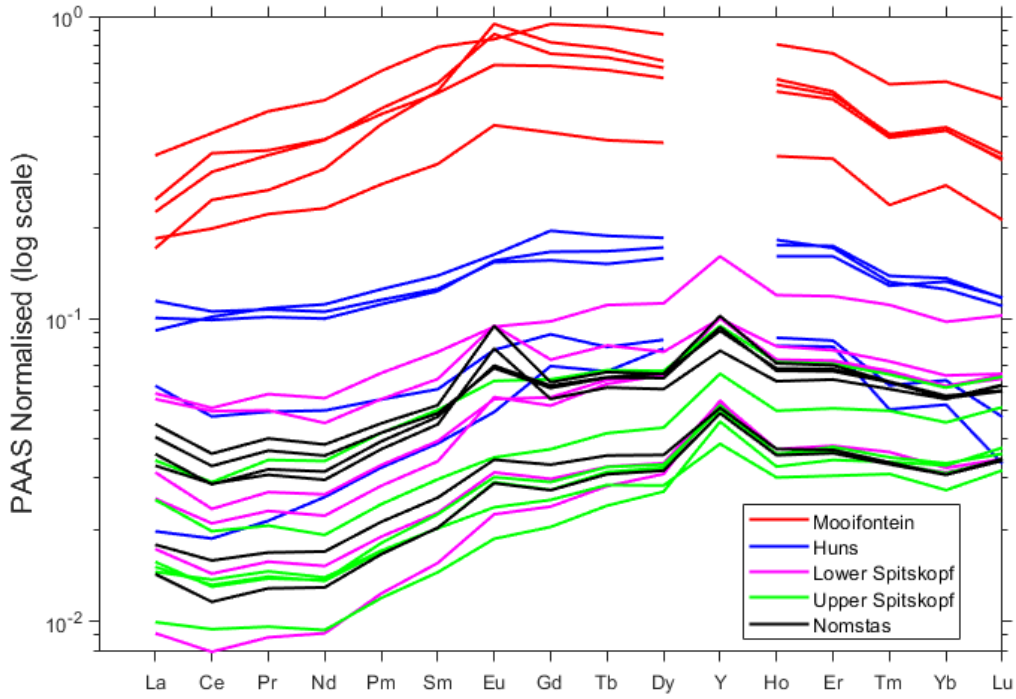

Figure 9: REE patterns of the Mooifontein, Huns, Lower and Upper Spitskopf members and Nomstas Formation.

5 Chapter 5: Strontium isotopes analytical protocol testing

5.1 Introduction

When analysing $^{87}Sr/^{86}Sr$ ratios for strontium isotope stratigraphy (SIS), it is important to select samples that preserve primary seawater signals. Given that $^{87}Sr/^{86}Sr$ analysis is time consuming and expensive, pre-screening of samples is often employed based on petrography and other isotopic and trace element data, to identify the most promising candidates. $\delta^{18}O$ data are susceptible to alteration and carbonates with $\delta^{18}O$ <-10‰ are considered to have been altered significantly (Kaufman et al., 1993; Kuznetsov et al., 2018). High Sr concentration in carbonate phases nullifies the effect of radiogenic ingrowth of ^{87}Sr due to ^{87}Rb decay. Therefore, samples with relatively high Sr concentrations are preferrable for measuring $^{87}Sr/^{86}Sr$ (Derry et al., 1989; Halverson et al., 2007). High Mn content may also indicate diagenetic alteration and higher Mn/Sr is often associated with positive shifts in $^{87}Sr/^{86}Sr$ such that samples with Mn/Sr > 2 are more likely to yield altered $^{87}Sr/^{86}Sr$ ratios (Derry et al., 1992; Kuznetsov et al., 2018). Therefore, a combination of $\delta^{18}O$, Sr content and Mn/Sr ratios could potentially be used to pre-screen samples before Sr isotope analysis.

Where a carbonate sample does not yield primary $^{87}Sr/^{86}Sr$ ratios, this may be because the carbonate phase has been diagenetically altered away from seawater. However, in some cases, poor data quality may be a result of digestion of non-target phases within a complex bulk rock. Digestion of small amounts of phosphate, oxide or clay minerals could skew the weighted average $^{87}Sr/^{86}Sr$ ratio away from the carbonate signal (Bailey et al., 2000). Single step dissolution of carbonate samples usually incorporates Sr from these non-target phases and invariably affects $^{87}Sr/^{86}Sr$ ratios, regardless of the strength of acid used for dissolution (Kaufman et al., 1993, McArthur et al., 1994, Bailey et al., 2000; Li et al., 2011). Sequential digestion of powdered samples using weak acid (e.g., acetic acid) can eliminate contaminant Sr and ensures measurement of $^{87}Sr/^{86}Sr$ ratios from carbonate phases (Bailey et al., 2000; Bellefroid et al., 2018; Li et al., 2011). A sequential leaching protocol is therefore commonly, although not universally, used for sample preparation before analysis of strontium isotopes.

The work of Bailey et al., (2000) is robust and has stood for two decades, but it was only based on four samples, none of which were Precambrian carbonates. Bellefroid et al., (2018) tested 43 Precambrian samples by mechanical removal of visibly altered regions followed by microdrilling before employing a 7-step leaching method (see Bellefroid et al., 2018 for full

description of method). The Bellefroid et al., study was successful in demonstrating the utility of sequential leaching in (1) identifying fractions least contaminated by Sr derived from aluminosilicates and, (2) showing the direction of $^{87}Sr/^{86}Sr$ ratios shifts. It was thus decided to expand the protocol to a new set of Precambrian samples by analysing bulk rock powders. To test the efficacy of the protocol, three samples were chosen and assigned labels 'good', 'moderate' or 'bad' based on their trace element and $\delta^{18}O$ compositions. These samples are all from a short time span and it is anticipated that they all precipitated in an ocean with the same $^{87}Sr/^{86}Sr$ ratio. A sequential digestion procedure was then used to test whether 1) these pre-screening techniques could accurately predict which samples would yield the most primary $^{87}Sr/^{86}Sr$ ratios, and 2) test whether sequential digestion is an effective technique to avoid contamination in Precambrian bulk rock limestones.

5.2 Methods

The samples in this study are all from the Schwarzrand subgroup, Nama Group, and were collected as part of a stratigraphic transect at Neint Nababeep. Three samples were chosen and classified as "bad", "moderate" or "good", primarily based on $\delta^{18}O$ and [Sr] due to the fact that all samples generally had very low Fe/Sr and Mn/Sr ratios (Table 1). Samples obtained in this study generally have high Sr concentrations. Therefore, samples with less than 700 ppm Sr concentration were classified as 'low Sr samples', but it is acknowledged that this cut-off is arbitrary. To ensure that Sr could be detected across all the sequential digestion steps while using the minimum sample mass, 500 ppm was considered the minimum Sr content for samples to be conducive for analysis. The samples were all collected within well constrained stratigraphic transects and span a total distance of ~1300 meters, which represents a timeframe of ~2 Myrs (Nelson et al., 2022).

Approximately 10 mg of powder was treated with sufficient 0.01 M acetic acid to react with 1 mg of the powder and the mixture was agitated and left to stand for >30 minutes. The solution was then centrifuged for 10 minutes at 4000 rpm. The supernatant was removed and stored in a clean tube for analysis. The remaining solid and solution phases were dried down and the entire process was repeated nine more times until all the carbonate phase had been digested. The remnant solid was treated with Aqua regia and the mixture was left to stand for >24 hours. The solution was centrifuged for 10 minutes at 4000 rpm and the supernatant was removed. Elemental Sr separation and purification was carried out after (Pin et al., 2014;

see also for full details of procedure). Sr isotope compositions were measured with a Nu Instrument NuPlasma HR MC-ICP-MS at the University of Cape Town. Sr was analysed as a solution of 200 ppb 0.2% HNO_3 and the reference standard was NIST SRM987 using an $^{87}Sr/^{86}Sr$ ratio normalizing value of 0.710255. An hourly, 30 s on-peak background measurement was carried out in the running acid solution, with a composition of sixty 10 s integrations for each analysis (Howarth et al., 2019). $^{87}Sr/^{86}Sr$ isotope data were corrected for: (i) instrumental mass fractionation using the exponential law and the non-radiogenic $^{86}Sr/^{88}Sr$ ratio with a value of 0.1194 (Nier, 1938), (ii) Rb interference using the natural $^{85}Rb/^{87}Rb$ ratio and the measured signal for ^{85}Rb.

Table 1: Data used to assign three samples as bad, moderate or good, with respect to their predicted preservation potential for $^{87}Sr/^{86}Sr$.

Sample ID	$\delta^{18}O$	Sr (ppm)	Fe/Sr (mass ratio)	Mn/Sr (mass ratio)	Assignment
ORLS-10	-15.15‰,	669	4.48	0.50	Bad
ORLS-19	-8.01‰,	1199	2.64	0.13	Moderate
ORSN-17	-6.87‰,	1891	2.13	0.35	Good

5.3 Results and interpretation

$^{87}Sr/^{86}Sr$ ratios for the carbonate phases in the bad sample (ORLS-10) range from 0.708755 to 0.708892 (n = 10, mean = 0.708788, median = 0.708776, standard deviation = 0.000041) and the contaminant phase yielded a ratio of 0.708879. $^{87}Sr/^{86}Sr$ for the carbonate phase of the moderate sample (ORLS-19) range from 0.708571 to 0.708672 (n = 10, mean = 0.708647, median = 0.708655, standard deviation = 0.000030) and the contaminant phase yielded an $^{87}Sr/^{86}Sr$ ratio of 0.710680 (Table 2). $^{87}Sr/^{86}Sr$ ratios for the carbonate phase of the good sample (ORSN-17) range from 0.708547 to 0.708624 (n = 10, mean = 0.708570, median = 0.708567, standard deviation =0.000023) and the contaminant phase yielded an $^{87}Sr/^{86}Sr$ ratio of 0.709265 (Figure 10A).

Table 2: $^{87}Sr/^{86}Sr$ ratios for sequential leaching protocol

Digestion step	Bad (ORLS10)		Moderate (ORLS19)		Good (ORSN17)	
	$^{87}Sr/^{86}Sr$	±2σ	$^{87}Sr/^{86}Sr$	±2σ	$^{87}Sr/^{86}Sr$	±2σ
1	0.708825	0.000022	0.708655	0.000012	0.708573	0.000013
2	0.708778	0.000012	0.708634	0.000012	0.708570	0.000013
3	0.708774	0.000015	0.708655	0.000018	0.708563	0.000013
4	0.708760	0.000012	0.708655	0.000017	0.708575	0.000024
5	0.708788	0.000013	0.708646	0.000012	0.708547	0.000011
6	0.708762	0.000014	0.708671	0.000012	0.708584	0.000011
7	0.708781	0.000015	0.708641	0.000014	0.708557	0.000013
8	0.708755	0.000048	0.708669	0.000011	0.708550	0.000011
9	0.708768	0.000056	0.708672	0.000016	0.708552	0.000044
10	0.708892	0.000093	0.708571	0.000072	0.708624	0.000072
Aqua regia	0.708879	0.000016	0.710680	0.000062	0.709265	0.000047

For the 'good' and 'moderate' samples, the final contaminant digest, using aqua regia to attack silicates, oxides and organic matter, showed significantly higher $^{87}Sr/^{86}Sr$ values than the weak acid digests, designed to attack carbonate phases (Figure 10A and Table 2). The last carbonate digest of the 'bad' sample had a higher value than the final contaminant digest and this was likely caused by contamination from a silicate phase. Overall, the protocol test confirms a widely held assumption, and the previous work of Bailey et al., (2000), that contamination from non-target phases increases the $^{87}Sr/^{86}Sr$ ratio. This is why it is common practice in strontium isotopes stratigraphy (SIS) studies to select the lowest $^{87}Sr/^{86}Sr$ ratios from a stratigraphic succession on the assumption that they are the closest representation of seawater. The sequential leaching protocol is thus designed to minimize the risk of contributions from non-carbonate phases (Bailey et al., 2000; Li et al., 2011; Bellefroid et al., 2018). This study has repeated the work of Bailey et al., (2000) to confirm their protocol, and also extended it to a wider range of sample types. The samples employed in the Bailey et al., (2000) (two chalks, a marl and an indurated limestone) were all fossil bearing, Phanerozoic aged and had variable cementation and hardness. Samples from this study were all Precambrian, non-fossil bearing, lithified and hard limestones and represent mostly different marine conditions to those prevalent in the Phanerozoic.

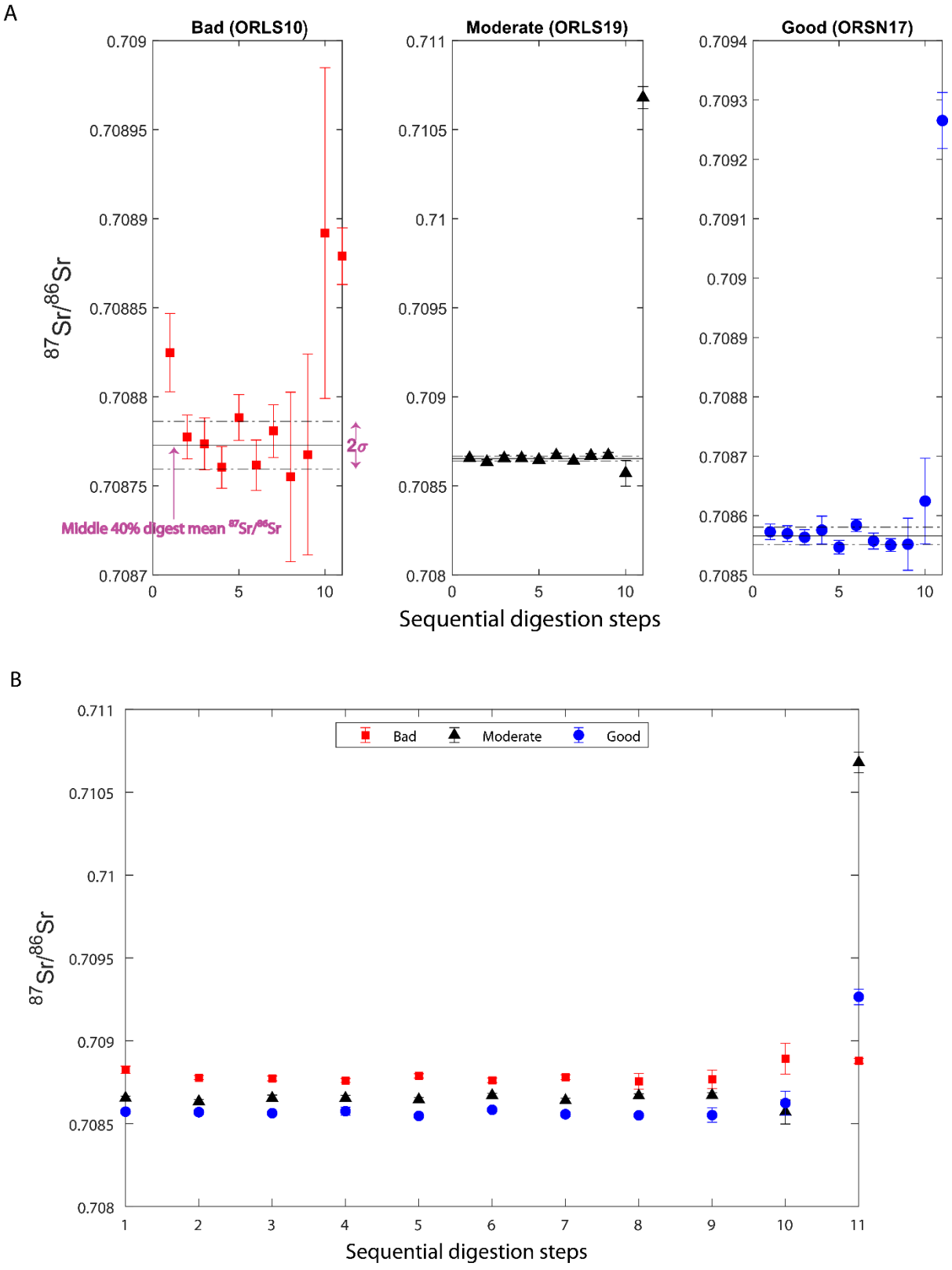

Figure 10: Sequential digestion plots. (A) individual sequential digest plots for the three samples. (B) Comparison of the sequential digestion steps for the three samples.

The ‘good’ sample has the lowest average $^{87}Sr/^{86}Sr$ ratio across the carbonate digests, and the lowest standard deviation. There is a clear difference between the carbonate digests and the final contaminant digest. In contrast, the ‘bad’ sample shows a higher average $^{87}Sr/^{86}Sr$ ratio, and the most variation across the digests, with a clear trend towards higher $^{87}Sr/^{86}Sr$ ratios in later digests. The final carbonate leach had a high $^{87}Sr/^{86}Sr$ ratio similar to the contaminant leach, indicating contamination through silicate leaching. The bad sample also had significantly large analytical errors, especially for the 80% to 100% carbonate leaches (Figure 10A).

The assignment of sample quality in advance, based on $\delta^{18}O$ and Sr content, appears to successfully predict which samples will yield the lowest, least contaminated $^{87}Sr/^{86}Sr$ ratios. This study therefore supports the use of these parameters for crude sample screening prior to SIS work. The high $^{87}Sr/^{86}Sr$ ratio of the first leach (10% carbonate dissolution) of the ‘bad’ sample shows the importance of excluding the first part of the sample during sequential digestion. Single step dissolution would incorporate the Sr from this first leach, which has a higher $^{87}Sr/^{86}Sr$ ratio and likely originates from a non-target phase such as evaporated groundwater salts and also Sr from ion exchange sites, increasing the average $^{87}Sr/^{86}Sr$ of the sample(Bailey et al., 2000). Similarly, single step dissolution would incorporate the final contaminant phases of clays, oxides etc, once all the carbonate phase has been digested, and this would affect the $^{87}Sr/^{86}Sr$ value (Bellefroid et al., 2018; Li et al., 2011). Measuring $^{87}Sr/^{86}Sr$ from the middle 40% digest, as was done in this study, ensured that the contaminant phases which are present in the initial and final digests were avoided. Although in ‘good’ samples, such a method may not be necessary, it can make a big difference in ‘bad’ samples. As such, it is highly recommended to apply the method consistently to all samples, in combination with sample pre-screening, to obtain the best results. This minimizes any risk of contamination in samples that appear ‘good’, but where pre-screening has failed, and may allow uncontaminated data to be safely extracted from ‘moderate’ or even ‘bad’ samples.

6 Chapter 6: Strontium isotopes analysis and strontium isotope stratigraphy

6.1 Introduction

Strontium isotopes ratios ($^{87}Sr/^{86}Sr$) are useful for chemostratigraphy due to the long residence time of Sr, which records global ocean signals which are well-preserved in carbonate rocks (Chen et. al., 2022; Shields & Veizer, 2002). There remains considerable uncertainty around stratigraphic correlations across the Ediacaran-Cambrian boundary. Better constraints are needed to improve our understanding of critical patterns of evolution which emerged during the terminal Ediacaran and early Cambrian.

Strontium isotope stratigraphy (SIS) has previously been used in areas such as South China, Oman, Namibia and Siberia, alongside radiometric dates and C isotopes (see Bowyer et al., 2022 for best current correlations). However, Precambrian chemostratigraphy, which is mostly anchored by C isotopes is inherently problematic due to questions around whether $\delta^{13}C$ signals are global or local. Since it is widely agreed that Sr isotopes trends in marine carbonates preserve global signals, improving SIS can enhance the quality of Precambrian chemostratigraphy. Moreover, SIS is a useful tool in understanding weathering patterns during the Ediacaran which have possible implications for the emergence biomineralizing metazoans.

The Nama Group offers one of the best sections for calibrating fossil records across the Ediacaran–Cambrian Boundary, but unfortunately, existing data are sparse (n = 25) and pre-date existing stratigraphic correlations (Kaufmann et al., 1993). There are also general concerns around diagenesis and scatter in Sr isotope data and there are very few high quality records available for the Ediacaran. Here, new high-resolution data from an expanded section of the Nama Group with high sedimentation rates will be presented along with radiometric dates. The best possible sample screening and laboratory extraction techniques were used in order to maximize chances of obtaining primary signals.

6.2 Sr isotopes analysis

51 Carefully selected samples (33 from Schwarzrand Subgroup – Neint Nababeep Plateau, 18 from Kuibis Subgroup – Zebra River section, Namibia), based on Sr content, Mn/Sr and $\delta^{18}O$, petrographic characteristics as well stratigraphic position, were pre-washed with 1 M ammonium acetate to remove non-target phase Sr (Bailey et al., 2000). The samples were then sequentially leached to target a central digest which constituted 40% of the sample (see

Chapter 5). ~2.5 mg of powder was treated with 0.0075 M acetic acid to dissolve 0.75 mg (initial 30% of sample). The mixture was left to stand for >30 minutes after which it was centrifuged at 4000 rpm for 10 minutes and the supernatant was decanted and discarded. After drying down, the remaining sample was reacted with 0.01 M acetic acid to dissolve 1 mg (middle 40% of the sample) and the mixture was agitated and left to stand for >30 minutes. The mixture was centrifuged at 4000 rpm for 10 minutes and the supernatant was pipetted out and analysed for Sr isotope composition. The remaining undigested sample was discarded. Strontium isotope analysis was carried out in the same manner as in Chapter 5.

6.3 Results

6.3.1 Sr isotopes

$^{87}Sr/^{86}Sr$ ratios in the Omkyk and Hoogland members (Kuibis Subgroup – Zebra River, Namibia) range from 0.708678 to 0.711602 (n = 18) (Table 3). In the Huns Member (Neint Nababeep Plateau, South Africa) Sr isotope ratios range from 0.708474 to 0.709001 (n = 16). One value is anomalously high (ORH26 = 0.709001). In the Lower Spitskopf $^{87}Sr/^{86}Sr$ ratios range from 0.708487 to 0.708773 (n = 11). $^{87}Sr/^{86}Sr$ in the Upper Spitskopf range from 0.708553 to 0.708852 (n = 4) and in the Nomstas $^{87}Sr/^{86}Sr$ range from 0.708566 to 0.708638 (n = 3). The data are all displayed in Table 3.

6.3.2 Strontium isotopes interpretation

6.3.2.1 Schwarzrand Subgroup (Neint Nababeep, South Africa)

$^{87}Sr/^{86}Sr$ data from Neint Nababeep (Table 3) are remarkably consistent throughout the stratigraphy and are similar to the previously reported value of 0.7085 for Nama Group carbonates (Kaufmann et al., 1993). The two outlying data points ($^{87}Sr/^{86}Sr > 0.7087$) are for the “bad” sample and sample ORSN02 which was selected for stratigraphic coverage but whose trace element data suggested relatively high degree of alteration compared to the rest of the samples. Together, this further validates the pre-screening process which selected the least altered samples for strontium isotope analysis (see Chapter 5).

Diagenetic screening using trace elements and $\delta^{18}O$ indicates that the samples have been well preserved and have not been severely affected by late-stage diagenesis or alteration. A comparison of $^{87}Sr/^{86}Sr$ with Sr content does not show any trend (positive or negative) with $^{87}Sr/^{86}Sr$ ratios mostly oscillating between 0.7085 and 0.7086 for Sr concentrations range of 1000 ppm to 10000 ppm.

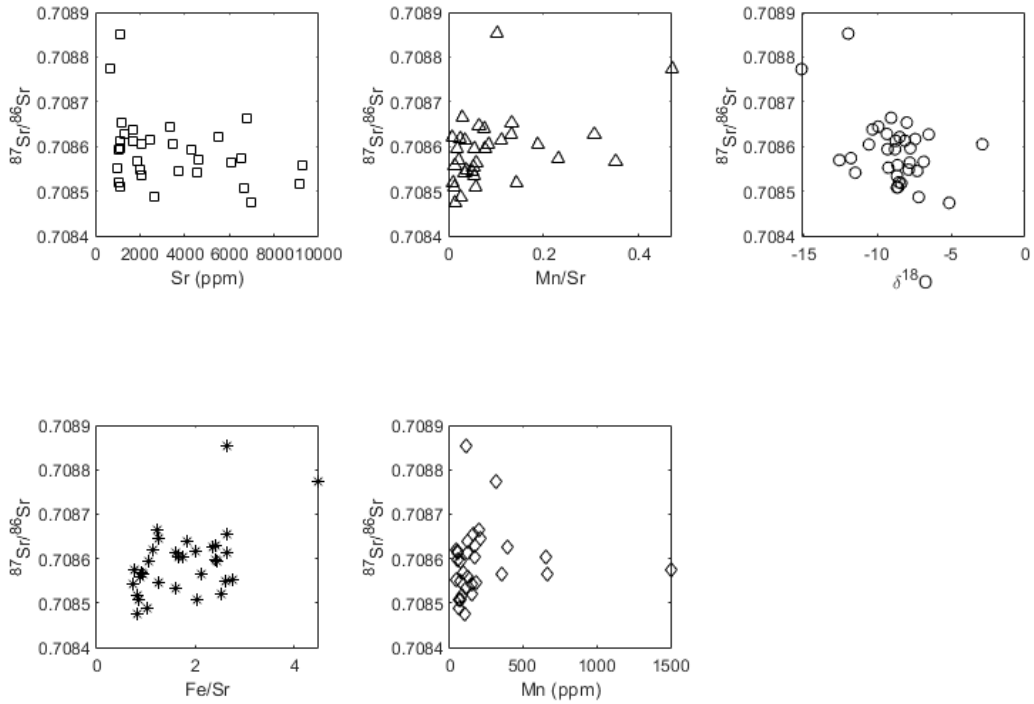

Figure 11: Cross-plots of $^{87}Sr/^{86}Sr$ against trace elements which are useful geochemical parameters for diagenetic screening. Data are from Schwarzrand Subgroup, South Africa.

Similarly, respective comparisons of $^{87}Sr/^{86}Sr$ ratios with Mn/Sr, Fe/Sr ratios do not show variation of $^{87}Sr/^{86}Sr$ with increasing Mn/Sr, Fe/Sr or $\delta^{18}O$ (Figure 11). A comparison with Mn content shows a slight positive correlation. Since Mn is known to increase during diagenetic alteration caused by meteoric fluids during early-stage diagenesis, the covariation between $^{87}Sr/^{86}Sr$ and Mn suggests that the rocks experienced some degree of alteration, and that the lowest $^{87}Sr/^{86}Sr$ ratios are closest to primary seawater.

6.3.2.2 Kuibis Subgroup (Zaris Basin, Namibia)

Kuibis Subgroup $^{87}Sr/^{86}Sr$ ratios are variable and have likely experienced some degree of diagenetic alteration. Higher $^{87}Sr/^{86}Sr$ ratios are associated with lower Sr contents (Figure 12). Similarly, higher $^{87}Sr/^{86}Sr$ are associated with high Fe/Sr and Mn/Sr ratios, with the strongest correlation observed with Fe/Sr. There is no correlation between $\delta^{18}O$ and $^{87}Sr/^{86}Sr$ ratios or Mn content.

The extent of alteration makes it difficult to ascertain the initial seawater $^{87}Sr/^{86}Sr$ however, two things have been observed: 1) Kuibis Subgroup $^{87}Sr/^{86}Sr$ are all higher than 0.7085; 2) the least altered samples mostly yield ratios around 0.7090. Due to the clear diagenetic trends

which have affected $^{87}Sr/^{86}Sr$ ratios, the very high ratios from the Zaris Section mostly likely do not represent primary seawater.

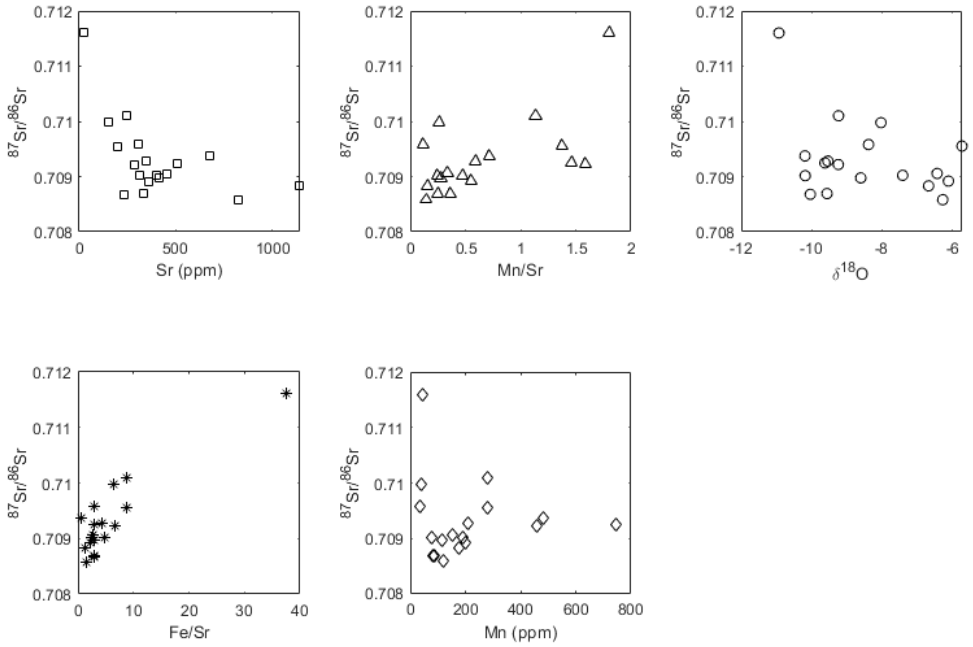

Figure 12: Cross-plots of $^{87}Sr/^{86}Sr$ against trace elements which are useful geochemical parameters for diagenetic screening. Data are from Kuibis Subgroup, Namibia.

6.3.3 Water-rock interaction modelling

Models of co-variation between Sr content and $^{87}Sr/^{86}Sr$ ratios provide important information on water-rock interaction (Banner & Hanson, 1990) (Figure 13). In the Banner & Hanson (1990) model, two limestones with the same $^{87}Sr/^{86}Sr$ ratio (0.7080) but different Sr concentrations (1000 and 200 ppm), were allowed to separately interact with a fluid. The fluid had a Sr content of 10 ppm Sr and an $^{87}Sr/^{86}Sr$ ratio of 0.7200, which closely approximates riverine input of some modern rivers e.g., Ganges River (Richter et al., 1992). The two limestones both attained the equilibrium Sr value of 200 ppm at the same cumulative fluid:rock ratio, whereas the limestone with lower Sr content attained $^{87}Sr/^{86}Sr$ equilibrium with the fluid at a lower fluid:rock ratio than the limestone with higher Sr content. The difference is caused by different controlling factors: Sr content is controlled by K_D^{Sr-Ca} and concentration of calcium in the fluid while $^{87}Sr/^{86}Sr$ is dependent on the Sr content of the limestones (Banner & Hanson, 1990).

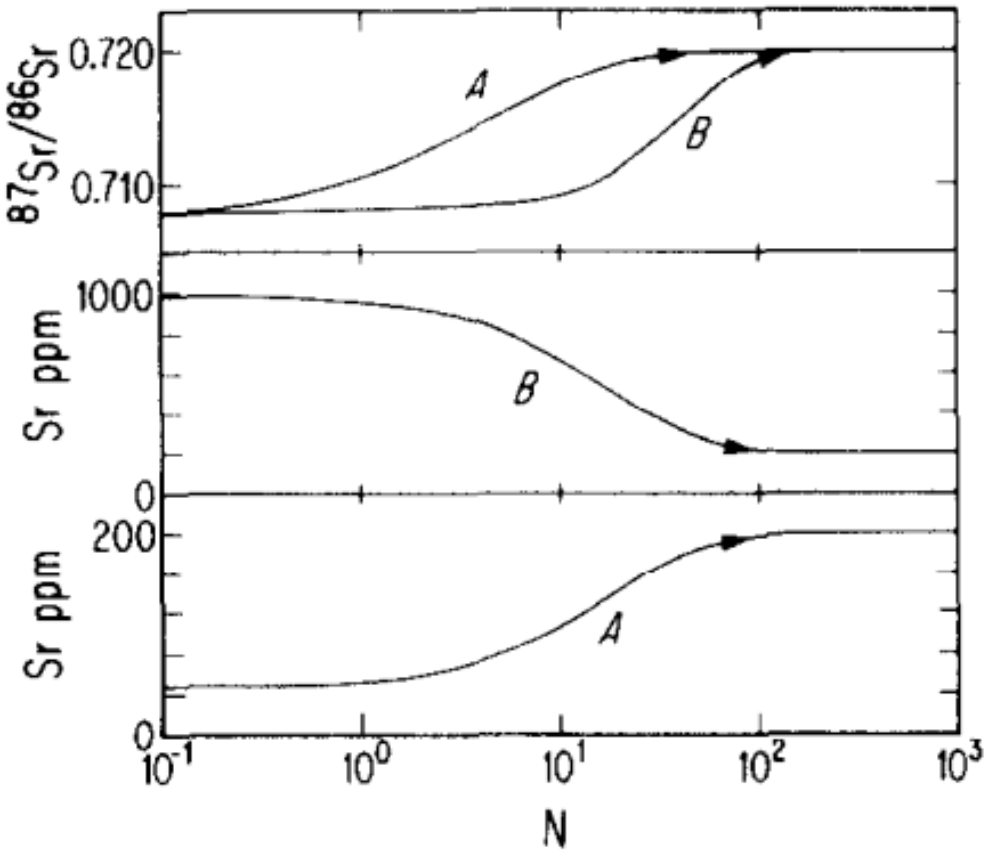

Figure 13: Numerical modelling of variation of $^{87}Sr/^{86}Sr$ and Sr concentration with increasing N (cumulative fluid:rock ratio) for recrystallisation of limestone A (20 ppm Sr) and limestone B (1000 ppm Sr). Both rocks have initial porosity of 50% and $^{87}Sr/^{86}Sr$ value of 0.7080. The curves show the pathway of compositional change of the two rocks as they interact with a fluid of 10 ppm Sr, 1000 ppm Ca and $^{87}Sr/^{86}Sr$ value of 0.7200 and $K_D^{Sr-Ca} = 0.05$. Arrows show direction of progressive fluid-rock interaction and position of the arrows signifies fluid:rock ratio at which Sr concentration or $^{87}Sr/^{86}Sr$ has reached 99% of the equilibrium value. Taken from Banner and Hanson, (1990).

We can use this model to approximate the fluid:rock ratios at which the Sr isotopic shifts observed in this study occurred (Veizer, 1983). Two samples, assumed to represent the most altered sample from the Schwarzrand and Kuibis subgroups respectively will be profiled. Sample ORSN02 from the Upper Spitskopf, Schwarzrand Subgroup, has an $^{87}Sr/^{86}Sr$ ratio of 0.708852 and Sr content of 1113 ppm. Assuming the rock had an initial $^{87}Sr/^{86}Sr$ of 0.7085, and came into contact with fluids with a composition similar to riverine input, a cumulative fluid:rock ratio of at least 10 would be required to produce the 35 x 10^{-5} positive $^{87}Sr/^{86}Sr$ shift. In contrast, sample LO-2 from the Kuibis Subgroup, with Sr content of 24 ppm and $^{87}Sr/^{86}Sr$ ratio of 0.711602 would only have required a fluid:rock ratio of ~1 to produce the 26 x 10^{-4} positive $^{87}Sr/^{86}Sr$ shift. This highlights that the principal control on shifts in Sr isotopic composition during alteration is the initial Sr content of the sample.

The model also helps constrain the extent of $^{87}Sr/^{86}Sr$ alteration during diagenesis. The high Sr carbonates of the Schwarzrand Subgroup would have required water dominated conditions (open system) to be extremely affected by diagenetic alteration. For such shallow environment carbonates, these conditions could have only been attained during early deposition and recrystallisation of the carbonates. Post burial, the cumulative fluid:rock ratio would have drastically reduced such that the impact of diagenetic alteration was effectively buffered by the high Sr concentration of the sediments and as such the shift in $^{87}Sr/^{86}Sr$ ratios would not have been pronounced. Further diagenesis likely proceeded under rock dominated conditions (closed system) and as such cements precipitated from pore fluids would have inherited the $^{87}Sr/^{86}Sr$ of the primary minerals (Marshall, 1992). This strongly implies that the rocks predominantly preserve signals of early-stage diagenetic cements which would have precipitated in near equilibrium with seawater.

For the Kuibis Subgroup carbonates from the Zaris sub-basin, which generally have lower Sr content than the Neint Nababeep Plateau samples, low fluid:rock ratios would have been adequate to induce significant isotopic shifts. Such low ratios can persist post burial, as long as diagenetic potential of the rocks exists. As such, diagenetic alteration would have been prolonged hence the large observed $^{87}Sr/^{86}Sr$ shifts in these rocks.

6.3.4 Rb correction

Radioactive decay of ^{87}Rb to ^{87}Sr may affect $^{87}Sr/^{86}Sr$ ratios of carbonates if substantial Rb was incorporated into the crystal lattice of the carbonate minerals. The effect may be severe enough to obscure original global ocean Sr isotope signals in marine carbonates over a given geological time. To account for the resultant additional ^{87}Sr, a Rb correction was made using the formula:

$$Rb_{corr} = {}^{87}Rb/{}^{86}Sr\,(e^{\lambda t} - 1) \qquad \text{Equation 3}$$

$$^{87}Rb/^{86}Sr = \left((Rb_{meas}/Rb_W)^{87}Rb_F\right)/\left((Sr_{meas}/Sr_W)^{86}Sr_F\right) \cong 2.893(Rb_{meas}/Sr_{meas})$$

λ is the decay constant, t is the geological time which has elapsed since deposition of the carbonate, Rb_{meas} and Sr_{meas} are the measured concentrations of Rb and Sr in ppm, Rb_W and Sr_W refer to the atomic weights of Rb and Sr and $^{87}Rb_F$ and $^{86}Sr_F$ are the respective atomic fractions related to the abundances of ^{87}Rb and ^{86}Sr isotopes.

Then,

$$^{87}Sr/^{86}Sr_{corr} = {}^{87}Sr/^{86}Sr_{meas} - Rb_{corr}$$

The corrected $^{87}Sr/^{86}Sr$ values are marginally shifted downwards compared to the measured values (Figure 14) and this is attributed to the high Sr concentrations of the samples which overprint the effect of ^{87}Rb decay. For this reason, measured values from this study should be regarded as being reflective of original global ocean signal at the time of deposition, unless they have been shown to be diagenetically altered as is the case for Kuibis Subgroup samples from Zebra River, Namibia.

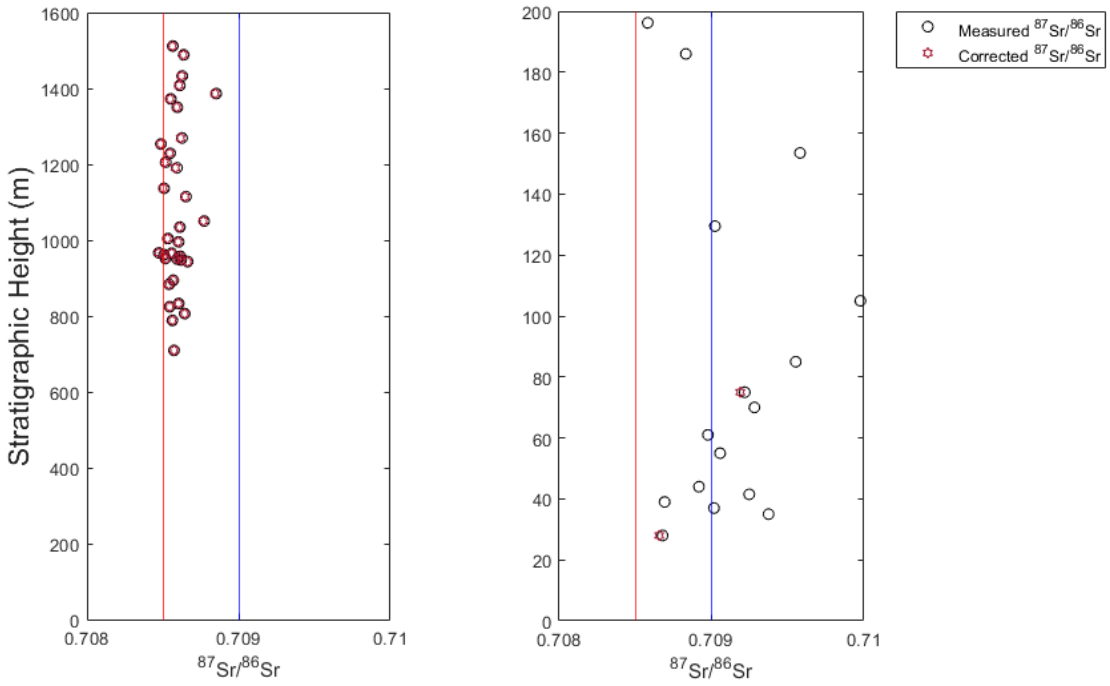

Figure 14: Strontium isotope stratigraphy logs for Schwarzrand Subgroup (left) and Kuibis Subgroup (right). Red line is $^{87}Sr/^{86}Sr$ = 0.7085. Blue line is $^{87}Sr/^{86}Sr$ = 0.7090.

Table 3: Measured and corrected $^{87}Sr/^{86}Sr$ values for Kuibis and Schwarzrand subgroups.

Sample Name	$^{87}Sr/^{86}Sr$ Measured	2σ Error	$^{87}Sr/^{86}Sr$ Corrected*
Kuibis Subgroup – Zebra River, Namibia			
LO-2	0.7116025	0.000028	
LO-6	0.7086780	0.000012	0.7086563
LO-7	0.7093741	0.000022	
LO-8	0.7090158	0.000016	
LO-9	0.7086918	0.000012	
LO-10	0.7092471	0.000015	
LO-11	0.7089172	0.000015	
LO-15	0.7090559	0.000015	
LO-16	0.7089761	0.000015	
OS2-1	0.7101010	0.000025	
OS2-2	0.7092812	0.000013	
OS2-3	0.7092176	0.000021	0.7091886
OS2-4	0.7095524	0.000020	
OS2-6	0.7099766	0.000011	
ZR-12	0.7090223	0.000018	
ZR-19	0.7095805	0.000019	
ZR-34	0.7088311	0.000011	
ZR-36	0.7085805	0.000013	
Schwarzrand Subgroup – Neint Nababeep Plateau, South Africa			
ORH02	0.7085738	0.000011	0.7085735
ORH06	0.7085637	0.000011	0.7085632
ORH07	0.7086442	0.000014	0.7086436
ORH08	0.7085451	0.000016	0.7085447

ORH09	0.7086047	0.000012	0.7086034
ORH12	0.7085412	0.000012	0.7085409
ORH13	0.7085693	0.000009	0.7085691
ORH18	0.7086639	0.000013	0.7086638
ORH19	0.7086209	0.000013	0.7086207
ORH20	0.7085936	0.000011	0.7085933
ORH21	0.7085177	0.000009	0.7085173
ORH22	0.7086164	0.000011	0.7086157
ORH23	0.7085082	0.000010	0.7085080
ORH24	0.7085581	0.000017	0.7085580
ORH25	0.7084737	0.000009	0.7084736
ORLS02	0.7086042	0.000014	0.7086006
ORLS04	0.7085342	0.000014	0.7085309
ORLS08	0.7086126	0.000011	0.7086100
ORLS10	0.7087728	0.000013	0.7087674
ORLS19	0.7086533	0.000014	0.7086464
ORLS24	0.7085084	0.000014	0.7085032
ORLS27	0.7085936	0.000016	0.7085834
ORLS31	0.7085197	0.000016	0.7085129
ORLS36	0.7085480	0.000010	0.7085447
ORLS41	0.7084867	0.000010	0.7084851
ORLS45	0.7086267	0.000016	0.7086179

ORLS55	0.7085959	0.000014	0.7085923
ORLS59	0.7085525	0.000023	0.7085480
ORSN02	0.7088522	0.000010	0.7088448
ORSN05	0.7086126	0.000010	0.7086071
ORSN08	0.7086279	0.000022	0.7086239
ORSN14	0.7086379	0.000017	0.7086354
ORSN17	0.7085658	0.000015	0.7085632

*** Rb content was too low for most samples and as such, no $^{87}Sr/^{86}Sr$ corrections were done for those samples.**

6.3.5 Reliability of $^{87}Sr/^{86}Sr$ ratios obtained in this study

6.3.5.1 Neint Nababeep Plateau, South Africa

The lack of clear covariation between $^{87}Sr/^{86}Sr$ and trace element ratios (i.e., Mn/Sr, Fe/Sr and Rb/Sr) or $\delta^{18}O$ indicates minimal diagenetic alteration. Furthermore, the high Sr concentrations of the samples analysed for $^{87}Sr/^{86}Sr$ combined with the sequential digestion protocol employed in this study lead to the conclusion that the $^{87}Sr/^{86}Sr$ data of the Schwarzrand Subgroup from Neint Nababeep Plateau closely reflect the strontium isotope composition of the seawater from which the carbonates precipitated. $^{87}Sr/^{86}Sr$ ratios from Neint Nababeep Plateau are well constrained by six dated ash beds hosted in the Huns and Spitskopf members and the Nomstas Formation, with the Huns bed yielding the oldest date of 539.63 ± 0.15 Ma and the Nomstas ash bed yielding the youngest date of 537.95 ± 0.28 Ma (Nelson et al., 2022). Hence, the age constraints placed by the absolute dates combined with the consistent $^{87}Sr/^{86}Sr$ ratios (~0.7085) can be interpreted to indicate stable marine $^{87}Sr/^{86}Sr$ during the final ~2 million years of the Ediacaran Period. Therefore, the Sr isotope data obtained from Neint Nababeep Plateau likely represent the best available constraints on the marine $^{87}Sr/^{86}Sr$ ratio in the terminal Ediacaran, especially close to the Ediacaran-Cambrian boundary.

6.3.5.2 Zebra River, Namibia

$^{87}Sr/^{86}Sr$ ratios from the Zebra River section of the Zaris Basin, Namibia have been shown to covary with trace element ratios that are diagnostic of diagenetic alteration (Figure 12).

However, when $^{87}Sr/^{86}Sr$ ratios are plotted alongside stratigraphic plots of $\delta^{18}O$, $\delta^{238}U$ and $\delta^{34}S_{CAS}$, no covariations are observed (Figure 15). The lack of correlation with $\delta^{18}O$ is curious because meteoric fluid, which is the common cause of early-stage diagenetic alteration, typically has much lower $\delta^{18}O$ than seawater. Diagenetic alteration is apparent in samples with a range of $\delta^{18}O$ values (~-10‰ to -5‰), suggesting Sr isotopes were altered via non-meteoric fluid sources. Early-stage diagenesis has also been noted to increase $\delta^{238}U$ and positive offsets of up to 0.3‰ have been reported in modern sediments (Romaniello et al., 2013). As such, positive shifts caused by early-stage diagenetic alteration ought to be observed for both $^{87}Sr/^{86}Sr$ and $\delta^{238}U$.

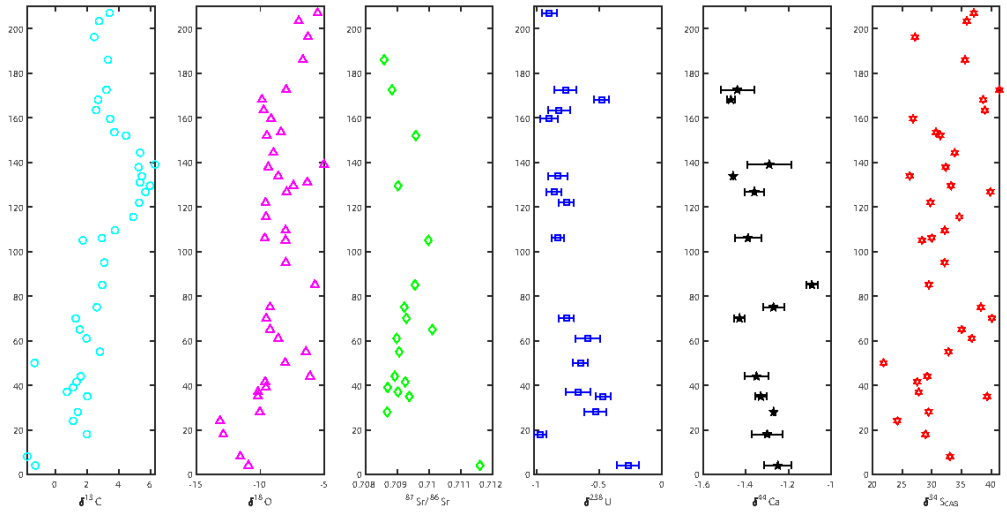

Figure 15: Chemostratigraphy plots of the Zebra River section of the Zaris sub-basin, Namibia. $\delta^{34}S_{CAS}$, $\delta^{13}C$ and $\delta^{18}O$ are from Tostevin et al., (2017). $\delta^{238}U$ and $\delta^{44}Ca$ are from Tostevin et al., (2019a) and Tostevin et al., (2019b). $^{87}Sr/^{86}Sr$ are from this study.

However, $\delta^{238}U$ data from the Zebra River section (Tostevin, et al., 2019b) show fluctuations but these are not reflected in the correlative $^{87}Sr/^{86}Sr$ ratios. Similarly, $\delta^{34}S_{CAS}$ data from the same section (Tostevin et al., 2017) show variations which are not mirrored by the strontium isotope data. For both $\delta^{238}U$ and $\delta^{34}S_{CAS}$, the values and trends have been determined to indicate original seawater isotopic composition and variation across the terminal Ediacaran (Tostevin, et al., 2019b; Tostevin et al., 2017). $^{87}Sr/^{86}Sr$ ratios are highly susceptible to diagenesis compared to other geochemical proxies e.g., $\delta^{238}U$ and the data possibly reflect limited diagenesis which mostly affected $^{87}Sr/^{86}Sr$. There is also lack of discernable stratigraphic trend in $^{87}Sr/^{86}Sr$, again suggesting that variability is due to variable diagenesis.

It is therefore difficult to extract useful information about the primary seawater $^{87}Sr/^{86}Sr$ from the Zebra River samples, but it is concluded that seawater $^{87}Sr/^{86}Sr$ was at least as high, if not higher, than in the Schwarzrand Subgroup.

6.4 Long term evolution of Neoproterozoic seawater

It has been proposed that a prolonged rise in continental weathering rates was the main influence on the long-term increase in $^{87}Sr/^{86}Sr$ ratios across the Neoproterozoic (Shields, 2007). Superimposed on this steady increase are smaller fluctuations, suggesting multiple factors were at play. The Neoproterozoic is notable for: 1) climatic upheavals, the most conspicuous being the two Cryogenian Period global glaciation events, 2) breakup of the supercontinent Rodinia and the assembly of Gondwana, and 3) emplacement of several CFBs (Ernst et al., 2013; McCausland et al., 2011; Merdith et al., 2017; Rooney et al., 2014; Stern, 2018). Several authors have argued that the impact of these events was severe enough to impinge on the base-level, long term $^{87}Sr/^{86}Sr$ changes caused by Rb decay (e.g. Halverson et al., 2007; Cox et al., 2016; Rooney et al., 2014, 2015; Shields & Veizer 2002; Shields 2007).

The low $^{87}Sr/^{86}Sr$ ratios (0.7055 – 0.7060) during the early Neoproterozoic (950 – 850 Ma) (Figure 16A) have been attributed to the tenure of Rodinia which was characterized by low relief and high continentality, resulting in enhanced weathering of volcanic arcs on the margins of the supercontinent (Allégre et al., 2010; Chen et al., 2022). Volcanic arcs are dominated by basalt and andesitic rocks which have low $^{87}Sr/^{86}Sr$ and these rocks would have been juvenile at the time of their emplacement during Rodinia assembly (Allègre et al., 2010). The eruption of the Dashigou CFB and Franklin CFB have been credited with a drop in $^{87}Sr/^{86}Sr$ from 0.7064 to 0.7052 and from 0.7071 to 0.7064 at 920 Ma and 720 Ma respectively (Cox et al., 2016; Zhou et al., 2020). In a clear demonstration of the interplay of tectonics, palaeogeography and atmospheric pCO_2, it has been suggested that the Franklin CFB was situated in the tropics where high surface temperatures and rainfall would have increased draw down of atmospheric CO_2 and increased weathering of the CFB (Cox et al., 2016). The rapid chemical weathering of the Franklin CFB has thus been postulated to have caused the Sturtian Snowball glaciation due to the associated rapid drop in atmospheric pCO_2 (Rooney et al., 2015; Cox et al., 2016). The commencement of the assembly of Gondwana ca. 600 Ma saw a steep rise in $^{87}Sr/^{86}Sr$ and this has been attributed to an increase in weathering caused by

collision induced uplift and the rise was sustained until ~ca 550 Ma when the values peaked at ~0.7090 (Chen et al., 2022; Zhou et al., 2020).

6.5 Correlating Nama Group strontium isotope data to global Ediacaran strata

The data obtained in this study are from ca. 550 Ma to 538 Ma, a span of time generally accepted to have high $^{87}Sr/^{86}Sr$ ratios. Thus, it is imperative that the data are placed within a broader Ediacaran framework. In order to achieve this, the data from this study will be compared with correlative Ediacaran strata from Namibia, Oman and South China.

6.5.1 Namibia

The Zaris and Witputs basins in Namibia have been extensively studied and represent the benchmark for correlating the Neint Nababeep Plateau strata. The presence of ash beds within the strata of Zaris and Witputs basins constrain the age of deposition to between <550 Ma and ~538 Ma, based on the 547.36 ± 0.36 Ma from (Bowring et al., 2007) and a younger date of 538.58 ± 0.19 Ma from an ash bed located in the Nomstas Formation (Linnemann et al., 2019). Further, ash beds situated in the intervening members help to anchor the deposition dates of the respective members. Carbon isotope chemostratigraphy correlation shows that the older Omkyk and Hoogland members of Zaris sub-basin and the Mara Member of the Witputs sub-basin are missing from the Neint Nababeep Plateau section. However, the Schwarzrand Subgroup strata are better preserved at Neint Nababeep Plateau than the correlative Namibian sub-basins.

Previously published $^{87}Sr/^{86}Sr$ ratios data show scatter in the Zaris Formation (Kuibis Subgroup, Lower Nama) but a minimum value of 0.708398 was obtained from a non-luminescent microspar which was isolated from bulk rock and represents early forming cement (Kaufman et al., 1993). The solitary minimum value can thus be considered to be representative of seawater $^{87}Sr/^{86}Sr$ during the precipitation of the upper Kuibis Subgroup (Omkyk and Hoogland members). $^{87}Sr/^{86}Sr$ obtained from the Urusis Formation (Schwarzrand Subgroup, Upper Nama) show less scatter than the Lower Nama samples and converge around 0.7085, similar to those measured from Neint Nababeep Plateau (Kaufman et al., 1993). Considering the age gap between deposition of the lower Nama carbonates and deposition of the Upper Nama carbonates, ~5 million years (conservative estimate), the 0.0001 increase is likely indicative of an aging continental crust (i.e., higher $^{87}Sr/^{86}Sr$ caused by Rb decay) and not a change in weathering rates.

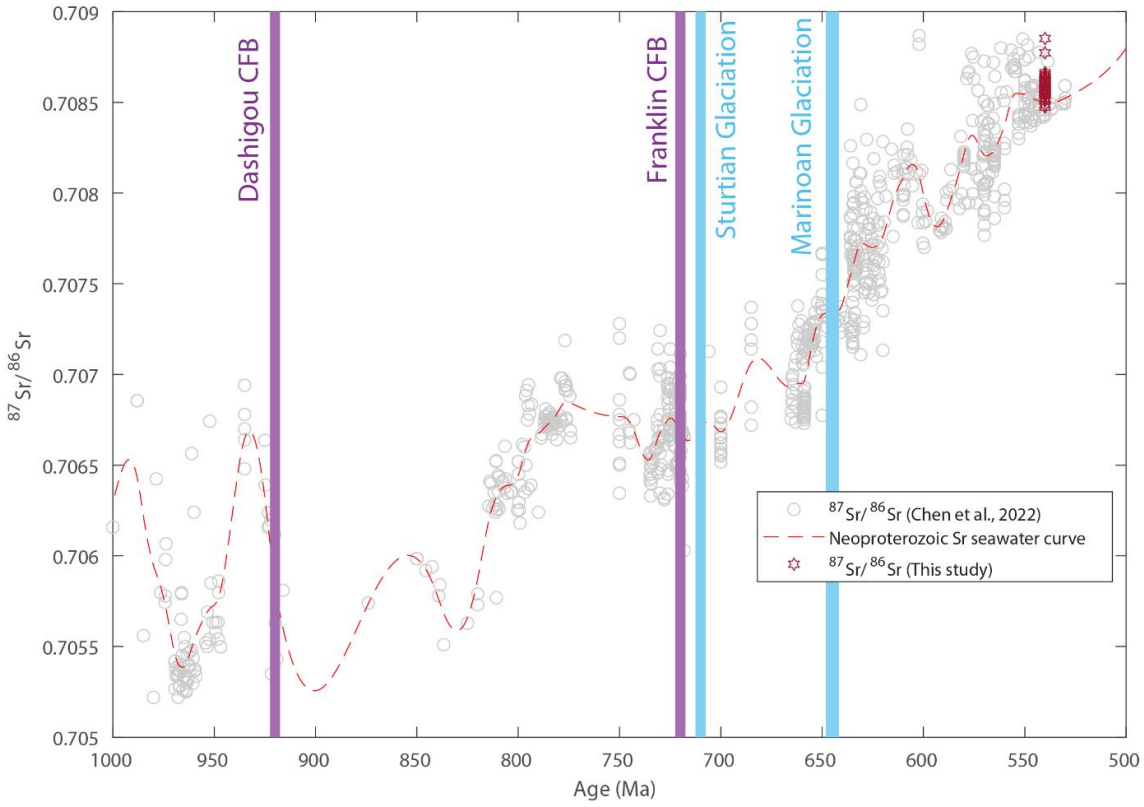

B

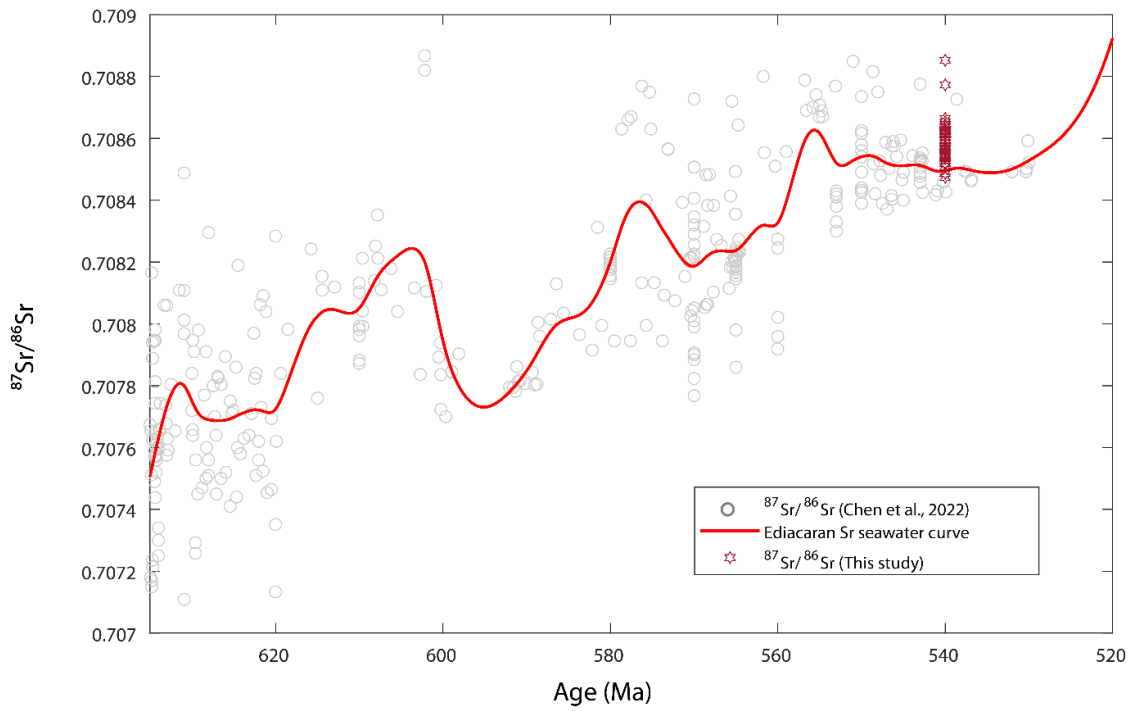

Figure 16: A. Neoproterozoic Sr seawater curve, B. Zoomed in Ediacaran Sr seawater curve. CFB = continental flood basalt. Curves A and B were generated in Matlab using the smoothing spline algorithm with the smoothing parameter set at 0.01 and 0.1 respectively. Data used to construct curve were from Chen et al., (2022).

6.5.2 South China

The Yangtze Gorges area of South China possesses Ediacaran Strata that have been extensively studied and are constrained by two ash bed U-Pb zircon dates of 635.2 ± 0.6 Ma and 550.14 ± 0.63 Ma (Condon et al., 2005; Yang et al., 2021). There is a dearth of ash beds in the Dengying Formation, which lies above the ash bed dated 550.14 ± 0.63 Ma, so correlation of younger strata is reliant on carbon isotope chemostratigraphy. The Lower Member of Dengying Formation (Hamajing Member/Algal Dolomite Member) is correlative to the Lower Zaris Formation and captures the shift from negative to positive $\delta^{13}C$ (Cui et al., 2019). The Middle Member (Shibantan Member/Gaojiashan Member) records the recently named Omkyk Excursion where $\delta^{13}C$ shift upwards from ~+2‰ to ~+6‰ which, as the name indicates, also occurs in the Omkyk Member of the Zaris Formation (Bowyer et al., 2022; Cui et al., 2019). The Upper Member (Baimatuo Member/ Beiwan Member) records a return to a $\delta^{13}C$ of ~+2‰ and the top of this member has been interpretated to be equivalent to the Nomstas Formation, which has been dated at 538.8 Ma in Namibia (Linnemann et al., 2019; Cui et al., 2019).

$^{87}Sr/^{86}Sr$ ratios for the Doushatuo Formation exhibit a smooth curve with two distinct large positive shifts and peak at ~0.7090 (Sawaki et al., 2010). The Hamajing and Shibantan members record consistent $^{87}Sr/^{86}Sr$ ratios of ~0.7084, which are similar to the Zaris Formation. There are currently no $^{87}Sr/^{86}Sr$ from the Baimatuo Member and as such it is unknown if the $^{87}Sr/^{86}Sr$ also increase to 0.7085 as is the case in the Schwarzrand Subgroup. The $^{87}Sr/^{86}Sr$ ratios were obtained from dolomite (Doushantuo Formation and Hamajing Member) and calcite (Shibantan Member) (Sawaki et al., 2010; Cui et al., 2019).

6.5.3 Oman

The Huqf Supergroup of Oman is a well-preserved continuous sequence of Ediacaran Strata and has been correlated with Nama and Yangtze Gorges sequences (Bowring et al., 2007; Fike et al., 2006). Glacial deposits at the top of the Abu Mahara Group have been pegged at ~635 Ma based on correlation with strata in South China and provide a lower age constraint (Fike et al., 2006). The upper age limit has been placed at ~541 Ma based on a U-Pb zircon date of 541.00 ± 0.13 Ma from an ash bed located in the A4 Member of the Ara Salt Formation (Bowring et al. 2007). Three ash beds located within the AO Member, near the base and near the top of the A3 Member have yielded respective U-Pb zircon dates of 546.72 ± 0.21 Ma,

542.90 ± 0.12 Ma and 542.33 ± 0.12 Ma. There are no ash beds in the Nafun Group and carbon isotope chemostratigraphy is currently the best tool for correlation. The $\delta^{13}C$ profile of the Nafun Group is the same as that of the Doushantuo Formation, including the Shuram Excursion – an event marked by the precipitous drop of $\delta^{13}C$ to negative values (between -12‰ and -8‰), named after the Shuram Formation of the Nafun Group where it was first recorded (Burns et al., 1994; Le Guerroué et al., 2006). The recovery to positive $\delta^{13}C$ values is recorded in the middle of the Buah Formation of the Nafun Group and is correlative to the Doushantuo-Dengying boundary and the Dabis-Zaris boundary, although it has recently been suggested that the excursion in the latter be termed as the Basal Nama Excursion (BANE) (Bowyer et al., 2022). Therefore, the middle of the Buah Formation can be pegged at 550.14 ± 0.63 Ma.

Similarly, the $^{87}Sr/^{86}Sr$ curve of the Nafun Group matches that of the Doushantuo Formation and it records a steady increase in $^{87}Sr/^{86}Sr$ from 0.7080 to 0.7090 (Burns et al., 1994). Critically, the rise in strontium isotopes ratios was fairly steep after the Shuram Excursion. All $^{87}Sr/^{86}Sr$ ratios were obtained from calcite and dolomite although it was not clearly reported on the exact number of calcite and dolomite samples respectively (Burns et al., 1994). The only available $^{87}Sr/^{86}Sr$ ratio from the Ara Salt Formation has a value of 0.709181 (Burns et al., 1994). Due to the restricted nature of basins during evaporite deposition, as well as the inconsistency with contemporaneous records, it is suggested that this is not reflective of the open marine Sr isotope composition.

6.5.4 Overview of correlated basins

The new radiometric ages from Nelson et al., (2022) and Linnemann et al., (2019), have improved chemostratigraphic correlation in the Ediacaran using $\delta^{13}C$ and $^{87}Sr/^{86}Sr$. The overall trend in the Ediacaran seawater $^{87}Sr/^{86}Sr$ curve (Figure 16B) shows an increase from 0.7080 to 0.7090 between ~635 Ma and 550 Ma before a decrease to ~0.7085 during the last 10 million years of the Ediacaran. The $\delta^{13}C$ chemostratigraphy is consistent with "Model C" proposed by Bowyer et al., (2022) which postulates a later onset of the basal Cambrian carbon isotope excursion (BACE) than the currently accepted date and also postulates a separate, short lived negative $\delta^{13}C$ excursion which has been termed the A0 excursion. This implies a younger Ediacaran-Cambrian Boundary age, which has been suggested to be as young as 535.5 Ma, but this date should be considered as speculative (Bowyer et al., 2022). The new

$^{87}Sr/^{86}Sr$ data from Zebra River and the Neint Nababeep Plateau, combined with recently published radiometric ages, provide a reliable, detailed $^{87}Sr/^{86}Sr$ framework for the last 2 Myr of the Ediacaran (Figure 17).

6.6 A decrease in seawater $^{87}Sr/^{86}Sr$ in the terminal Ediacaran

The drop from 0.7090 to 0.7085 between 550 Ma and 540 Ma is peculiar and there is no obvious explanation. It is well-established that the amalgamation of Gondwana involved collision and reworking of old Archean and Proterozoic rocks and these rocks had high $^{87}Sr/^{86}Sr$ (Goddéris et al., 2017). Moreover, there are no known CFBs which erupted during this time. Therefore, it is unlikely that the drop in $^{87}Sr/^{86}Sr$ ratios was due to increased non-radiogenic Sr input into seawater.

The culprit for the change in Sr composition of seawater could perhaps be related to climate, geography of continents or a combination of both. Palaeoclimate and palaeogeography of the Precambrian are poorly constrained and remain highly contested but the best available data show that most of the palaeocontinents were positioned in mid to low palaeolatitudes during the Ediacaran (Bradley, 2011; McCausland et al., 2011; Merdith et al., 2017; Wen et al., 2020). The spatial arrangement of continents during the terminal Ediacaran likely played a significant role in the rate of supply of strontium to global oceans with those continents in low palaeolatitudes contributing high volumes of sediment due to the higher temperatures, humidity and precipitation. Due to the generally high $^{87}Sr/^{86}Sr$ ratios observed for the Ediacaran, it is plausible that there was enhanced weathering of old, radiogenic Sr rich rocks influenced by location of the continents. The relief of the continents also played a critical role, since continents with higher relief experience increased chemical and physical weathering (Goddéris et al., 2017). The strontium isotope seawater curve is punctuated with peaks and troughs during the assembly of Gondwana (Figure 16) from 600 Ma until the Early Cambrian, when amalgamation ended and the supercontinent entered its tenured phase. Therefore, peaks in the $^{87}Sr/^{86}Sr$ curve, such as the one at ~550 Ma, could indicate orogen pulses and the troughs could be representative of lulls in continent-continent collisions. This is supported by the knowledge that assembly of Gondwana occurred in stages, facilitated by rapid phases of continental motions (Merdith et al., 2017).

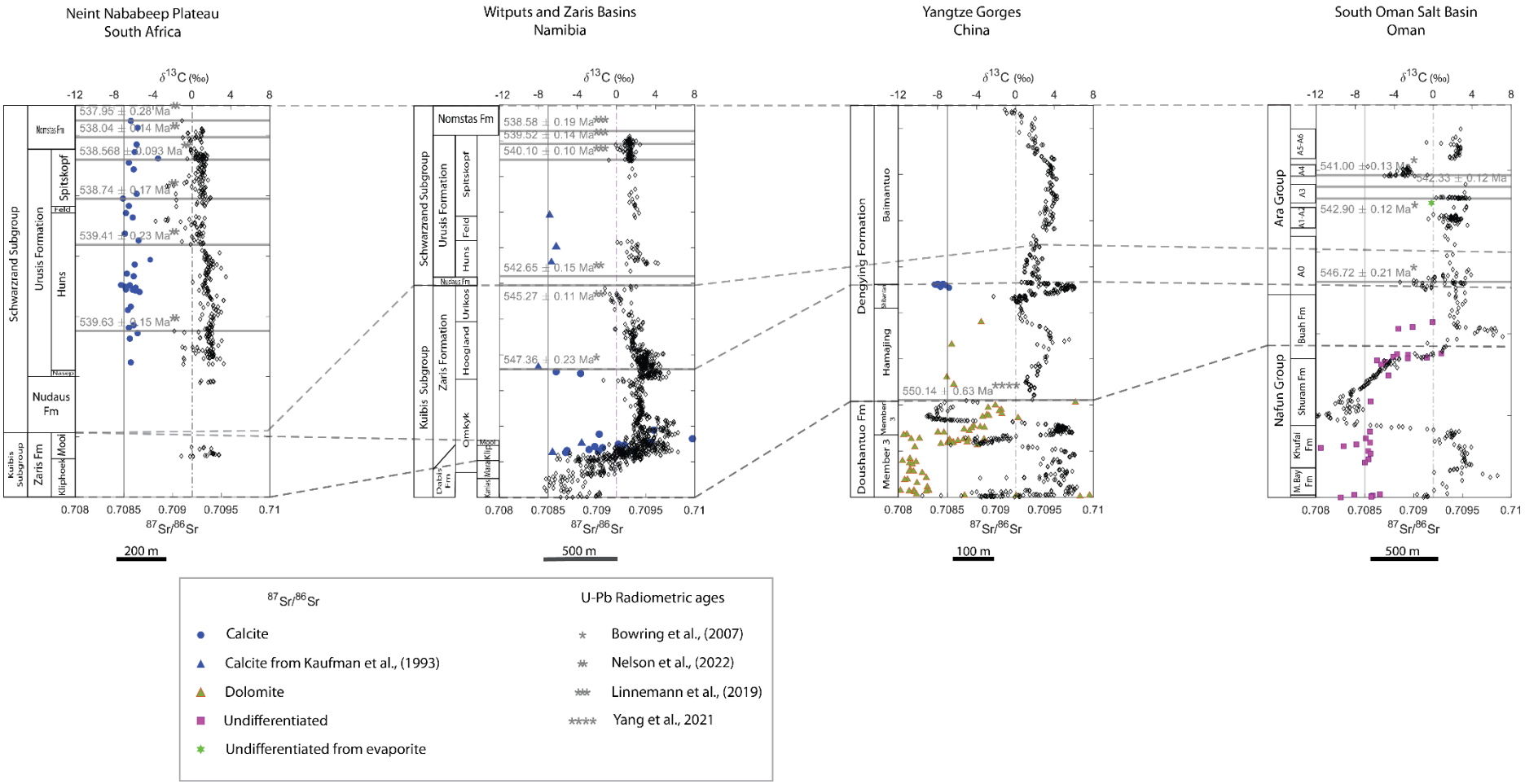

Figure 17: Correlation of Neint Nababeep Plateau with well-studied Ediacaran basins. Neint Nababeep Plateau and some of the Namibian Basin data are from this study. South China ratios are from Sawaki et al., (2010) and Cui et al., (2019), and Oman ratios are from Burns et al., (1994). $\delta^{13}C$ data for Neint Nababeep Plateau are from this study and Nelson et al., (2022). The $\delta^{13}C$ from Namibia are from Bowyer et al., (2022), and South China data are from Cui et al., (2019) and Sawaki et al., (2010). The black filled dots are $\delta^{13}C$.

Alternatively, Palaeoclimatic cooling could have been the driver for the downturn in continental weathering. Chemical index of alteration (CIA) data provide evidence for decreased chemical weathering rates in the locality of the Nama basins. The index is calculated using molar proportions and is expressed as:

$$CIA = [Al_2O_3/(Al_2O_3 + CaO + Na_2O + K_2O)]$$

The aluminium cation (Al^{3+}) is immobile while Ca^{2+}, Na^{+} and K^{+} are labile and as such, highly weathered siliciclastic sediments are enriched in Al^{3+} and depleted in the other three cations, yielding high CIA values (Nesbitt & Young, 1982). CIA analysis of the Zaris and WItputs sub-basins show high CIA ratios for the Kuibis Subgroup and low ratios for the Schwarzrand subgroup, which is indicative of a drop-off in the rate of weathering (Bowyer et al., 2020). Similarly, CIA data from Yangtze Block, South China show a transient drop in ratios between the terminal Ediacaran and early Cambrian (Zhang et al., 2018). It has been postulated that regional glaciation was responsible for the fall in chemical weathering rates in the locality of the Nama Group basins while arid and cold climatic conditions have been suggested to be the cause for the downward change in chemical weathering rates in the locality of South China Ediacaran basins (Bowyer et al., 2020; Zhai et al., 2018). There is also evidence for regional glaciations on multiple palaeocontinents during the terminal Ediacaran (Chumakov, 2011; Gaucher & Poiré, 2009; Germs & Gaucher, 2012; Hambrey & Harland, 1985; Shen et al., 2010). Unlike the Cryogenian snowball Earth events, terminal Ediacaran glaciations were restricted to mid to high latitude localities. The correlation of regional CIA data with global $^{87}Sr/^{86}Sr$ suggests that the effect of change in palaeoclimate (cooling) was severe enough to affect weathering rates and occurred over substantial geologic time to affect the Sr isotope composition of seawater during the terminal Ediacaran and possibly the early Cambrian. Therefore, the available evidence favours the interpretation that palaeoclimate was the main contributing factor towards the drop in $^{87}Sr/^{86}Sr$ values during the terminal Ediacaran.

6.7 Influence on evolution of biomineralizing metazoans

Skeletal organisms emerged around the same time as the maximum observed $^{87}Sr/^{86}Sr$ ca 550 Ma and this warrants further discussion. Although the resolution of $^{87}Sr/^{86}Sr$ ratios during this time can be improved, there is mounting evidence for a decrease in seawater Sr isotope composition. Further sampling at higher resolution will hopefully properly capture the transition from ~0.7090 to ~0.7085 and hopefully correlate the ratios to the emergence of

biomineralizing metazoans. Nevertheless, it would appear that the Neoproterozoic Period generally experienced an increase in seawater $^{87}Sr/^{86}Sr$ ratios and this may have been accompanied by an increase in $CaCO_3$ saturation, which would have been conducive for biomineralization. The extent of $CaCO_3$ saturations influence on biomineralization is unknown. Further, continental weathering and nutrient input may drive anoxia, and limit available dissolved free oxygen, which is also an important parameter for biomineralization. Regardless, overlaying the $^{87}Sr/^{86}Sr$ data with other geochemical data provides an insight into the interplay of these different factors. $\delta^{238}U$ from both the Nama Group and Dengying Formation show spreading global marine anoxia ca. 547 Ma (Tostevin et al., 2019b; Zhang et al., 2018). However, phosphorus, iodine, cerium anomalies and iron speciation data from the Nama Basin all show that stable but transient oxic conditions were attained at various times prior to 547 Ma in the Nama Group locality (Bowyer et al., 2020; Tostevin, Shields, et al., 2016; Tostevin, Wood, et al., 2016; Uahengo et al., 2020; R. A. Wood et al., 2015). Matching of Palaeontological and geochemical data from the Nama Basin also reveals a preponderance of skeletal animal fossils in oxic intervals and near absence of the same fossils in suboxic intervals (Tostevin et al., 2016b; Wood et al., 2015). Therefore, skeletal animals were thriving in shallow, oxic oases regardless of global trends in the extent of anoxia. Similarly, Wood et al., (2017), suggested that biomineralisation was controlled by local changes in carbonate saturation across the shelf, independent of global trends.

7 Chapter 7: Conclusions and ideas for future research

7.1 Conclusions

The work carried out in this study focused on the less studied South African section of the Nama Group, in the Neint Nababeep Plateau area and the overarching aim was to generate primary $^{87}Sr/^{86}Sr$ data through the terminal stage of the Ediacaran, to enable high resolution chemostratigraphy and constrain continental weathering rates, and ultimately, providing context for the evolution of skeletal biota.

The main outcomes from the study can be summarised as:

- Carbon isotopes and Ce anomaly data of the Neint Nababeep Plateau are similar to those of the Namibian section indicating similar conditions across the basin
- Diagenetic screening using trace elements ratios and $\delta^{18}O$ was successfully employed to identify very diagenetically altered samples and separate them from less diagenetically altered samples.
- The sequential digestion method first developed by Bailey et al., (2000) was successfully used on Precambrian bulk rock samples and yielded very good data. The use of sequential digestion highlighted two things: 1) it reinforced and vindicated the diagenetic screening process used to select samples, 2) it showed that the middle 40% digest provided the lowest $^{87}Sr/^{86}Sr$ ratios.
- The sequential leaching technique may not be necessary for well-preserved samples but is absolutely vital for samples with a high degree of diagenetic alteration.
- $^{87}Sr/^{86}Sr$ ratios obtained from the Huns, Spitskopf members and Nomstas Formation of the Neint Nababeep Plateau section are very consistent (~0.7085) and represent the best available and well age-constrained data for the last 2 million years of the Ediacaran, based on the recently obtained radiometric ages by Nelson et al., (2022).
- By correlating with other global Ediacaran strata, it has been shown that $^{87}Sr/^{86}Sr$ ratios dropped from ~0.7090 to ~0.7085 in the time between 551 Ma and 547 Ma and I suggest that this is due to a downturn in continental weathering rates, driven by climatic change.
- This study has improved inter-continental stratigraphic correlations for the terminal Neoproterozoic, and as such, will enhance our ability to compare different palaeontological records.

7.2 Future work

The Neint Nababeep Plateau represents a near complete sequence of the Kuibis Subgroup and a complete sequence of Schwarzrand Subgroup strata and this makes it extremely favourable for conducting further geochemical analyses. Further research would focus on increasing the geochemical resolution in the lower Nama Group (sampling at shorter intervals) and also improving our comprehension of the relationship between continental weathering and redox conditions of seawater during the last 10 million years of the Ediacaran. The impact of weathering on redox changes and by extension, impact on biomineralization can be investigated further by using Li isotopes. Lithium isotope systematics only depend on weathering of aluminosilicates and can provide complementary constraints on weathering rates. Further, Li has a shorter seawater residence time of ~1 Ma and can potentially capture changes in weathering rates on smaller timescales. More sophisticated redox sensitive proxies can also be used to further investigate changes in seawater oxygenation during the terminal Ediacaran and these proxies are such as molybdenum, selenium and uranium isotopes as well as redox sensitive elements such as Mo, U and V. This would hopefully improve our understanding of the rise in oxygenation in terminal Ediacaran oceans, a time notable for important evolutionary innovations.

8 References

Ahm, A. S. C., Maloof, A. C., MacDonald, F. A., Hoffman, P. F., Bjerrum, C. J., Bold, U., Rose, C. V., Strauss, J. V. & Higgins, J. A. (2019). An early diagenetic deglacial origin for basal Ediacaran “cap dolostones”. Earth and Planetary Science Letters 506, 292–307

Alibo, D. S., & Nozaki, Y. (1999). Rare earth elements in seawater: particle association, shale-normalization, and Ce oxidation. *Geochimica et Cosmochimica Acta*, *63*(3–4), 363–372.

Allègre, C. J., Louvat, P., Gaillardet, J., Meynadier, L., Rad, S., & Capmas, F. (2010). The fundamental role of island arc weathering in the oceanic Sr isotope budget. *Earth and Planetary Science Letters*, *292*(1–2), 51–56.

Amthor, J. E., Grotzinger, J. P., Schrö, S., Bowring, S. A., Ramezani, J., & Martin, M. W. (2003). Extinction of *Cloudina* and *Namacalathus* at the Precambrian-Cambrian boundary in Oman. *Geology*, *31*(5), 431–434.

Antcliffe, J. B. (2013). Questioning the evidence of organic compounds called sponge biomarkers. *Palaeontology*, *56*(5), 917–925.

Baadsgaard, H., Cumming, G. L., Folinsbee, R. E., & Godfrey, J. D. (2020). Limitations of radiometric dating. In *Geochronology in Canada,* 20-38. University of Toronto Press.

Bailey, T. R., Mcarthur, J. M., Prince, H., & Thirlwall, M. F. (2000). Dissolution methods for strontium isotope stratigraphy: whole rock analysis. *Chemical Geology*, *167*(3–4), 313–319.

Balthasar, U., & Cusack, M. (2014). Aragonite-calcite seas - quantifying the gray area. *Geology*, *43*(2), 99–102.

Banner, J. L. (1995). Application of isotope and trace element and isotope geochemistry of strontium to studies of carbonate diagenesis. *Sedimentology*, *42*(5), 805–824.

Banner, J. L., & Hanson, G. N. (1990). Calculation of simultaneous isotopic and trace element variations during water-rock interaction with applications to carbonate diagenesis. *Geochimica et Cosmochimica Acfa*, *54*(11), 3123–3137.

Banner, J. L., Hanson, G. N., & Meyers, W. J. (1988). Rare earth element and Nd isotopic variations in regionally extensive dolomites from the Burlington-Keokuk Formation (Mississippian); implications for REE mobility during carbonate diagenesis. *Journal of Sedimentary Research*, *58*(3), 415–432.

Bellefroid, E. J., Planavsky, N. J., Miller, N. R., Brand, U., & Wang, C. (2018). Case studies on the utility of sequential carbonate leaching for radiogenic strontium isotope analysis. *Chemical Geology*, *497*, 88–99.

Bender, M. L. (1982). Trace elements and ocean chemistry. *Nature*, *296*(5854), 203–204.

Bennett, W. W., & Canfield, D. E. (2020). Redox-sensitive trace metals as paleoredox proxies: a review and analysis of data from modern sediments. *Earth-Science Reviews*, *204*.

Berger, W. H., & Vincent, E. (1986). Deep-sea carbonates: Reading the carbon-isotope signal. *Geologische Rundschau*, *75*(1), 249–269.

Blanco, G., Germs, G. J. B., Rajesh, H. M., Chemale, F., Dussin, I. A., & Justino, D. (2011). Provenance and paleogeography of the Nama Group (Ediacaran to early Palaeozoic, Namibia): petrography, geochemistry and U-Pb detrital zircon geochronology. *Precambrian Research*, *187*(1–2), 15–32.

Bots, P., Benning, L. G., Rickaby, R. E. M., & Shaw, S. (2011). The role of SO_4 in the switch from calcite to aragonite seas. *Geology*, *39*(4), 331–334.

Boudinot, F. G., Kopf, S., Dildar, N., & Sepúlveda, J. (2021). Carbon Cycling During Oceanic Anoxic Event 2: compound-specific carbon isotope evidence from the Western Interior Seaway. *Paleoceanography and Paleoclimatology*, *36*(9).

Bowring, S. A., Grotzinger, J. P., Condon, D. J., Ramezani, J., Newall, M. J., & Allen, P. A. (2007). Geochronologic constraints on the chronostratigraphic framework of the neoproterozoic Huqf Supergroup, Sultanate of Oman. *American Journal of Science*, *307*(10), 1097–1145.

Bowyer, F. T., Shore, A. J., Wood, R. A., Alcott, L. J., Thomas, A. L., Butler, I. B., Curtis, A., Hainanan, S., Curtis-Walcott, S., Penny, A. M., & Poulton, S. W. (2020). Regional nutrient decrease drove redox stabilisation and metazoan diversification in the late Ediacaran Nama Group, Namibia. *Scientific Reports*, *10*(1), 1–11.

Bowyer, F. T., Zhuravlev, A. Y., Wood, R., Shields, G. A., Zhou, Y., Curtis, A., Poulton, S. W., Condon, D. J., Yang, C., & Zhu, M. (2022). Calibrating the temporal and spatial dynamics of the Ediacaran - Cambrian radiation of animals. *Earth-Science Reviews*, *225*, 103913.

Bradley, D. C. (2011). Secular trends in the geologic record and the supercontinent cycle. In *Earth-Science Reviews,* 108(1–2), 16–33.

Brain, C. K. (2001). Some observations on *Cloudina*, a terminal Proterozoic index fossil from Namibia. *Jounal of African Earth Sciences*, *33*(3–4), 475–480.

Brand, U., & Veizer, J. (1980). Chemical diagenesis of a multicomponent carbonate system; 1, trace elements. *Journal of Sedimentary Research*, *50*(4), 1219–1236.

Brocks, J. J., Jarrett, A. J. M., Sirantoine, E., Hallmann, C., Hoshino, Y., & Liyanage, T. (2017). The rise of algae in Cryogenian oceans and the emergence of animals. *Nature*, *548*(7669), 578–581.

Brown, M. (2006). Duality of thermal regimes is the distinctive characteristics of plate tectonics since the Neoarchean. *Geology*, *34*(11), 961–964.

Brown, M., Johnson, T., & Gardiner, N. J. (2020). Plate Tectonics and the Archean Earth. *Annual Review of Earth and Planetary Sciences*, *48*, 291–320.

Burke, W. H., Denison, R. E., Hetherington, E. A., Koepnick, R. B., Nelson, H. F., & Otto, J. B. (1982). Variation of seawater $^{87}Sr/^{86}Sr$ throughout Phanerozoic time. *Geology*, *10*(10), 516–519.

Burns, S. J., Haudenschild, U., & Matter, A. (1994). The strontium isotopic composition of carbonates from the late Precambrian (~560-540 Ma) Huqf Group of Oman. *Chemical Geology* , *111*(1–4), 269–282.

Butterfield, N. J. (2009). Modes of pre-Ediacaran multicellularity. *Precambrian Research*, *173*(1–4), 201–211.

Byrne, R. H., & Kim, K. H. (1990). Rare earth element scavenging in seawater. *Geochimica et Cosmochimica Acta*, *54*(10), 2645–2656.

Calver, C. R. (2000). Isotope stratigraphy of the Ediacaran (Neoproterozoic III) of the Adelaide Rift Complex, Australia, and the overprint of water column stratification. *Precambrian Research*, *100*(1–3), 121–150.

Canfield, D. E., Ngombi-Pemba, L., Hammarlund, E. U., Bengtson, S., Chaussidon, M., Gauthier-Lafaye, F., Meunier, A., Riboulleau, A., Rollion-Bard, C., Rouxel, O., Asael, D., Pierson-Wickmann, A. C., & el Albani, A. (2013). Oxygen dynamics in the aftermath of the Great Oxidation of Earth's atmosphere. *Proceedings of the National Academy of Sciences of the United States of America*, *110*(42), 16736–16741.

Canfield, D. E., Poulton, S. W., & Narbonne, G. M. (2007). Late-Neoproterozoic deep-ocean oxygenation and the rise of animal life. *Science*, *315*(5808), 92–95.

Canfield, D. E., & Thamdrup, B. (2009). Towards a consistent classification scheme for geochemical environments, or, why we wish the term 'suboxic' would go away. *Geobiology*, *7*(4), 385–392.

Cao, C., Liu, X.-M., Bataille, C. P., & Liu, C. (2020). What do Ce anomalies in marine carbonates really mean? A perspective from leaching experiments. *Chemical Geology*, *532*, 119413.

Carpenter, S. J., & Lohmann, K. C. (1992). Sr /Mg ratios of modern marine calcite: Empirical indicators of ocean chemistry and precipitation rate. *Geochimica et Cosmichimica Acta*, *56*(5), 1837–1849.

Carpenter, S. J., Lohmann, K. C., Holden, P., Walter, L. M., Huston, T. J., & Halliday, A. N. (1991). δ18O values, $^{87}Sr/^{86}Sr$ and Sr/Mg ratios of late Devonian abiotic marine calcite: implications for the composition of ancient seawater. *Geochimica et Cosmochimica Acta*, *55*(7), 1991–2010.

Cawood, P. A., Zhao, G., Yao, J., Wang, W., Xu, Y., & Wang, Y. (2018). Reconstructing South China in Phanerozoic and Precambrian supercontinents. *Earth-Science Reviews*, *186*, 173–194.

Chen, X., Zhou, Y., & Shields, G. A. (2022). Progress towards an improved Precambrian seawater $^{87}Sr/^{86}Sr$ curve. In *Earth-Science Reviews,* 224.

Chumakov, N. M. (2011). Late Proterozoic African glacial era. *Stratigraphy and Geological Correlation*, *19*(1), 1–20.

Colbourn, G., Ridgwell, A., & Lenton, T. M. (2015). The time scale of the silicate weathering negative feedback on atmospheric CO2. *Global Biogeochemical Cycles*, *29*(5), 583–596.

Condon, D., Zhu, M., Bowring, S., Wang, W., Yang, A., & Jin, Y. (2005). U-Pb Ages from the Neoproterozoic Doushantuo Formation, China. *Science*, *308*(5718), 95–98.

Conway Morris, S., Mattes, B. W., & Menge, C. (1990). The early skeletal organism *Cloudina*: new occurrences from Oman and possibly China. *American Journal of Science*, *290*, 245–260.

Cox, G. M., Halverson, G. P., Stevenson, R. K., Vokaty, M., Poirier, A., Kunzmann, M., Li, Z. X., Denyszyn, S. W., Strauss, J. v., & Macdonald, F. A. (2016). Continental flood basalt weathering as a trigger for Neoproterozoic Snowball Earth. *Earth and Planetary Science Letters*, *446*, 89–99.

Craig, H. (1953). The geochemistry of the stable carbon isotopes. *Geochemica et Cosmochimicha Acta*, *3*(2–3), 53–92.

Cui, H., Xiao, S., Cai, Y., Peek, S., Plummer, R. E., & Kaufman, A. J. (2019). Sedimentology and chemostratigraphy of the terminal Ediacaran Dengying Formation at the Gaojiashan section, South China. *Geological Magazine*.

DePaolo, D. J., & Ingram, B. L. (1985). High-resolution stratigraphy with strontium isotopes. *Science*, *227*(4689), 938–941.

Derry, L. A., Kaufman, A. J., & Jacobsen, S. B. (1992). Sedimentary cycling and environmental change in the late Proterozoic: evidence from stable and radiogenic isotopes. *Geochimica n Cosmochimica Acta*, *56*(3), 1317–1329.

Derry, L. A., Keto, L. S., Jacobsen, S. B., Knoll, A. H., & Swett, K. (1989). Sr isotopic variations in Upper Proterozoic carbonates from Svalbard and East Greenland. *Geochimica et Cosmochimica Acta*, *53*(9), 2331–2339.

Diaz, M. R., & Eberli, G. P. (2019). Decoding the mechanism of formation in marine ooids: a review. *Earth-Science Reviews*, *190*, 536–556.

Droser, M. L., & Gehling, J. G. (2015). The advent of animals: the view from the Ediacaran. *Proceedings of the National Academy of Sciences of the United States of America*, *112*(16), 4865–4870.

Droser, M. L., Gehling, J. G., & Jensen, S. R. (2006). Assemblage palaeoecology of the Ediacara biota: the unabridged edition? *Palaeogeography, Palaeoclimatology, Palaeoecology*, *232*(2–4), 131–147.

Droser, M. L., Tarhan, L. G., & Gehling, J. G. (2017). The rise of animals in a changing environment: global ecological innovation in the late Ediacaran. *Annual Review of Earth and Planetary Sciences*, *45*, 593–617.

Elderfield, H. (1986). Strontium isotope stratigraphy. *Palaeogeography, Palaeoclimatology, Palaeoecology*, *57*(1), 71–90.

Elderfield, H., & Greaves, M. J. (1983). Determination of the rare earth elements in sea water. In *Trace metals in sea water* (pp. 427–445). Springer.

Elderfield, H., Upstill-Goddard, R., & Sholkovitz, E. R. (1990). The rare earth elements in rivers, estuaries, and coastal seas and their significance to the composition of ocean waters. *Geochimica et Cosmochimica Acta*, *54*(4), 971–991.

Elderfield, H., Whitfield, M., Burton, J. D., Bacon, M. P., & Liss, P. S. (1988). The oceanic chemistry of the rare-earth elements [and discussion]. *Philosophical Transactions of the Royal Society of London. Series A, Mathematical and Physical Sciences*, *325*(1583), 105–126.

Ernst, R. E., Bleeker, W., Söderlund, U., & Kerr, A. C. (2013). Large igneous provinces and supercontinents: toward completing the plate tectonic revolution. *Lithos,* 174, 1–14.

Farquhar, G. D., Ehleringer, J. R., & Hubick, K. T. (1989). Carbon isotope discrimination and photosynthesis. *Annual Review of Plant Biology*, *40*(1), 503–537.

Faure, G., Assereto, R., & Tremba, E. L. (1978). Strontium isotope composition of marine carbonates of Middle Triassic to Early Jurassic age, Lombardic Alps, Italy. *Sedimentology*, *25*(4), 523–543.

Faure, G., & Mensing, T. M. (2005). *Isotopes - Principles and Applications* (3rd ed.). John Wiley & Sons, Inc.

Faure, G., & Powell, J. L. (1972). The geochemistry of rubidium and strontium. In *Strontium isotope geochemistry* (pp. 1–8). Springer.

Fike, D. A., Grotzinger, J. P., Pratt, L. M., & Summons, R. E. (2006). Oxidation of the Ediacaran ocean. *Nature*, *444*(7120), 744–747.

Folk, R. L. (1980). *Petrology of Sedimentary Rocks*. Hemphill Publishing Company.

Gaucher, C., & Poiré, D. G. (2009). Chapter 4.5 palaeoclimatic events. *Developments in Precambrian Geology*, *16*, 123–130.

Ge, L., Jiang, S. Y., Swennen, R., Yang, T., Yang, J. H., Wu, N. Y., Liu, J., & Chen, D. H. (2010). Chemical environment of cold seep carbonate formation on the northern continental slope of South China Sea: evidence from trace and rare earth element geochemistry. *Marine Geology*, *277*(1–4), 21–30.

German, C. R., & Elderfield, H. (1990). Application of the Ce anomaly as a paleoredox indicator: the ground rules. *Paleoceanography*, *5*(5), 823–833.

Germs, G. J. B. (1972). New shelly fossils from Nama Group, South West Africa. *American Journal of Science*, *272*(8), 752–761.

Germs, G. J. B. (1983). *Implications of a sedimentary facies and depositional environmental analysis of the Nama Group in South West Africa/Namibia.*

Germs, G. J. B. (1995). The Neoproterozoic of southwestern Africa, with emphasis on platform stratigraphy and paleontology. *Precambrian Research*, *73*(1–4), 137–151.

Germs, G. J. B., & Gaucher, C. (2012). Nature and extent of a late Ediacaran (ca. 547 Ma) glacigenic erosion surface in southern Africa. *South African Journal of Geology*, *115*(1), 91–102.

Germs, G. J. B., Knoll, A. H., & Vidal, G. (1986). Latest Proterozoic microfossils from the Nama Group, Namibia (South West Africa). *Precambrian Research*, *32*(1), 45–62.

Goddéris, Y., le Hir, G., Macouin, M., Donnadieu, Y., Hubert-Théou, L., Dera, G., Aretz, M., Fluteau, F., Li, Z. X., & Halverson, G. P. (2017). Paleogeographic forcing of the strontium isotopic cycle in the Neoproterozoic. *Gondwana Research*, *42*, 151–162.

Gold, D. A., Caron, A., Fournier, G. P., & Summons, R. E. (2017). Paleoproterozoic sterol biosynthesis and the rise of oxygen. *Nature*, *543*(7645), 420–423.

Grammer, G. M., & Ginsburg, R. N. (1992). Highstand versus lowstand deposition on carbonate platform margins: insight from Quaternary foreslopes in the Bahamas. *Marine Geology*, *103*(1), 125–136.

Grant, S. W. F. (1990). Shell structure and distribution of *Cloudina*, a potential index fossil for the terminal Proterozoic. *American Journal of Science*, *290*, 261–294.

Grazhdankin, D. (2004). Patterns of distribution in the Ediacaran biotas: facies versus biogeography and evolution. *Paleobiology*, *30*(2), 203–221.

Greber, N. D., Dauphas, N., Bekker, A., Ptáček, M. P., Bindeman, I. N., & Hofmann, A. (2017). Titanium isotopic evidence for felsic crust and plate tectonics 3.5 billion years ago. *Science*, *357*(6357), 1271–1274.

Gresse, P. G., & Germs, G. J. B. (1993). The Nama foreland basin: sedimentation, major unconformity bounded sequences and multisided active margin advance. *Precambrian Research*, *63*(3–4), 247–272.

Grotzinger, J. P., Bowring, S. A., Saylor, B. Z., & Kaufman, A. J. (1995). Biostratigraphic and geochronologic constraints on early animal evolution. *Science*, *270*(5236), 598–604.

Grotzinger, J. P., Watters, W. A., & Knoll, A. H. (2000). Calcified metazoans in thrombolite-stromatolite reefs of the terminal Proterozoic Nama Group, Namibia. *Paleobiology*, *26*(3), 334–359.

Halverson, G. P., Dudás, F. Ö., Maloof, A. C., & Bowring, S. A. (2007). Evolution of the $^{87}Sr/^{86}Sr$ composition of Neoproterozoic seawater. *Palaeogeography, Palaeoclimatology, Palaeoecology*, *256*(3–4), 103–129.

Hambrey, M. J., & Harland, W. B. (1985). The late Proterozoic glacial era. *Palaeogeography, Palaeoclimatology, Palaeoecology*, *51*(1), 255–272.

Hawkesworth, C. J., Cawood, P. A., & Dhuime, B. (2020). The evolution of the continental crust and the onset of plate tectonics. *Frontiers in Earth Science*, *8*, 326.

Hawkesworth, C. J., Cawood, P. A., Dhuime, B., & Kemp, T. I. S. (2017). Earth's continental lithosphere through time. *Annual Review of Earth and Planetary Sciences*, *45*, 169–198.

Hedges, S. B., Blair, J. E., Venturi, M. L., & Shoe, J. L. (2004). A molecular timescale of eukaryote evolution and the rise of complex multicellular life. *BMC Evolutionary*, *4*(1), 1–9.

Higgins, J.A., Blättler, C.L., Lundstrom, E.A., Santiago-Ramos, D.P., Akhtar, A.A., Ahm, A.C., Bialik, O., Holmden, C., Bradbury, H., Murray, S.T. & Swart, P.K., 2018. Mineralogy, early marine diagenesis, and the chemistry of shallow-water carbonate sediments. *Geochimica et Cosmochimica Acta*, *220*, 512–534

Hoefs, J., & Hoefs, J. (1997). *Stable isotope geochemistry* (Vol. 201). Springer.

Howarth, G. H., Moore, A. E., Harris, C., van der Meer, Q. H. A., & le Roux, P. (2019). Crustal versus mantle origin of carbonate xenoliths from Kimberley region kimberlites using C-O-Sr-Nd-Pb isotopes and trace element abundances. *Geochimica et Cosmochimica Acta*, *266*, 258–273.

Hua, H., Chen, Z., Yuan, X., Zhang, L., & Xiao, S. (2005). Skeletogenesis and asexual reproduction in the earliest biomineralizing animal *Cloudina*. *Geology*, *33*(4), 277–280.

James, R. H., Elderfield, H., & Palmer, M. R. (1995). The chemistry of hydrothermal fluids from the Broken Spur site, 29"N Mid-Atlantic Ridge. *Geochimlca et Cosmochimica Acta*, *59*(4), 651–659.

Jenkyns, H. C. (1995). Carbon-isotope stratigraphy and paleoceanographic significance of the Lower Cretaceous shallow-water carbonates of Resolution Guyot, Mid-Pacific Mountains. In *Proceedings of the Ocean Drilling Program, Scientific Results* (Vol. 143, pp. 99–104).

Jenkyns, H. C., Galef, A. S., & Corfield, R. M. (1994). Carbon-and oxygen-isotope stratigraphy of the English Chalk and Italian Scaglia and its palaeoclimatic significance. *Geological Magazine*, *131*(1), 1–34.

Jiang, G., Kaufman, A. J., Christie-Blick, N., Zhang, S., & Wu, H. (2007). Carbon isotope variability across the Ediacaran Yangtze platform in South China: implications for a large surface-to-deep ocean $\delta^{13}C$ gradient. *Earth and Planetary Science Letters*, *261*(1–2), 303–320.

Kaufman, A. J., Hayes, J. M., Knoll, A. H., & Germs, G. J. B. (1991). Isotopic compositions of carbonates and organic carbon from upper Proterozoic successions in Namibia: stratigraphic variation and the effects of diagenesis and metamorphism. *Precambrian Research*, *49*(3–4), 301–327.

Kaufman, A. J., Jacobsen, S. B., & Knoll, A. H. (1993). The Vendian record of Sr and C isotopic variations in seawater: implications for tectonics and paleoclimate. *Earth and Planetary Science Letters*, *120*(3–4), 409–430.

Knoll, A. H. (2003). Biomineralization and evolutionary history. *Reviews in Mineralogy and Geochemistry*, *54*(1), 329–356.

Knoll, A. H., Javaux, E. J., Hewitt, D., & Cohen, P. (2006). Eukaryotic organisms in Proterozoic oceans. *Philosophical Transactions of the Royal Society B: Biological Sciences*, *361*(1470), 1023–1038.

Kuznetsov, A. B., Semikhatov, M. A., & Gorokhov, I. M. (2018). Strontium isotope stratigraphy: principles and state of the art. *Stratigraphy and Geological Correlation*, *26*(4), 367–386.

Laflamme, M., Darroch, S. A. F., Tweedt, S. M., Peterson, K. J., & Erwin, D. H. (2013). The end of the Ediacara biota: extinction, biotic replacement, or Cheshire Cat? *Gondwana Research,* 23(2), 558–573.

Lawrence, M. G., Greig, A., Collerson, K. D., & Kamber, B. S. (2006). Rare earth element and yttrium variability in South East Queensland waterways. *Aquatic Geochemistry*, *12*(1), 39–72.

Li, D., Shields-Zhou, G. A., Ling, H. F., & Thirlwall, M. (2011). Dissolution methods for strontium isotope stratigraphy: guidelines for the use of bulk carbonate and phosphorite rocks. *Chemical Geology*, *290*(3–4), 133–144.

Linnemann, U., Ovtcharova, M., Schaltegger, U., Gärtner, A., Hautmann, M., Geyer, G., Vickers-Rich, P., Rich, T., Plessen, B., Hofmann, M., Zieger, J., Krause, R., Kriesfeld, L., & Smith, J. (2019). New high-resolution age data from the Ediacaran–Cambrian boundary indicate rapid, ecologically driven onset of the Cambrian explosion. *Terra Nova*, *31*(1), 49–58.

Liu, X. M., Hardisty, D. S., Lyons, T. W., & Swart, P. K. (2019). Evaluating the fidelity of the cerium paleoredox tracer during variable carbonate diagenesis on the Great Bahamas Bank. *Geochimica et Cosmochimica Acta*, *248*, 25–42.

Love, G. D., Grosjean, E., Stalvies, C., Fike, D. A., Grotzinger, J. P., Bradley, A. S., Kelly, A. E., Bhatia, M., Meredith, W., Snape, C. E., Bowring, S. A., Condon, D. J., & Summons, R. E. (2009). Fossil steroids record the appearance of *Demospongiae* during the Cryogenian period. *Nature*, *457*(7230), 718–721.

Love, G. D., & Summons, R. E. (2015). The molecular record of Cryogenian sponges - a response to Antcliffe (2013). *Palaeontology*, *58*(6), 1131–1136.

Lyons, T. W., Diamond, C. W., Planavsky, N. J., Reinhard, C. T., & Li, C. (2021). Oxygenation, life, and the planetary system during earth's middle history: an overview. *Astrobiology*, *21*(8), 906–923.

Maloof, A. C., Rose, C. v., Beach, R., Samuels, B. M., Calmet, C. C., Erwin, D. H., Poirier, G. R., Yao, N., & Simons, F. J. (2010). Possible animal-body fossils in pre-Marinoan limestones from South Australia. *Nature Geoscience*, *3*(9), 653–659.

Marshall, J. D. (1992). Climatic and oceanographic isotopic signals from the carbonate rock record and their preservation. *Geological Magazine*, *129*(2), 143–160.

Mashego, M. (2020). *The use of Ce anomalies for tracking oxygen levels in Ediacaran shelf environments*. UCT (University of Cape Town).

McArthur, J., & Howarth, R. J. (2005). Strontium isotope stratigraphy. In *A Geologic Time Scale 2004* (pp. 96–105). Cambridge University Press.

McArthur, J. M. (1994). Recent trends in strontium isotope stratigraphy. *Terra Nova*, *6*(4), 331–358.

McArthur, J. M., Howarth, R. J., & Shields, G. A. (2012). Strontium isotope stratigraphy. In *The Geologic Time Scale 2012* (pp. 127–144). Elsevier B.V.

McCausland, P. J. A., Hankard, F., van der Voo, R., & Hall, C. M. (2011). Ediacaran paleogeography of Laurentia: paleomagnetism and ^{40}Ar-^{39}Ar geochronology of the 583Ma Baie des Moutons syenite, Quebec. *Precambrian Research*, *187*(1–2), 58–78.

Mehra, A., Watters, W. A., Grotzinger, J. P., & Maloof, A. C. (2020). Three-dimensional reconstructions of the putative metazoan Namapoikia show that it was a microbial construction. *Proceedings of the National Academy of Sciences of the United States of America*, *117*(33), 19760–19766.

Merdith, A. S., Collins, A. S., Williams, S. E., Pisarevsky, S., Foden, J. D., Archibald, D. B., Blades, M. L., Alessio, B. L., Armistead, S., Plavsa, D., Clark, C., & Müller, R. D. (2017). A full-plate global reconstruction of the Neoproterozoic. *Gondwana Research*, *50*, 84–134.

Mills, D. B., Ward, L. M., Jones, C. A., Sweeten, B., Forth, M., Treusch, A. H., & Canfield, D. E. (2014). Oxygen requirements of the earliest animals. *Proceedings of the National Academy of Sciences of the United States of America*, *111*(11), 4168–4172.

Mucci, A. (1986). Growth kinetics and composition of magnesian calcite overgrowths precipitated from seawater: quantitative influence of orthophosphate ions. *Geochimica et Cosmochimica Acta*, *50*(10), 2255–2265.

Mucci, A., & Morse, J. W. (1983). The incorporation of Mg^{2+} and Sr^{2+} into calcite overgrowths: influences of growth rate and solution composition. *Geochimica et Cosmochimica Acta*, *47*(2), 217–233.

Narbonne, G. M. (2005). The Ediacara biota: Neoproterozoic origin of animals and their ecosystems. *Annual Review of Earth and Planetary Sciences*, *33*, 421–442.

Nelson, L. L., Ramezani, J., Almond, J. E., Darroch, S. A. F., Taylor, W. L., Brenner, D. C., Furey, R. P., Turner, M., & Smith, E. F. (2022). Pushing the boundary: a calibrated Ediacaran-

Cambrian stratigraphic record from the Nama Group in northwestern Republic of South Africa. *Earth and Planetary Science Letters*, *580*, 117396.

Nesbitt, H. W., & Young, G. M. (1982). Early Proterozoic climates and plate motions inferred from major element chemistry of lutites. *Nature*, *299*(21), 715–717.

Nier, A. O. (1938). The isotopic constitution of strontium, barium, bismuth, thallium and mercury. *Physical Review*, *54*(4), 275–278. https://doi.org/10.1103/PhysRev.54.275

Palmer, M. R., & Edmond, J. M. (1989). The strontium isotope budget of the modern ocean. *Earth and Planetary Science Letters*, *92*(1), 11–26.

Parfrey, L. W., Lahr, D. J. G., Knoll, A. H., & Katz, L. A. (2011). Estimating the timing of early eukaryotic diversification with multigene molecular clocks. *Proceedings of the National Academy of Sciences of the United States of America*, *108*(33), 13624–13629.

Penny, A. M., Wood, R., Curtis, A., Bowyer, F., Tostevin, R., & Hoffman, K. H. (2014). Ediacaran metazoan reefs from the Nama Group, Namibia. *Science*, *344*(6191), 1504–1506.

Peterman, Z. E., Hedge, C. E., & Totjrtelot, H. A. (1970). Isotopic composition of strontium in sea water throughout Phanerozoic time. *Geochimica et Cosmochimica Acta*, *34*(1), 105–120.

Pickering, R. (2015). U–Pb dating small buried stalagmites from Wonderwerk Cave, South Africa: a new chronometer for earlier stone age cave deposits. *African Archaeological Review*, *32*(4), 645–668.

Pin, C., Gannoun, A., & Dupont, A. (2014). Rapid, simultaneous separation of Sr, Pb, and Nd by extraction chromatography prior to isotope ratios determination by TIMS and MC-ICP-MS. *Journal of Analytical Atomic Spectrometry*, *29*(10), 1858–1870.

Planavsky, N. J., Reinhard, C. T., Wang, X., Thomson, D., McGoldrick, P., Rainbird, R. H., & Fischer, W. W. (2014). Low Mid-Proterozoic atmospheric oxygen levels and the delayed rise of animals. *Science*, *346*(6209), 635–638.

Porter, S. M. (2007). Seawater chemistry and early carbonate biomineralization. *Science*, *316*(5829), 1302.

Porter, S. M. (2010). Calcite and aragonite seas and the de novo acquisition of carbonate skeletons. *Geobiology*, *8*(4), 256–277.

Pourmand, A., Dauphas, N., & Ireland, T. J. (2012). A novel extraction chromatography and MC-ICP-MS technique for rapid analysis of REE, Sc and Y: revising CI-chondrite and Post-Archean Australian Shale (PAAS) abundances. *Chemical Geology*, *291*, 38–54.

Pruss, S. B., Blättler, C. L., Macdonald, F. A., & Higgins, J. A. (2018). Calcium isotope evidence that the earliest metazoan biomineralizers formed aragonite shells. *Geology*, *46*(9), 763–766.

Richter, F. M., Rowley, D. B., & Depaolo, D. J. (1992). Sr isotope evolution of seawater: the role of tectonics. *Earth and Planetary' Science Letters*, *109*(1–2), 11–23.

Ries, J. B., Fike, D. A., Pratt, L. M., Lyons, T. W., & Grotzinger, J. P. (2009). Superheavy pyrite ($\delta^{34}S_{pyr} > \delta^{34}S_{CAS}$) in the terminal Proterozoic Nama Group, southern Namibia: a consequence of low seawater sulfate at the dawn of animal life. *Geology*, *37*(8), 743–746.

Romaniello, S. J., Herrmann, A. D., & Anbar, A. D. (2013). Uranium concentrations and $^{238}U/^{235}U$ isotope ratios in modern carbonates from the Bahamas: assessing a novel paleoredox proxy. *Chemical Geology*, *362*, 305–316.

Rooney, A. D., Cantine, M. D., Bergmann, K. D., Gómez-Pérez, I., al Baloushi, B., Boag, T. H., Busch, J. F., Sperling, E. A., & Strauss, J. v. (2020). Calibrating the coevolution of Ediacaran life and environment. *Proceedings of the National Academy of Sciences*, *117*(29), 16824–16830.

Rooney, A. D., Macdonald, F. A., Strauss, J. v, Dudás, F. Ö., Hallmann, C., & Selby, D. (2014). Re-Os geochronology and coupled Os-Sr isotope constraints on the Sturtian Snowball Earth. *Proceedings of the National Academy of Sciences*, *111*(1), 51–56.

Rooney, A. D., Strauss, J. v, Brandon, A. D., & Macdonald, F. A. (2015). A Cryogenian chronology: two long-lasting synchronous Neoproterozoic glaciations. *Geology*, *43*(5), 459–462.

Sahoo, S. K., Planavsky, N. J., Jiang, G., Kendall, B., Owens, J. D., Wang, X., Shi, X., Anbar, A. D., & Lyons, T. W. (2016). Oceanic oxygenation events in the anoxic Ediacaran ocean. *Geobiology*, *14*(5), 457–468.

Sawaki, Y., Ohno, T., Tahata, M., Komiya, T., Hirata, T., Maruyama, S., Windley, B. F., Han, J., Shu, D., & Li, Y. (2010). The Ediacaran radiogenic Sr isotope excursion in the Doushantuo Formation in the Three Gorges area, South China. *Precambrian Research*, *176*(1–4), 46–64.

Saylor, B. Z., Grotzinger, J. P., & Germs, G. J. B. (1995). Sequence stratigraphy and sedimentology of the Neoproterozoic Kuibis and Schwarzrand Subgroups (Nama Group), southwestern Namibia. *Precambrian Research*, *73*(1–4), 153–171.

Saylor, B. Z., Kaufman, A. J., Grotzinger, J. P., & Urban, F. (1998). A composite reference section for terminal Proterozoic strata of southern Namibia. *Journal of Sedimentary Research*, *68*(6), 1223–1235.

Schaller, M. F., Wright, J. D., & Kent, D. v. (2011). Atmospheric pCO_2 perturbations associated with the Central Atlantic Magmatic Province. *Science*, *331*(6023), 1404–1409.

Schaller, M. F., Wright, J. D., Kent, D. v., & Olsen, P. E. (2012). Rapid emplacement of the Central Atlantic Magmatic Province as a net sink for CO_2. *Earth and Planetary Science Letters*, *323*, 27–39. https://doi.org/10.1016/j.epsl.2011.12.028

Scholle, P. A., & Arthur, M. A. (1980). Carbon isotope fluctuations in Cretaceous pelagic limestones: potential stratigraphic and petroleum exploration toor. *The American Association of Petroleum Geologists Bulletin v*, *64*(1), 67–87.

Scholle, P. A., & Ulmer-Scholle, D. S. (2003). *A color guide to the petrography of carbonate rocks: grains, textures, porosity, diagenesis: Vol. AAPG Memoir 77*. AAPG.

Shackleton, N. J. (1986). Paleogene stable isotope events. *Palaeogeography, Palaeoclimatology, Palaeoecology*, *57*(1), 91–102.

Shen, B., Xiao, S., Zhou, C., Kaufman, A. J., & Yuan, X. (2010). Carbon and sulfur isotope chemostratigraphy of the Neoproterozoic Quanji Group of the Chaidam Basin, NW China: basin stratification in the aftermath of an Ediacaran glaciation postdating the Shuram event? *Precambrian Research*, *177*(3), 241–252.

Shields, G. A. (2007). A normalised seawater strontium isotope curve: possible implications for Neoproterozoic-Cambrian weathering rates and the further oxygenation of the Earth. *EEarth*, *2*(2), 35–42.

Shields, G., & Veizer, J. (2002). Precambrian marine carbonate isotope database: Version 1.1. *Geochemistry, Geophysics, Geosystems*, *3*(6).

Shields-Zhou, G., & Och, L. (2011). The case for a Neoproterozoic oxygenation event: geochemical evidence and biological consequences. *GSA Today*, *21*(3), 4–11.

Shore, A., & Wood, R. (2021). Environmental and diagenetic controls on the morphology and calcification of the Ediacaran metazoan *Cloudina*. *Scientific Reports*, *11*(1), 1–13.

Shore, A., Wood, R., Curtis, A., & Bowyer, F. (2020). Multiple branching and attachment structures in cloudinomorphs, Nama Group, Namibia. *Geology*, *48*(9), 877–881.

Simone, L. (1980). Ooids: a review. *Earth-Science Reviews*, *16*, 319–355.

Spooner, E. T. C. (1976). The strontium isotopic composition of seawater, and seawater-oceanic crust interaction. *Earth and Planetary Science Letters*, *31*(1), 167–174.

Stern, R. J. (2005). Evidence from ophiolites, blueschists, and ultrahigh-pressure metamorphic terranes that the modern episode of subduction tectonics began in Neoproterozoic time. *Geology*, *33*(7), 557–560.

Stern, R. J. (2018). The evolution of plate tectonics. *Philosophical Transactions of the Royal Society A: Mathematical, Physical and Engineering Sciences*, *376*(2132).

Tarhan, L. G., Droser, M. L., Cole, D. B., & Gehling, J. G. (2018). Ecological expansion and extinction in the late Ediacaran: weighing the evidence for environmental and biotic drivers. *Integrative and Comparative Biology*, *58*(4), 688–702.

Taylor, S. R., & McLennan, S. M. (1985). *The continental crust: Its composition and evolution*.

Tostevin, R. (2015). *Developing proxies to constrain redox gradients in terminal Ediacaran oceans*. UCL (University College London).

Tostevin, R., Bradbury, H. J., Shields, G. A., Wood, R. A., Bowyer, F., Penny, A. M., & Turchyn, A. v. (2019a). Calcium isotopes as a record of the marine calcium cycle versus carbonate diagenesis during the late Ediacaran. *Chemical Geology*, *529*.

Tostevin, R., Clarkson, M. O., Gangl, S., Shields, G. A., Wood, R. A., Bowyer, F., Penny, A. M., & Stirling, C. H. (2019b). Uranium isotope evidence for an expansion of anoxia in terminal Ediacaran oceans. *Earth and Planetary Science Letters*, *506*, 104–112.

Tostevin, R., He, T., Turchyn, A. v., Wood, R. A., Penny, A. M., Bowyer, F., Antler, G., & Shields, G. A. (2017). Constraints on the late Ediacaran sulfur cycle from carbonate associated sulfate. *Precambrian Research*, *290*, 113–125.

Tostevin, R., & Mills, B. J. W. (2020). Reconciling proxy records and models of earth's oxygenation during the Neoproterozoic and Palaeozoic. *Interface Focus*, *10*(4).

Tostevin, R., Shields, G. A., Tarbuck, G. M., He, T., Clarkson, M. O., & Wood, R. A. (2016a). Effective use of cerium anomalies as a redox proxy in carbonate-dominated marine settings. *Chemical Geology*, *438*, 146–162.

Tostevin, R., Wood, R. A., Shields, G. A., Poulton, S. W., Guilbaud, R., Bowyer, F., Penny, A. M., He, T., Curtis, A., Hoffmann, K. H., & Clarkson, M. O. (2016b). Low-oxygen waters limited habitable space for early animals. *Nature Communications*, *7*(1), 1–9.

Towe, K. M. (1970). Oxygen-collagen priority and the early metazoan fossil record. *Proceedings of the National Academy of Sciences*, *65*(4), 781–788.

Tucker, M. E., & Wright, V. P. (1990). *Carbonates sedimentology*. Blackwell Science Ltd.

Uahengo, C. I., Shi, X., Jiang, G., & Vatuva, A. (2020). Transient shallow-ocean oxidation associated with the late Ediacaran Nama skeletal fauna: evidence from iodine contents of the Lower Nama Group, southern Namibia. *Precambrian Research*, *343*.

Ullmann, C. V. (2016). The effect of precipitation rate on Mg/Ca and Sr/Ca ratios in biogenic calcite as observed in a belemnite rostrum. *Biogeosciences Discuss*, *8*, 1–14.

Urey, H. C., Lowenstam, H. A., Epstein, S., & Mckinney, C. R. (1951). Measurement of paleotemperatures and temperatures of the Upper Cretaceous of England, Denmark, and the southeastern United States. *Geological Society of America Bulletin*, *62*(4), 399–416.

Veizer, J. (1983). Chemical diagenesis of carbonates: theory and application of trace element technique. In M. A. Arthur, T. F. Anderson, I. R. Kaplan, J. Veizer, & L. S. Land (Eds.), *Stable Isotopes in Sedimentary Geology* (Issue SC10).

Veizer, J. (1989). Strontium isotopes in seawater through time. *Annual Reviews in Earth and Planetary Sciences*, *17*(1), 141–167.

Veizer, J. (2018). Trace elements and isotopes in sedimentary carbonates. In R. J. Reeder (Ed.), *Carbonates* (pp. 265–300). De Gruyter.

Veizer, J., Ala, D., Azmy, K., Bruckschen, P., Buhl, D., Bruhn, F., Carden, G. A. F., Diener, A., Ebneth, S., Godderis, Y., Jasper, T., Korte, C., Pawellek, F., Podlaha, O. G., & Strauss, H. (1999). $^{87}Sr/^{86}Sr$, $\delta^{13}C$ and $\delta^{18}O$ evolution of Phanerozoic seawater. *Chemical Geology*, *161*(1–3), 59–88.

Veizer, J., Buhl, D., Diener, A., Ebneth, S., Podlaha, O. G., Bruckschen, P., Jasper, T., Korte, C., Schaaf, M., Ala, D., & Azmy, K. (1997). Strontium isotope stratigraphy: potential resolution and event correlation. *Palaeogeography, Palaeoclimatology, Palaeoecology*, *132*(1–4), 65–77.

Veizer, J., & Compston, W. (1974). $^{87}Sr/^{86}Sr$ composition of seawater during the Phanerozoic. *Geochimica et Cosmochimica Acta*, *38*(9), 1461–1484.

Waggoner, B. (2003). The Ediacaran biotas in space and time. *Integrative and Comparative Biology*, *43*(1), 104–113.

Walker, J. C. G., Hays, P. B., & Kasting, J. F. (1981). A negative feedback mechanism for the long-term stabilization of earth's surface temperature. *Journal of Geophysical Research*, *86*(C10), 9776–9782.

Watters, W. A., & Grotzinger, J. P. (2001). Digital reconstruction of calcified early metazoans, terminal Proterozoic Nama Group, Namibia. *Paleobiology*, *27*(1), 159–171.

Webb, G. E., & Kamber, B. S. (2000). Rare earth elements in Holocene reefal microbialites: a new shallow seawater proxy. *Geochimica et Cosmochimica Acta*, *64*(9), 1557–1565.

Weissert, H. (1989). C-isotope stratigraphy, a monitor of paleoenvironmental change: a case study from the early Cretaceous. *Surveys in Geophysics*, *10*(1), 1–61.

Wen, B., Evans, D. A. D., Anderson, R. P., & McCausland, P. J. A. (2020). Late Ediacaran paleogeography of Avalonia and the Cambrian assembly of West Gondwana. *Earth and Planetary Science Letters*, *552*, 116591.

Wendler, I. (2013). A critical evaluation of carbon isotope stratigraphy and biostratigraphic implications for late Cretaceous global correlation. *Earth-Science Reviews*, *126*, 116–146.

Werne, J. P., & Hollander, D. J. (2004). Balancing supply and demand: controls on carbon isotope fractionation in the Cariaco Basin (Venezuela) Younger Dryas to present. *Marine Chemistry*, *92*(1–4), 275–293.

Wickman, F. E. (1948). Isotope ratios: a clue to the age of certain marine sediments. *The Journal of Geology*, *56*(1), 61–66.

Wood, R. (2018). Exploring the drivers of early biomineralization. *Emerging Topics in Life Sciences*, *2*(2), 201–212.

Wood, R. A. (2011). Paleoecology of the earliest skeletal metazoan communities: implications for early biomineralization. *Earth-Science Reviews*, *106*(1–2), 184–190.

Wood, R. A., Grotzinger, J. P., & Dickson, J. A. D. (2002). Proterozoic modular biomineralized metazoan from the Nama Group, Namibia. *Science*, *296*(5577), 2383–2386.

Wood, R. A., Poulton, S. W., Prave, A. R., Hoffmann, K. H., Clarkson, M. O., Guilbaud, R., Lyne, J. W., Tostevin, R., Bowyer, F., Penny, A. M., Curtis, A., & Kasemann, S. A. (2015). Dynamic redox conditions control late Ediacaran metazoan ecosystems in the Nama Group, Namibia. *Precambrian Research*, *261*, 252–271.

Wood, R. A., Zhuravlev, A. Y., Sukhov, S. S., Zhu, M., & Zhao, F. (2017a). Demise of Ediacaran dolomitic seas marks widespread biomineralization on the Siberian Platform. *Geology*, *45*(1), 27–30.

Wood, R., & Erwin, D. H. (2018). Innovation not recovery: dynamic redox promotes metazoan radiations. *Biological Reviews*, *93*(2), 863–873.

Wood, R., Ivantsov, A. Y., & Zhuravlev, A. Y. (2017b). First macrobiota biomineralization was environmentally triggered. *Proceedings of the Royal Society B: Biological Sciences*, *284*(1851), 20170059.

Wood, R., Liu, A. G., Bowyer, F., Wilby, P. R., Dunn, F. S., Kenchington, C. G., Cuthill, J. F. H., Mitchell, E. G., & Penny, A. (2019). Integrated records of environmental change and evolution challenge the Cambrian Explosion. *Nature Ecology and Evolution*, *3*(4), 528–538.

Wood, R., & Penny, A. (2018). Substrate growth dynamics and biomineralization of an Ediacaran encrusting poriferan. *Proceedings of the Royal Society B: Biological Sciences*, *285*(1870).

Xiao, S. (2020). Ediacaran sponges, animal biomineralization, and skeletal reefs. *Proceedings of the National Academy of Sciences of the United States of America*, *117*(35), 20997–20999.

Yang, C., Rooney, A. D., Condon, D. J., Li, X.-H., Grazhdankin, D. v, Bowyer, F. T., Hu, C., Macdonald, F. A., & Zhu, M. (2021). The tempo of Ediacaran evolution. *Science Advances*, *7*(45), eabi9643.

Zhai, L., Wu, C., Ye, Y., Zhang, S., & Wang, Y. (2018). Fluctuations in chemical weathering on the Yangtze Block during the Ediacaran–Cambrian transition: Implications for paleoclimatic conditions and the marine carbon cycle. *Palaeogeography, Palaeoclimatology, Palaeoecology*, *490*, 280–292.

Zhang, F., Xiao, S., Kendall, B., Romaniello, S. J., Cui, H., Meyer, M., Gilleaudeau, G. J., Kaufman, A. J., & Anbar, A. D. (2018). Extensive marine anoxia during the terminal Ediacaran Period. *Science Advances*, *4*, eaan8983.

Zhou, Y., von Strandmann, P. A. E. P., Zhu, M., Ling, H., Manning, C., Li, D., He, T., & Shields, G. A. (2020). Reconstructing Tonian seawater $^{87}Sr/^{86}Sr$ using calcite microspar. *Geology*, *48*(5), 462–467.

Zumberge, J. A., Love, G. D., Cárdenas, P., Sperling, E. A., Gunasekera, S., Rohrssen, M., Grosjean, E., Grotzinger, J. P., & Summons, R. E. (2018). Demosponge steroid biomarker 26-methylstigmastane provides evidence for Neoproterozoic animals. *Nature Ecology and Evolution*, *2*(11), 1709–1714.

9 Appendix

Table 1: Trace elements and carbon and oxygen isotopes data

Sample ID	Sr (ppm)	Mn (ppm)	Fe (ppm)	Rb (ppm)	Mn/Sr	Fe/Sr	Rb/Sr	$\delta^{13}C$	$\delta^{18}O$
Zebra River									
LO-2	23.64	42.57	885.05	<d.l.	1.80	37.44		-1.24	-10.93
LO-6	236.93	85.44	682.63	0.23	0.36	2.88	0.00096	1.43	-10.04
LO-07	674.42	483.15	394.48	<d.l.	0.72	0.58		2.03	-10.19
LO-08	400.52	189.67	1028.55	<d.l.	0.47	2.57		0.75	-10.18
LO-09	335.96	83.00	993.41	<d.l.	0.25	2.96		1.14	-9.56
LO-10	508.20	743.57	1475.94	<d.l.	1.46	2.90		1.35	-9.62
LO-11	359.37	198.65	823.55	<d.l.	0.55	2.29		1.62	-6.11
LO-15	453.03	152.06	1203.87	<d.l.	0.34	2.66		2.83	-6.43
LO-16	412.62	113.52	1198.40	<d.l.	0.28	2.90		1.98	-8.60
OS2-1	246.02	278.97	2140.89	<d.l.	1.13	8.70		1.56	-9.24
OS2-2	351.19	207.42	1527.14	<d.l.	0.59	4.35		1.30	-9.54
OS 2-3	290.50	460.48	1953.87	0.37	1.59	6.73	0.00128	2.63	-9.24
OS2-4	203.99	280.23	1776.96	<d.l.	1.37	8.71		2.98	-5.73
OS 2-6	155.39	40.50	1000.19	<d.l.	0.26	6.44		1.75	-8.03
ZR12	315.27	77.57	1547.38	<d.l.	0.25	4.91		5.97	-7.41

ZR19	309.18	35.94	908.93	<d.l.	0.12	2.94		3.73	-8.38
ZR34	1138.17	177.22	1418.37	<d.l.	0.16	1.25		3.33	-6.68
ZR36	824.58	118.29	1230.92	<d.l.	0.14	1.49		2.47	-6.27
Neint Nababeep Plateau									
ORMF01	537.69	3685.65	78546.21	1.30	6.85	146.08	0.00243	1.68	-6.30
ORMF02	379.02	1284.07	10752.90	0.34	3.39	28.37	0.00089	0.26	-21.37
ORMF03	308.23	1411.53	9230.96	0.96	4.58	29.95	0.00310	-0.29	-19.08
ORMF04	285.88	2121.07	51260.05	0.93	7.42	179.30	0.00327	1.32	-17.08
ORMF05	338.28	1642.56	10477.26	0.34	4.86	30.97	0.00101	0.93	-19.85
ORMF07	330.89	7182.90	51086.31	0.45	21.71	154.39	0.00135	-0.25	-5.14
ORMF08	1225.06	1071.82	7182.29	0.10	0.87	5.86	0.00008		
ORMF09	1605.59	1566.60	9513.35	0.10	0.98	5.93	0.00006	0.89	-18.44
ORH01	2902.45	1836.11	5793.54	0.19	0.63	2.00	0.00006	-0.06	-12.20
ORH02	6516.28	1504.77	5113.68	0.09	0.23	0.78	0.00001	1.46	-11.80
ORH03	3770.05	975.27	5288.67	0.07	0.26	1.40	0.00002	1.32	-13.61

ORH04	1146.53	2370.85	5559.77	0.11	2.07	4.85	0.00010	1.43	-16.46
ORH05	3453.42	4134.37	4249.37	0.09	1.20	1.23	0.00003	0.45	-15.48
ORH06	6056.08	353.59	5687.04	0.13	0.06	0.94	0.00002	2.41	-7.81
ORH07	3316.36	214.19	4228.20	0.08	0.06	1.27	0.00003	2.46	-9.95
ORH08	3723.51	185.61	4667.49	0.07	0.05	1.25	0.00002	2.35	-7.31
ORH09	3460.50	652.71	6049.83	0.21	0.19	1.75	0.00006	-2.77	-2.90
ORH10	2150.31	643.50	5681.35	0.19	0.30	2.64	0.00009	1.70	-10.23
ORH11	2260.86	283.35	4881.72	0.09	0.13	2.16	0.00004	1.56	-13.31
ORH12	4525.03	157.01	3317.57	0.07	0.03	0.73	0.00001	-10.90	-11.51
ORH13	4602.65	100.43	4167.01	0.04	0.02	0.91	0.00001	1.00	-12.58
ORH14	1257.67	907.83	4701.35	0.08	0.72	3.74	0.00006	2.46	-13.56
ORH15	1639.66	965.25	7212.77	0.09	0.59	4.40	0.00005	3.04	-11.75
ORH16	1458.45	283.93	2990.73	0.05	0.19	2.05	0.00004	2.46	-14.20
ORH17	6289.89	163.11	6880.13	0.09	0.03	1.09	0.00001	1.67	-10.38
ORH18	6769.76	198.28	8452.37	0.04	0.03	1.25	0.00001	2.63	-9.08
ORH19	5508.92	44.78	6306.45	0.04	0.01	1.14	0.00001	1.45	-8.50
ORH20	4305.94	81.23	4599.28	0.06	0.02	1.07	0.00001	1.27	-8.81
ORH21	9136.09	90.39	7527.40	0.17	0.01	0.82	0.00002	0.25	-8.39
ORH22	2461.21	60.17	4944.34	0.08	0.02	2.01	0.00003	1.20	-7.45
ORH23	6634.96	81.08	5729.51	0.06	0.01	0.86	0.00001	2.14	-8.69

ORH24	9261.37	121.90	8282.58	0.03	0.01	0.89	0.00000	1.53	-8.65
ORH25	6978.46	103.57	5737.07	0.06	0.01	0.82	0.00001	1.20	-5.14
ORH26	3009.94	854.31	8759.44	0.02	0.28	2.91	0.00001	-0.98	-9.96
ORLS02	2070.81	174.54	3472.54	0.33	0.08	1.68	0.00016	0.91	-10.58
ORLS03	697.92	143.40	2957.13	0.76	0.21	4.24	0.00109	-0.06	-7.69
ORLS04	2095.59	113.34	3378.12	0.30	0.05	1.61	0.00014	0.96	-8.68
ORLS05	158.90	79.55	2793.29	0.17	0.50	17.58	0.00110	0.58	-6.31
ORLS06	502.15	60.01	2756.89	0.14	0.12	5.49	0.00027	1.24	-8.44
ORLS07	43.94	92.89	2849.87	0.17	2.11	64.87	0.00397	0.77	-8.36
ORLS08	1717.85	60.01	2764.55	0.20	0.03	1.61	0.00011	1.08	-8.14
ORLS09	785.39	110.87	2861.16	0.14	0.14	3.64	0.00018	0.75	-14.60
ORLS10	669.39	314.68	2998.55	0.16	0.47	4.48	0.00024	0.75	-15.15
ORLS14	50.39	678.02	3266.99	0.17	13.46	64.83	0.00339	0.59	-12.93
ORLS15	559.71	473.85	3214.54	0.17	0.85	5.74	0.00030	0.23	-13.60
ORLS16	1017.57	244.60	3779.56	0.17	0.24	3.71	0.00017	0.73	-11.80
ORLS17	1338.07	180.28	2798.87	0.16	0.13	2.09	0.00012	0.73	-12.57
ORLS19	1199.18	160.09	3162.70	0.36	0.13	2.64	0.00030	0.85	-8.02
ORLS20	1591.18	144.45	2965.80	0.36	0.09	1.86	0.00023	-1.74	-5.88
ORLS21	395.63	94.56	2853.47	0.32	0.24	7.21	0.00080	-1.13	-5.67
ORLS22	1850.02	44.00	2982.65	0.22	0.02	1.61	0.00012	-0.33	-6.14

ORLS23	80.03	56.77	2861.62	0.21	0.71	35.76	0.00259	0.86	-7.60
ORLS24	1132.37	65.14	2309.42	0.26	0.06	2.04	0.00023	0.15	-8.61
ORLS26	69.39	56.11	2485.95	0.36	0.81	35.83	0.00521	-0.43	-6.48
ORLS27	1033.34	80.40	2536.29	0.47	0.08	2.45	0.00045	1.03	-9.32
ORLS28	592.70	98.70	2517.67	0.25	0.17	4.25	0.00042	0.87	-7.38
ORLS29	19.75	85.83	2541.79	0.19	4.34	128.67	0.00944	0.79	-9.56
ORLS30	26.22	150.72	2433.29	0.30	5.75	92.80	0.01129	-4.51	-6.16
ORLS31	1069.98	153.76	2718.89	0.32	0.14	2.54	0.00030	1.16	-8.55
ORLS32	755.86	112.54	2732.69	0.20	0.15	3.62	0.00026	1.40	-9.03
ORLS33	493.94	114.14	2985.26	0.20	0.23	6.04	0.00040	1.31	-9.58
ORLS34	1225.65	110.70	3391.28	0.16	0.09	2.77	0.00013	1.30	-10.03
ORLS35	1162.86	113.90	3114.79	0.23	0.10	2.68	0.00020	1.25	-9.84
ORLS36	2001.63	76.65	5204.94	0.30	0.04	2.60	0.00015	0.91	-7.89
ORLS37	1951.53	66.78	2931.07	0.45	0.03	1.50	0.00023	1.10	-8.59
ORLS38	1381.08	193.10	3134.03	0.33	0.14	2.27	0.00024	1.19	-8.73
ORLS39	1449.64	94.81	2697.77	0.50	0.07	1.86	0.00034	1.13	-6.40
ORLS40	3363.33	142.06	2965.04	0.31	0.04	0.88	0.00009	0.16	-7.52
ORLS41	2671.04	69.88	2745.94	0.19	0.03	1.03	0.00007	1.04	-7.21
ORLS42	2771.59	71.10	3279.85	0.34	0.03	1.18	0.00012	1.24	-6.50
ORLS43	2797.36	154.43	3825.08	0.55	0.06	1.37	0.00020	-0.33	-8.76

ORLS44	2823.95	430.73	4879.03	0.80	0.15	1.73	0.00028	-0.18	-7.63
ORLS45	1284.27	394.60	3033.30	0.50	0.31	2.36	0.00039	-0.44	-6.53
ORLS46	1971.56	411.79	2911.35	0.33	0.21	1.48	0.00017	0.75	-9.57
ORLS52	621.24	165.79	2726.26	0.28	0.27	4.39	0.00045	-0.35	-9.61
ORLS53	159.55	157.77	2756.92	0.32	0.99	17.28	0.00201	1.18	-12.21
ORLS54	582.21	69.75	4586.62	0.27	0.12	7.88	0.00046	1.49	-9.54
ORLS55	1120.19	61.39	2714.16	0.18	0.05	2.42	0.00016	1.30	-7.78
ORLS56	130.53	171.72	3121.56	0.25	1.32	23.92	0.00189	1.15	-13.89
ORLS57	414.02	103.99	2714.97	0.24	0.25	6.56	0.00059	1.56	-11.91
ORLS58	778.35	130.35	2729.90	0.24	0.17	3.51	0.00030	1.41	-8.42
ORLS59	1001.97	52.23	2755.90	0.20	0.05	2.75	0.00020	1.51	-9.26
ORSN01	816.26	315.20	2970.39	0.40	0.39	3.64	0.00049	1.04	-11.70
ORSN02	1113.50	113.91	2934.79	0.36	0.10	2.64	0.00033	0.63	-11.98
ORSN03	619.62	164.36	2869.85	0.36	0.27	4.63	0.00058	0.89	-12.79
ORSN04	555.43	144.47	2629.98	0.47	0.26	4.74	0.00084	0.73	-16.28
ORSN05	1084.74	121.25	2866.58	0.27	0.11	2.64	0.00024	0.74	-8.77
ORSN06	917.87	183.78	2923.03	0.24	0.20	3.18	0.00027	0.54	-9.55
ORSN07	1895.30	181.67	2935.36	0.32	0.10	1.55	0.00017	-1.72	-9.79
ORSN08	1331.97	176.50	3230.42	0.24	0.13	2.43	0.00018	0.25	-9.36
ORSN11	1533.08	514.52	3363.15	0.25	0.34	2.19	0.00016	-0.98	-14.10

ORSN12	1801.71	488.25	4565.54	0.33	0.27	2.53	0.00018	0.38	-13.49
ORSN13	1504.08	192.14	2914.24	0.16	0.13	1.94	0.00011	-0.72	-12.29
ORSN14	1715.86	130.08	3165.49	0.19	0.08	1.84	0.00011	0.08	-10.34
ORSN15	2111.19	1102.02	3282.83	0.48	0.52	1.55	0.00023	0.38	-11.35
ORSN16	1941.19	531.17	3133.95	0.33	0.27	1.61	0.00017	0.42	-11.88
ORSN17	1891.73	665.47	4030.27	0.21	0.35	2.13	0.00011	0.98	-6.87

Table 2: REE and Yttrium data

	PAAS normalised Light REE					**PAAS normalised Medium REE**						**PAAS normalised Heavy REE**				
	La	Ce	Pr	N^d	Pm	Sm	Eu	Gd	Tb	Dy	Y	Ho	Er	Tm	Yb	Lu
Zebra River																
LO2	0.32	0.29	0.34	0.37	0.43	0.49	0.92	0.71	0.77	0.80	1.14	0.84	0.84	0.74	0.66	0.68
LO6	0.12	0.10	0.10	0.10	0.11	0.11	0.15	0.14	0.13	0.12	0.16	0.12	0.12	0.10	0.09	0.09
LO7	0.24	0.29	0.23	0.26	0.31	0.36	0.44	0.49	0.55	0.55	0.67	0.56	0.54	0.45	0.39	0.38
LO8	0.03	0.02	0.02	0.02	0.01	0.01	0.02	0.02	0.02	0.02	0.04	0.02	0.02	0.02	0.01	0.01
LO9	0.04	0.02	0.02	0.02	0.02	0.02	0.02	0.03	0.02	0.02	0.04	0.02	0.02	0.02	0.01	0.02
LO10	0.17	0.16	0.16	0.17	0.18	0.20	0.25	0.25	0.26	0.24	0.31	0.25	0.24	0.21	0.17	0.17
LO11	0.01	0.01	0.01	0.01	0.01	0.01	0.01	0.01	0.01	0.02	0.05	0.02	0.02	0.02	0.02	0.02
LO15	0.11	0.10	0.07	0.08	0.10	0.11	0.15	0.18	0.17	0.16	0.25	0.18	0.17	0.14	0.11	0.11

LO16	0.05	0.04	0.03	0.04	0.04	0.04	0.06	0.08	0.09	0.10	0.19	0.11	0.11	0.09	0.07	0.07
OS2-1	0.11	0.10	0.11	0.12	0.12	0.12	0.15	0.16	0.15	0.13	0.21	0.14	0.13	0.11	0.09	0.09
OS2-2	0.12	0.13	0.14	0.16	0.17	0.18	0.28	0.21	0.22	0.19	0.24	0.20	0.19	0.16	0.15	0.15
OS2-3	0.03	0.03	0.02	0.03	0.03	0.03	0.05	0.04	0.04	0.03	0.07	0.03	0.03	0.02	0.02	0.02
OS2-4	0.17	0.17	0.20	0.23	0.26	0.29	0.46	0.32	0.33	0.29	0.34	0.28	0.26	0.22	0.19	0.19
OS2-6	0.09	0.09	0.09	0.11	0.12	0.14	0.25	0.20	0.20	0.18	0.26	0.19	0.16	0.12	0.09	0.09
ZR 12	0.17	0.16	0.15	0.18	0.19	0.20	0.28	0.30	No data	0.26	0.33	0.27	0.24	0.19	0.15	0.15
ZR 19	0.03	0.02	0.02	0.02	0.02	0.02	0.02	0.02	No data	0.02	0.04	0.02	0.03	0.02	0.02	0.02
ZR 34	0.09	0.08	0.08	0.09	0.08	0.08	0.15	0.12	No data	0.10	0.15	0.11	0.10	0.07	0.07	0.06
ZR 36	0.10	0.08	0.08	0.09	0.08	0.07	0.11	0.11	No data	0.09	0.15	0.11	0.10	0.08	0.07	0.07
Neint Nababeep Plateau																
MF01	0.21	0.30	0.36	0.45	0.67	0.88	1.24	1.21	1.18	1.17	No data	1.10	1.02	0.87	0.87	0.81
MF02	0.18	0.20	0.22	0.23	0.28	0.32	0.44	0.39	0.41	0.38	No data	0.34	0.34	0.24	0.28	0.21

MF03	0.35	0.41	0.49	0.53	0.66	0.79	0.84	0.92	0.94	0.87	No data	0.81	0.75	0.60	0.61	0.53
MF04	0.23	0.31	0.35	0.39	0.50	0.60	0.87	0.73	0.75	0.68	No data	0.59	0.55	0.41	0.43	0.35
MF05	0.25	0.35	0.36	0.39	0.47	0.56	0.69	0.66	0.69	0.63	No data	0.56	0.53	0.40	0.42	0.34
MF07	0.17	0.25	0.27	0.31	0.44	0.57	0.94	0.78	0.82	0.71	No data	0.62	0.56	0.40	0.42	0.33
MF08	0.01	0.01	0.01	0.01	0.01	0.01	No data	No data	0.02	0.02	No data	No data	0.02	No data	0.01	No data
MF09	0.03	0.04	0.03	0.04	0.05	0.05	0.04	0.05	0.09	0.08	No data	0.07	0.08	No data	0.05	No data
H01	0.10	0.10	0.10	0.10	0.11	0.12	0.16	0.17	0.17	0.17	No data	0.18	0.17	0.14	0.14	0.12
H02	0.01	0.00	0.00	0.00	0.00	0.00	No data	No data	0.00	0.00	No data	No data	0.00	No data	No data	No data
H03	0.01	0.01	0.01	0.01	0.02	0.02	0.02	0.02	0.03	0.03	No data	0.02	0.02	0.00	0.01	No data
H04	0.09	0.10	0.11	0.11	0.13	0.14	0.16	0.19	0.20	0.19	No data	0.18	0.17	0.13	0.13	0.11

H05	0.01	0.01	0.01	0.01	0.01	0.01	0.01	0.00	0.01	0.01	No data	0.01	0.01	No data	0.01	No data
H06	0.01	0.00	0.00	0.00	0.00	0.00	No data	No data	0.00	0.00	No data	No data	0.00	No data	0.00	No data
H07	0.02	0.02	0.02	0.02	0.02	0.02	0.02	0.03	0.03	0.04	No data	0.04	0.04	0.02	0.03	0.02
H08	0.00	0.00	No data	0.00	No data	No data	No data	No data	No data	No data	No data	No data	No data	No data	No data	No data
H09	0.11	0.11	0.11	0.11	0.12	0.13	0.15	0.15	0.16	0.16	No data	0.16	0.16	0.13	0.13	0.12
H10	0.06	0.05	0.05	0.05	0.05	0.06	0.08	0.08	0.09	0.08	No data	0.08	0.08	0.06	0.06	0.05
H11	0.01	0.01	0.01	0.01	0.01	0.01	0.02	0.02	0.02	0.02	No data	0.02	0.02	0.00	0.02	No data
H12	0.01	0.01	0.01	0.01	0.01	0.01	0.01	0.00	0.01	0.01	No data	0.01	0.01	No data	0.01	No data
H13	0.00	0.00	No data	0.00	No data	No data	No data	No data	0.00	0.00	No data	No data	0.00	No data	No data	No data
H14	0.01	0.00	0.00	0.00	0.00	0.00	No data	No data	0.01	0.01	No data	0.00	0.01	No data	0.01	No data

H15	0.02	0.02	0.02	0.02	0.03	0.04	0.05	0.06	0.07	0.08	No data	0.08	0.08	0.05	0.05	0.03
H16	0.01	0.00	0.00	0.00	0.00	0.00	No data	No data	0.01	0.01	No data	0.00	0.01	No data	0.00	No data
H17	0.00	0.00	0.00	0.00	0.00	0.00	No data	No data	0.00	0.00	No data	0.00	0.00	No data	0.00	No data
H18	0.00	0.00	0.00	0.00	0.00	0.00	No data	No data	0.01	0.01	No data	0.00	0.01	No data	0.00	No data
H19	0.00	0.00	No data	0.00	0.00	0.00	No data	No data	0.00	0.00	No data	0.00	0.00	No data	0.00	No data
H20	0.01	0.00	0.00	0.01	0.01	0.01	0.00	0.01	0.01	0.02	No data	0.01	0.02	No data	0.01	No data
H21	0.00	0.00	0.00	0.00	0.00	0.00	No data	No data	0.00	0.00	No data	0.00	0.00	No data	0.00	No data
H22	0.01	0.00	0.00	0.00	0.00	0.00	No data	0.00	0.01	0.01	No data	0.01	0.01	No data	0.01	No data
H23	0.01	0.00	0.00	0.00	0.00	0.00	No data	No data	0.01	0.01	No data	0.00	0.01	No data	0.01	No data
H24	0.00	0.00	0.00	0.00	0.00	0.00	0.00	0.00	0.01	0.01	No data	0.01	0.01	No data	0.01	No data

H25	0.00	0.00	No data	0.00	No data	No data	No data	No data	No data	No data	No data	No data	No data	No data	No data	No data
H26	0.01	0.00	0.00	0.00	0.00	0.00	0.00	0.01	0.01	0.01	No data	0.01	0.02	No data	0.01	No data
ORLS-02	0.05	0.05	0.05	0.05	0.05	0.06	0.09	0.07	0.08	0.08	0.10	0.08	0.08	0.07	0.06	0.07
ORLS-03	0.04	0.04	0.04	0.04	0.05	0.06	0.10	0.07	0.08	0.08	0.10	0.08	0.07	0.07	0.06	0.07
ORLS-04	0.01	0.01	0.01	0.01	0.02	0.02	0.02	0.02	0.03	0.03	0.04	0.03	0.03	0.03	0.03	0.03
ORLS-05	0.01	0.01	0.01	0.01	0.01	0.01	0.01	0.01	0.01	0.01	0.02	0.01	0.01	0.01	0.01	0.01
ORLS-06	0.00	0.00	0.00	0.00	0.00	0.01	0.01	0.01	0.01	0.01	0.02	0.01	0.02	0.02	0.02	0.02
ORLS-07	0.01	0.01	0.01	0.01	0.01	0.02	0.02	0.02	0.03	0.03	0.05	0.04	0.04	0.03	0.03	0.03
ORLS-08	0.01	0.01	0.01	0.01	0.01	0.02	0.02	0.02	0.03	0.03	0.05	0.03	0.04	0.03	0.03	0.03
ORLS-09	0.00	0.00	0.00	0.00	0.01	0.01	0.01	0.01	0.01	0.01	0.03	0.02	0.02	0.02	0.02	0.02
ORLS 10	0.01	0.01	0.01	0.01	0.01	0.01	0.02	0.02	0.02	0.02	0.04	0.02	0.02	0.02	0.02	0.02
ORLS 14	0.04	0.03	0.05	0.05	0.07	0.09	0.11	0.12	0.13	0.13	0.18	0.14	0.13	0.11	0.10	0.10
ORLS 15	0.01	0.01	0.01	0.01	0.02	0.02	0.04	0.04	0.05	0.06	0.10	0.06	0.06	0.06	0.05	0.06
ORLS 16	0.01	0.01	0.01	0.01	0.01	0.01	0.02	0.02	0.03	0.03	0.05	0.03	0.03	0.03	0.03	0.03
ORLS 17	0.03	0.03	0.03	0.03	0.04	0.05	0.06	0.07	0.09	0.10	0.19	0.12	0.14	0.14	0.13	0.14
ORLS 19	0.04	0.03	0.04	0.04	0.05	0.06	0.07	0.07	0.08	0.07	0.10	0.08	0.08	0.07	0.06	0.06
ORLS 20	0.04	0.03	0.04	0.04	0.04	0.05	0.09	0.06	0.07	0.07	0.11	0.08	0.08	0.07	0.06	0.07
ORLS 21	0.03	0.02	0.02	0.02	0.03	0.03	0.07	0.04	0.05	0.05	0.09	0.06	0.07	0.06	0.06	0.07

ORLS 22	0.02	0.02	0.02	0.02	0.02	0.03	0.04	0.04	0.04	0.04	0.07	0.05	0.05	0.05	0.04	0.05
ORLS 23	0.02	0.01	0.02	0.02	0.02	0.02	0.03	0.03	0.03	0.03	0.05	0.04	0.04	0.04	0.03	0.03
ORLS 24	0.03	0.02	0.03	0.02	0.03	0.03	0.06	0.04	0.04	0.05	0.06	0.05	0.05	0.05	0.04	0.05
ORLS 26	0.03	0.02	0.03	0.02	0.03	0.03	0.04	0.04	0.05	0.05	0.07	0.06	0.06	0.06	0.05	0.05
ORLS 27	0.02	0.02	0.02	0.02	0.02	0.03	0.04	0.04	0.04	0.04	0.06	0.04	0.04	0.04	0.04	0.04
ORLS 28	0.01	0.01	0.01	0.01	0.01	0.02	0.02	0.02	0.02	0.02	0.04	0.03	0.03	0.02	0.02	0.03
ORLS 29	0.01	0.01	0.01	0.01	0.02	0.02	0.03	0.03	0.03	0.04	0.07	0.04	0.04	0.04	0.04	0.04
ORLS 30	0.03	0.02	0.03	0.03	0.03	0.04	0.05	0.05	0.06	0.06	0.10	0.07	0.07	0.07	0.06	0.07
ORLS 31	0.03	0.02	0.02	0.02	0.03	0.03	0.05	0.04	0.04	0.04	0.06	0.04	0.04	0.03	0.03	0.03
ORLS 32	0.01	0.01	0.01	0.01	0.01	0.01	0.02	0.02	0.02	0.02	0.03	0.02	0.02	0.02	0.02	0.02
ORLS 33	0.01	0.00	0.01	0.01	0.01	0.01	0.01	0.01	0.01	0.01	0.02	0.01	0.01	0.01	0.01	0.01
ORLS 34	0.01	0.01	0.01	0.01	0.01	0.01	0.02	0.02	0.02	0.02	0.03	0.02	0.02	0.02	0.02	0.02
ORLS 35	0.02	0.02	0.02	0.02	0.02	0.03	0.03	0.04	0.04	0.04	0.06	0.05	0.05	0.04	0.04	0.04
ORLS 36	0.03	0.02	0.02	0.02	0.03	0.03	0.05	0.05	0.05	0.05	0.08	0.06	0.06	0.05	0.05	0.05
ORLS 37	0.03	0.02	0.03	0.03	0.03	0.04	0.05	0.05	0.05	0.06	0.08	0.06	0.06	0.06	0.05	0.06
ORLS 38	0.02	0.02	0.02	0.02	0.02	0.03	0.04	0.04	0.04	0.04	0.07	0.05	0.05	0.05	0.04	0.05
ORLS 39	0.02	0.02	0.02	0.02	0.03	0.03	0.04	0.04	0.05	0.05	0.08	0.06	0.06	0.06	0.05	0.05
ORLS 40	0.06	0.05	0.06	0.05	0.07	0.08	0.09	0.10	0.11	0.11	0.16	0.12	0.12	0.11	0.10	0.10
ORLS 41	0.02	0.01	0.02	0.01	0.02	0.02	0.03	0.03	0.03	0.03	0.05	0.04	0.03	0.03	0.03	0.03
ORLS 42	0.03	0.02	0.02	0.02	0.03	0.03	0.04	0.04	0.05	0.05	0.07	0.05	0.05	0.05	0.04	0.05

ORLS 43	0.08	0.07	0.08	0.07	0.09	0.10	0.23	0.11	0.13	0.12	0.16	0.13	0.12	0.11	0.10	0.10
ORLS 44	0.09	0.08	0.10	0.10	0.13	0.16	0.26	0.20	0.22	0.22	0.28	0.22	0.20	0.18	0.16	0.15
ORLS 45	0.07	0.06	0.07	0.07	0.09	0.11	0.29	0.14	0.15	0.15	0.19	0.14	0.13	0.12	0.11	0.11
ORLS 46	0.03	0.02	0.02	0.02	0.03	0.03	0.06	0.05	0.06	0.06	0.10	0.07	0.07	0.07	0.06	0.06
ORLS 52	0.02	0.01	0.01	0.01	0.02	0.02	0.03	0.03	0.03	0.03	0.05	0.04	0.04	0.03	0.03	0.04
ORLS 53	0.02	0.02	0.02	0.02	0.02	0.03	0.03	0.04	0.04	0.04	0.06	0.04	0.05	0.04	0.04	0.04
ORLS 54	0.01	0.01	0.01	0.01	0.02	0.02	0.02	0.03	0.03	0.03	0.04	0.03	0.03	0.03	0.03	0.03
ORLS 55	0.01	0.01	0.01	0.01	0.02	0.02	0.03	0.03	0.03	0.04	0.06	0.04	0.04	0.04	0.04	0.04
ORLS 56	0.03	0.03	0.03	0.03	0.04	0.05	0.06	0.06	0.07	0.07	0.09	0.07	0.07	0.07	0.06	0.06
ORLS 57	0.02	0.02	0.02	0.02	0.02	0.03	0.03	0.04	0.04	0.04	0.06	0.05	0.05	0.05	0.04	0.05
ORLS 58	0.02	0.02	0.02	0.02	0.03	0.03	0.04	0.05	0.05	0.06	0.09	0.06	0.06	0.06	0.05	0.06
ORLS 59	0.01	0.01	0.01	0.01	0.01	0.01	0.02	0.02	0.02	0.03	0.05	0.03	0.03	0.03	0.03	0.04
ORSN-01	0.02	0.01	0.02	0.02	0.02	0.02	0.03	0.03	0.04	0.04	0.06	0.04	0.04	0.04	0.03	0.04
ORSN-02	0.02	0.01	0.01	0.01	0.02	0.02	0.03	0.03	0.03	0.03	0.05	0.04	0.04	0.03	0.03	0.03
ORSN-03	0.02	0.02	0.02	0.02	0.02	0.02	0.04	0.03	0.03	0.03	0.05	0.03	0.03	0.03	0.03	0.03
ORSN-04	0.02	0.01	0.01	0.01	0.02	0.02	0.03	0.03	0.03	0.03	0.05	0.03	0.03	0.03	0.03	0.04
ORSN-05	0.02	0.02	0.02	0.02	0.02	0.03	0.04	0.04	0.04	0.04	0.06	0.05	0.05	0.04	0.04	0.05
ORSN-06	0.03	0.02	0.02	0.02	0.02	0.03	0.03	0.04	0.04	0.04	0.07	0.05	0.05	0.05	0.05	0.05
ORSN-07	0.04	0.03	0.03	0.03	0.04	0.05	0.07	0.06	0.06	0.07	0.10	0.07	0.07	0.06	0.06	0.06
ORSN-08	0.03	0.02	0.02	0.02	0.02	0.03	0.06	0.04	0.04	0.04	0.09	0.05	0.05	0.04	0.04	0.05

ORSN-11	0.03	0.03	0.03	0.03	0.04	0.04	0.08	0.05	0.06	0.06	0.08	0.06	0.06	0.06	0.05	0.06
ORSN-12	0.07	0.06	0.06	0.06	0.07	0.08	0.14	0.10	0.10	0.10	0.14	0.11	0.11	0.10	0.09	0.09
ORSN-13	0.01	0.01	0.01	0.01	0.02	0.02	0.03	0.03	0.03	0.03	0.05	0.04	0.04	0.03	0.03	0.03
ORSN-14	0.04	0.03	0.04	0.04	0.04	0.05	0.07	0.06	0.06	0.06	0.09	0.07	0.07	0.06	0.05	0.06
ORSN-15	0.10	0.08	0.09	0.08	0.09	0.11	0.25	0.12	0.13	0.13	0.18	0.13	0.13	0.11	0.10	0.10
ORSN-16	0.04	0.04	0.04	0.04	0.05	0.05	0.09	0.06	0.07	0.07	0.09	0.07	0.07	0.06	0.05	0.06
ORSN-17	0.02	0.02	0.02	0.02	0.02	0.03	0.03	0.03	0.04	0.04	0.05	0.04	0.04	0.03	0.03	0.03